MASTER THESIS

Development of the Pixel Detector for the ATLAS Detector Upgrade

Laboratory of Experimental Particle Physics
Department of Physics, Kyushu University

Mathieu Darnajou
Supervisor : Junji Tojo

February 6th, 2017

九州大学
KYUSHU UNIVERSITY

"L'expérience est un peigne pour les chauves, un haut parleur pour les muets, un tableau pour les aveugles. Mais il y a néanmoins un point qui peut servir : savoir ce qui est important dans la vie."

Gérard Mancret

Abstract

The *Standard Model* (SM) of particle physics describes a consistent theoretical framework in the range of the currently accessible experimental data. Even though it is currently the best description of the universe, it does not explain, for example, the existence of Dark Matter observed in galaxy rotation or the oscillation of the neutrinos between their flavors. Those exceptions are not predicted by the SM and lead to the necessity of new theories called *Beyond the Standard Model* (BSM). The observation of new phenomena has become a main goal for particle physics. The Large Hadron Collider (LHC) at CERN, the current energy-frontier accelerator of proton-proton collisions, has been running for that purpose. A future physics program started being developed with the increased luminosity by the LHC upgrade.

The *ATLAS experiment* at the LHC has been operating a general-purpose detector. As the luminosity increases, it will become necessary to *upgrade the detector* to face up to high luminosity and high radiation damage. In particular, the Inner Detector close to the collision point will be replaced by a new detector, the silicon pixel detector, located in the innermost layer. This detector technology gives the best precision for charged particle position detection with individual pixel readout. To meet the tighten requirements of high readout speed and smaller pixel size, a new chip called *RD53* is under development. Kyushu University is preparing to participate to the conception of the *RD53* chip, since the new facility at the top of the technology to develop silicon detectors was built.

Currently, the innermost layer of the ATLAS Pixel detector uses *FE-I4* chips. The *FE-I4* (*RD53*) chip measures 20 × 19 (25 × 25) mm^2 and is composed of 80 × 226 (1024 × 256) pixels. Each pixel measures 50 × 250 (25 × 100) μm^2. When a charged particle passes through the detector, it leaves a signal of 15,000 electrons. This signal is compared to a *threshold* and the output is *Time over Threshold (ToT)*. Once the *RD53 chip* is ready to use, it will be important to quickly characterize and operate it in data taking conditions. This means to *tune* the chip with the *Threshold* and *ToT* that minimize the noise with the best performances. A *Data Acquisition System* was developed to inject signal charge and read the data from the *FE-I4* chip. The *Threshold* and *ToT* that maximize data quality are found to be 3,000 electrons and 5 × 25 ns, respectively.

To understand accurately the necessity for the upgrade, a qualitative simulation study of the physics case was made based on two phenomena involving rare Higgs production processes. One is the potential discovery of other type of Higgs boson predicted by the *Minimal Supersymmetric Standard Model*. The *Heavy Neutral Higgs* can decay to a pair of Higgs bosons, each of which would be detected in the upgraded ATLAS detector. The other is to measure the Higgs self-coupling through the Higgs pair production. The Higgs self-coupling is one of the important properties of the Higgs boson to understand the *electroweak symmetry breaking* in the Higgs potential of the SM. Both simulation studies are based on *Higgs pair production* and *background events*. A Higgs pair decays in the $\gamma\gamma b\bar{b}$ channel where one Higgs boson decays to a pair of photons and the other to a pair of b-quark and anti b-quark. The number of the heavy Higgs boson detected in the ATLAS detector was estimated depending on its mass. To study the self-coupling, the number of the signal and background events was also estimated in the SM.

Contents

List of Figures

List of Tables

Part I

Introduction

Chapter 1

The ATLAS Experiment

1.1 Introduction

The *Standard Model* (SM) of particle physics is a theory concerning the electromagnetic, weak, and strong nuclear interactions, as well as classifying all the subatomic particles known. Over time and through many experiments, the SM has become established as a well-tested physics theory and is currently the best description of the universe. However, it does not explain the complete picture. For example, the existence of Dark Matter observed in galaxy rotation, the oscillation of the neutrinos between their flavors or the existence of three generations of matter. Those observations are not predicted by the SM (Chap. 2). Perhaps it is only a part of a bigger picture that includes new physics. The explanation of those phenomena has become a main goal for particle physics and leads to the necessity of new theories called *Beyond the Standard Model* (BSM). The Large Hadron Collider (LHC) (Sec. 1.2) at CERN, the current energy-frontier accelerator of proton-proton collision, has been running for that purpose. A future physics program (sec. 1.2.2) started being developed with the increased luminosity by the LHC upgrade.

The *ATLAS experiment* (Sec. 1.3) at the LHC has been operating a general-purpose detector, investigating a wide range of physics. As the luminosity increases, it will become necessary to *upgrade the detector* to face up to high luminosity and high radiation damage. In particular in the innermost layer, the *Inner Detector* (ID) (Sec. 1.3.2) close to the collision point will be replaced by a new detector, the *Inner Tracker* (ITk) (Sec. 1.4), that will contain pixel and strip detectors. This detector technology gives the best precision for charged particle position detection with individual pixel readout. To meet the tighten requirements of high readout speed and smaller pixel size, a new chip called *RD53* is under development. Kyushu University is preparing to participate to the conception of the *RD53* chip, and installed the new facility at the top of the technology to develop silicon detectors. The part II of this thesis concerns the development of the new generation pixel detector at Kyushu University.

A qualitative simulation study is necessary to understand accurately the necessity for the ATLAS upgrade. Hence, the part III of this thesis concerns the physics case, based on two phenomena involving rare Higgs production processes (Sec. 2.2). One is the potential discovery of the other type of Higgs boson (Sec. 2.2.2) predicted by the *Minimal Supersymmetric Standard Model.* The *Heavy Neutral Higgs* can decay to a pair of Higgs bosons, each of which would be detected in the upgraded ATLAS detector. The other is to measure the Higgs self-coupling (Sec. 2.2.1) through the Higgs pair production. The Higgs self-coupling is one of the important properties of the Higgs boson to understand the *electroweak symmetry breaking* in the Higgs potential of the SM. Both simulation studies are based on *Higgs pair production* and *background events*. A Higgs pair decays in the $\gamma\gamma b\bar{b}$ channel where one Higgs boson decays to a pair of photons and the other to a pair of b-quark and anti b-quark. Currently, because the number of measured events is very few, the production cross section cannot be determined but only an upper bound. A more accurate analysis that corresponds to the observation of the phenomenon will necessitate a much higher luminosity.

The topics of this thesis concern the upgrade of the *ATLAS detector* (Sec. 1.3) and studies of the upgrade of the LHC at CERN. It is essential to understand the experimental context before to explain the related research. This chapter contains an overview of the CERN and also a presentation of the LHC and its upgrade prospects. The ATLAS detector will then be presented with an explanation of its different parts and some of its characteristics. Finally, the presentation will focus on the prospects for *inner trackers* upgrade to introduce the *FE-I4 chip* which is the main part of the ATLAS detector concerned by this research.

1.2 The Large Hadron Collider at CERN

Founded in 1954, the CERN (*in French* : le Centre Européen de Recherche Nucléaire) is a laboratory for particle and nuclear physics situated at the Franco-Swiss border near Geneva. The *Large Hadron Collider* (LHC) (fig. 1.1) is a proton-proton synchrotron collider situated at the CERN. Built between 1998 and 2008, it is installed in a 27 kilometers long tunnel at 100 meters under the city of Geneva, Switzerland. Currently, the LHC is producing collisions of proton beam at center of mass energy of $\sqrt{s} = 13$ TeV. It corresponds to *the highest energy* ever reached by a particle collider.

The LHC regroups a total of seven experiments. At the four collision points are situated the four main experiments :

- **ALICE** : The main task of the ALICE experiment is to study the properties of the quark-gluon plasma, created from heavy ion collisions. This extreme state of matter, where the quarks and the gluons are not confined into hadrons, might have existed in the nature just after the Big Bang.

- **CMS** : The CMS detector was built to observe most of processes that occurs from high energy proton-proton collisions. The design combines a compact geometry and a great precision. The solenoid magnet that surround all the sub-detectors is the characteristic of this detector.

- **LHCb** : The study of the bottom quark allows to observe processes that concerns matter-antimatter asymmetry. B mesons produced by proton collisions stay close to the beam pipe. This is the reason why the LHCb detector do not surround the collision point as the other experiments.

- **ATLAS** : Finally, the ATLAS detector has the same task as CMS to observe a large range of physics processes that occurs in proton collisions. The two main goals for this detector was first the discovery of the Higgs boson (Sec. 2.1.2) in 2012 and the research for BSM physics. To confirm the reproductivity of the results, an observation is needed both by CMS and ATLAS. The collaborations are then working in the same directions. The ATLAS detector is described more in detail in the section 1.3.

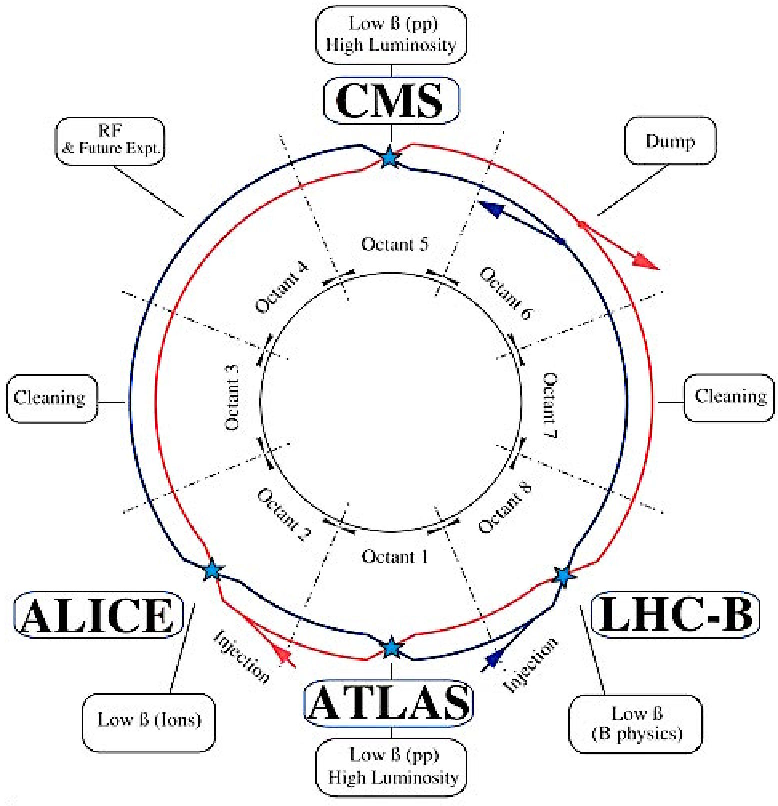

Figure 1.1: Layout of LHC and the main experiments, identified at their location in the accelerator ring. *(Source : LHC Results Highlights, CLASHEP 2013)*

1.2.1 Characteristics of the LHC

The LHC is composed of 1,232 *dipole electromagnets* of 16.5 m long and 27 tons each. There are maintained at a temperature of 1.9 K by the circulation of *superfluid helium*, while a current of 11,850 A generates a 8.33 T magnetic field to curve the proton trajectory. The *beam acceleration* is generated by 8 radio-frequency cavities situated in the acceleration system of the LHC. At a frequency of 400 MHz they give a potential of 2 MV that accelerates the protons with a 5 MV/m field. The highest energy reached by the LHC is limited by the maximal intensity of the current where the dipole electromagnets and the superconducting coils can operate. Over this limit, the magnetic field produced by the coils cannot maintain the orbit of the LHC.

Another important characteristic of the LHC is the *luminosity* $\mathscr{L}$. It is, with the energy, the other quantity usually used to describe the performances of a particle collider. The expression for the luminosity of two Gaussian-shape beams that collide around the speed of light is :

$$\mathscr{L} = \frac{N_1 N_2 f N_b}{4\pi\sigma_x\sigma_y}, \tag{1.1}$$

where

- N_1 and N_2 are the number of particle per bunch for the two colliding proton beam 1 and 2, respectively.
- f is the revolution frequency in the LHC.

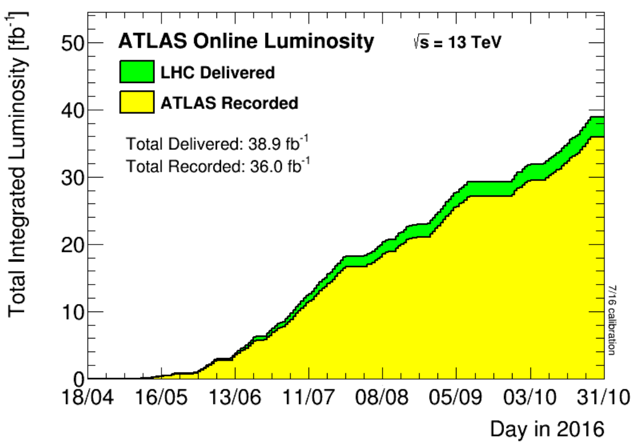

Figure 1.2: Cumulative luminosity vs time delivered to (green) and recorded by ATLAS (yellow) during stable beams for pp collisions at 13 TeV centre-of-mass energy in 2016.
(Source : ATLAS public results : https://twiki.cern.ch)

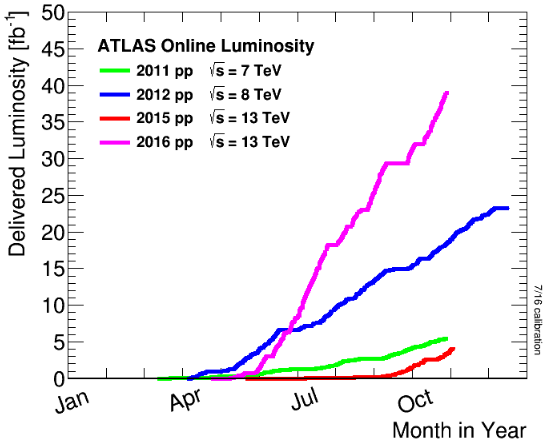

Figure 1.3: Cumulative luminosity vs day delivered to ATLAS during stable beams and for high energy pp collision at $\sqrt{s}$ = 7, 8 and 13 TeV for 2011-2016 (p-p data only).
(Source : ATLAS public results : https://twiki.cern.ch/)

- N_b is the number of bunches.
- σ_x, σ_y are the beam size at collision point in the horizontal and vertical directions, respectively.

It is usual to introduce the integrated luminosity $\mathscr{L}_{int} = \int \mathscr{L}(t)dt$ expressed in invert femtobarn $1\ \text{fb}^{-1} = 10^{39}\ \text{cm}^{-2}$. The fig. 1.2 is a plot that represents the cumulative luminosity as determined from counting rates measured by the luminosity detectors. The comparison of the recorded luminosity versus the delivered luminosity reflects the *Data Acquisition* (DAQ) inefficiency. The fig. 1.3 shows the history of the integrated luminosity during Run 1 (2011-2012) and Run 2 (2015-2016).

1.2.2 High Luminosity LHC

At the end of the Run 2 (fig. 1.4), the LHC is expected to deliver an *integrated luminosity* of $\mathscr{L}_{int}$ = 100 pb^{-1} corresponding to O(10^{32}) events in total recorded by the ATLAS detector. The analysis that occurs at the ATLAS experiment concerns extremely rare processes. For example, the current analysis on Higgs pair production processes makes drastic cut on all the data recorded in Run 1 and Run 2 while the results are only based on few events [2].

This situation of the low integrated luminosity raised the necessity to upgrade the LHC and has given rise to the *High Luminosity LHC* (HL-LHC) project [3]. The goal is to collect 3,000 fb^{-1} by 2037[1] in order to enhance the potential for new discoveries at LHC. This rate corresponds to an *instantaneous luminosity* of $\mathscr{L} = 5 \times 10^{34}\ \text{cm}^{-2}\ \text{s}^{-1}$, increasing the number of *pile-up*[2] to about 140 pp collisions per bunch crossing, compared to about 28 in the current run.

To handle this high rate, it is necessary to raise the space measurement precision of the particles, particularly in the *Inner Detector* (Sec. 1.3.2) due to its proximity with the collision point. This leads to major challenge due to extremely high detector occupancy, radiation damage and data transmission requirements (Sec. 1.4).

[1] which is about 300 times the current integrated luminosity (fig. 1.2 and 1.3)
[2] A situation where a particle detector is affected by several events at the same time.

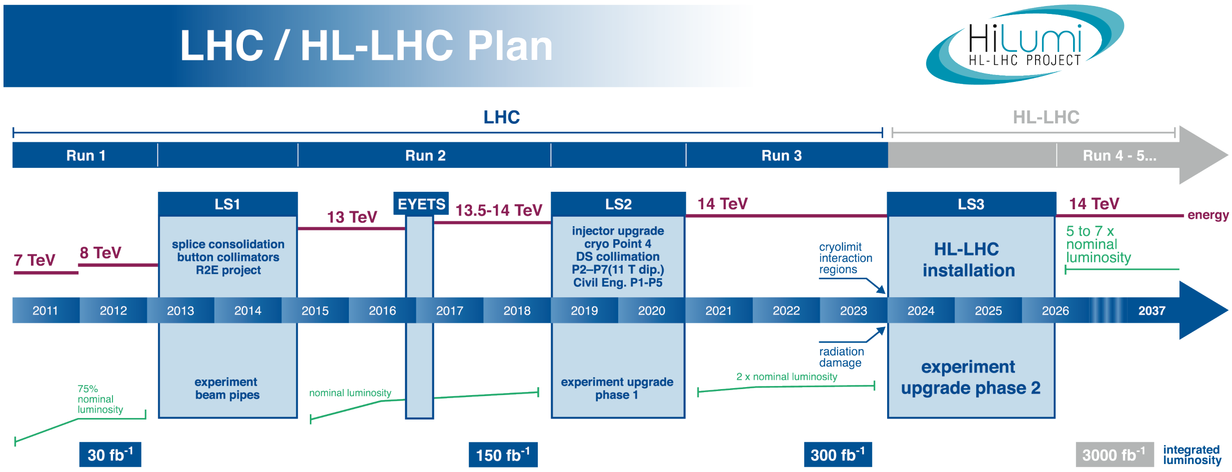

Figure 1.4: Detail of LHC runs, shutdown and prospects of the High Luminosity LHC
(Source : The HL-LHC Project : http://hilumilhc.web.cern.ch/)

1.3 The ATLAS Experiment

The *ATLAS collaboration*[3] is composed of over 3,000 physicists including 1,000 students represented by 177 universities and laboratories in 38 countries worldwide. The ATLAS experiment [4] is searching for new discoveries from *collisions of protons* at an extremely high energy. The detector (fig. 1.5) is 44 meters long for 25 meters wide and the weight is about 7,000 tons.

1.3.1 The sub-detectors

The structure is decomposed in several *sub-detectors*, divided themselves into different layers under a concentric cylindrical geometry. The central part around the beam pipe is named *barrel*, it is surrounded by several pairs of discs named *end-caps* perpendicular to the beam. The result is an hermetic detector that detects all particles (at the exception of the neutrinos) with no blind spots. The four main parts of the ATLAS detector are :

- **Muon Spectrometer** : made up of 4,000 individual muon chambers, it surrounds the calorimeter to measures muon paths to determine their momenta with high precision. It consists of thousands of charged particle sensors placed in the magnetic field produced by large superconducting toroidal coils. The sensors are similar to the straws for the inner detector (see section 1.3.2), but with larger tube diameters.The subsections of the Muon System are : **Thin Gap Chambers**, **Resistive Plate Chambers**, **Monitored Drift Tubes** and **Cathode Strip Chambers**.
- **Magnet system** : bends charged particle trajectories around the various layers of detector systems, to measure particle momenta. The main sections of the magnet system are : **Toroid magnets**, a flat superconducting cable located in the center of an aluminum stabilizer with rectangular cross-section and **Solenoid magnet**, designed to provide a 2 T magnetic field in the central tracking volume.

[3] More informations on http://atlasexperiment.org/

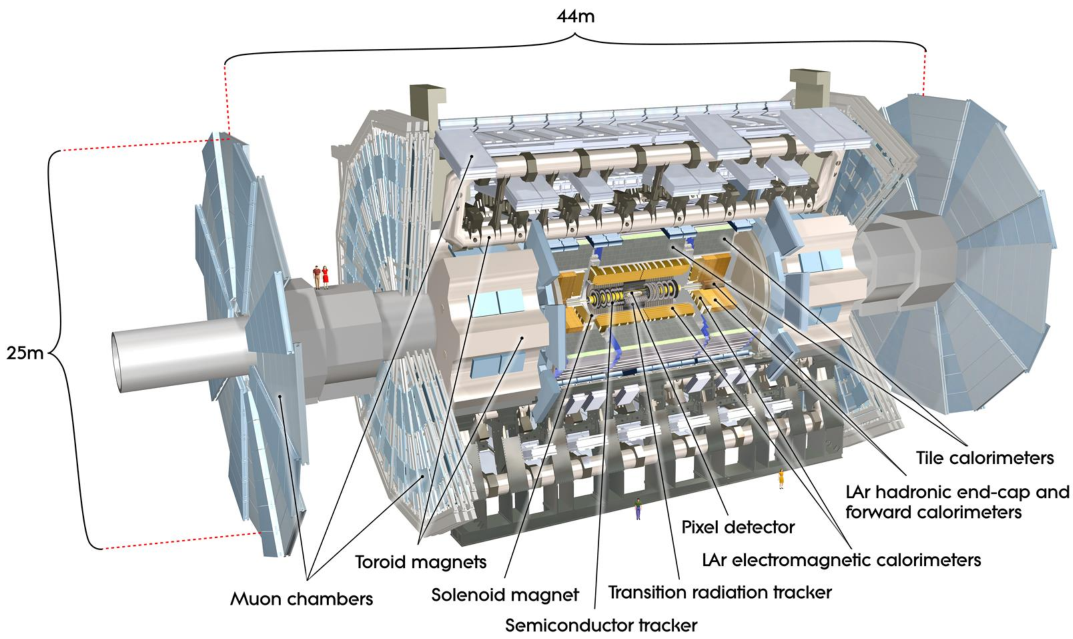

Figure 1.5: Schematic of the ATLAS Detector. See Sec. 1.3.1 for a description of the sub-detectors.
(Source : The ATLAS experiment : http://www.atlasexperiment.org/)

- **Calorimeters** : measures the energy that a particle loses as it passes through the detector. They consist of layers of *absorbing* high-density material interleaved with layers of an *active* medium such as liquid argon. Interactions in the absorbers transform the incident energy into a "shower" of particles that are detected by the sensing elements. The system is composed by : **Liquid Argon (LAr) electromagnetic calorimeter**, **LAr hadronic end-cap and forward calorimeters** and **Tile Calorimeter**.

- **Inner Detector** : measures the direction, momentum, and charge of charged particles produced in each proton-proton collision and reconstructs their trajectory. It is also used to determine the primary and secondary vertices of particle decays. The main components of the Inner Detector are : **Pixel Detector**, **Semiconductor Tracker (SCT)**, and **Transition Radiation Tracker (TRT)**. The next section (1.3.2) gives more details on the Inner Detector.

1.3.2 The Inner Detector

The ATLAS Inner Detector (fig. 1.6) combines high-resolution trackers in the inner layers and continuous tracking elements on the edge. The Central Solenoid provides a magnetic field of 2 T. In the *barrel* region the high-precision detectors are arranged in concentric cylinders, while the *end-cap* detectors are mounted on disks perpendicular to the beam axis. The ATLAS Inner Detector is composed of four sub-detectors :

- **Transition Radiation Tracker (TRT)** : made of 40-70 cm long and 0.5 cm wide thin tubes filled with Xenon gas. In *each tube* runs a single gold-plated *W-Re* wire to detect transition radiation photons created in a radiator between the straws. This detector provides about 30 measurements along a track with a resolution of about 0.2 mm. The barrel section is built of individual

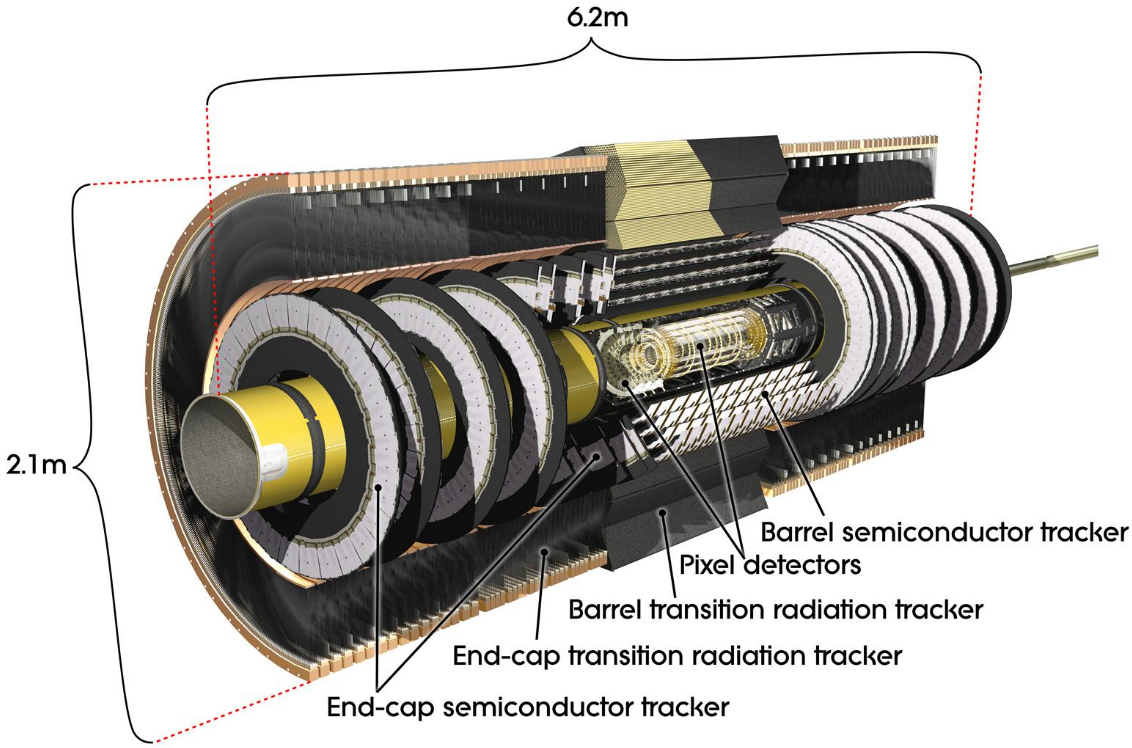

Figure 1.6: The ATLAS inner detector. See text 1.3.2 for a description of its different parts.
(Source : The ATLAS experiment : http://www.atlasexperiment.org/)

modules between 329 and 793 straws each, covering the radial range from 56 to 107 cm. The first six layers are inactive over the central 80 cm of their length to reduce their occupancy. Each end-cap consists of 18 wheels. The innermost 14 cover the radial range from 64 to 103 cm, while the last four extend to an inner radius of 48 cm. Wheels 7 to 14 have half as many straws per cm in the beam direction as the others, to avoid an unnecessary increase of crossed straws and material at medium rapidity.

- **Semi-Conductor Tracker (SCT)** : designed to provide eight precision measurements per track in the intermediate radial range, contributing to the measurement of momentum, impact parameter and vertex position. The SCT is composed of *four layers* of Silicon Microstrip detectors. Each module has four sensors of 6.36×6.40 cm^2 with 768 readout strips of 80 μm pitch. The barrel modules are mounted on carbon-fibre cylinders at radii of 30.0, 37.3, 44.7, and 52.0 cm. The end-cap modules are very similar in construction but use tapered strips with one set aligned radially.

- **Pixel Detector** : provides three precision measurements over the full acceptance, and mostly determines the impact parameter resolution and the ability of the Inner Detector to find short lived particles such as *B-Hadrons*. The system consists of three barrels at average radii of ~ 5 cm, 9 cm, and 12 cm (1456 *modules*), and three disks on each side, between radii of 9 and 15 cm (288 modules). Each module is 62.4 mm long and 21.4 mm wide, with 46080 *pixel elements* read out by 16 FE-I3 chips, each serving an array of 18 by 160 pixels. The 80 million pixels cover an area of 1.7 m^2.

- **Insertable B-Layer (IBL)** : consists of 14 staves of 64 cm long each arranged around the beam-pipe with an average distance to the center of beam pipe of 33.25 mm. Because the luminosity increased for Run 2, a new read-out chip named FE-I4 (detailed in Chap. 3) and two different silicon sensor technologies (planar and 3D) were used to be tolerant in the high radiation and the high occupancy.

1.3.3 Characteristics of the ATLAS detector

The following quantities are commonly used in this thesis. They are presented as characteristics of the ATLAS detector but are, in fact, commonly used in particle physics.

Pseudorapidity

The pseudorapidity, η , is a widely used *spatial coordinate* describing the angle of a particle relative to the beam axis. It is defined as :

$$\eta \equiv -\ln\left[\tan\left(\frac{\theta}{2}\right)\right], \tag{1.2}$$

where θ is the angle between the particle three-momentum $\vec{p}$ and the positive direction of the beam axis, defined to be in the direction to the octant 8 of the LHC (fig. 1.1).

Transverse momentum and Missing transverse momentum

The transverse momentum $\vec{p}_T$, is the momentum of an object transverse to the beam. Transverse energy is defined as

$$E_T = \sqrt{m^2 + p_T^2}, \tag{1.3}$$

for an object with mass m and transverse momentum p_T. Events in which the products have large transverse momentum are more likely to be interesting events.

To find particles that escape from the detector, it is possible to indirectly measure their energy. Because the sum of the initial transverse momentum is zero, it is useful to look for *missing transverse momentum* that is defined as :

$$\vec{p}_T^{miss} = -\sum_i \vec{p}_T(i), \tag{1.4}$$

for every detected particle i. *Missing transverse energy* is equivalent to missing transverse momentum only if the missing particle(s) were massless.

Reconstructed mass

The ATLAS detector can measure the energy and momentum of the particles produced in collisions and particle decays. By using those quantities, it is possible to reconstruct the *Lorentz 4-vector* of a particle and hence determine its mass. It becomes then possible to reconstruct the mass of a particle by measuring the energy and momentum of its decay products.

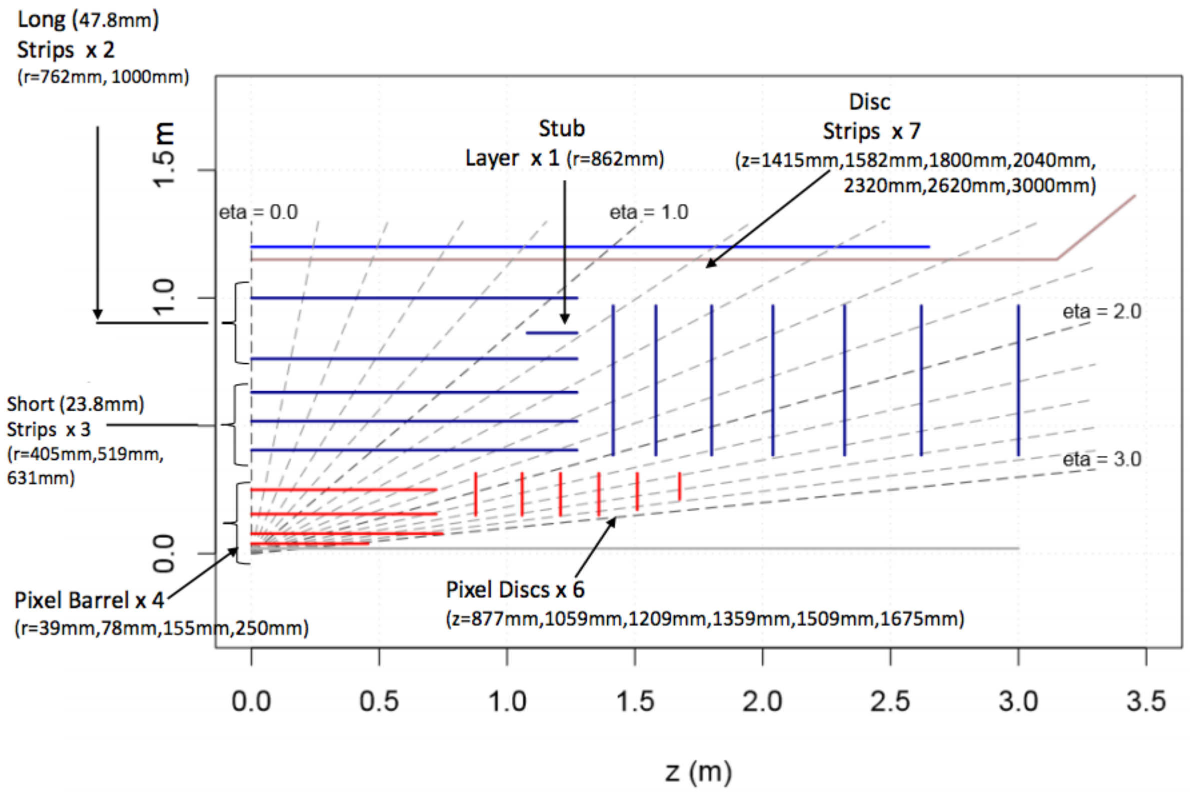

Figure 1.7: : A cross-section of the ITk layout showing coverage of the pixel detector in red and the strip detector in blue. The rapidity coverage extends up to $|\eta| < 2.7$. The blue line outside the ITk volume represents the coil of the solenoid magnet.
(Source : Inspire HEP : http://inspirehep.net/)

1.4 The ATLAS Inner Trackers upgrade for the HL-LHC

As described in Section 1.2.2, the high detector occupancy, radiation damage and data transmission requirements in the HL-LHC upgrade necessitates a replacement of the Inner Detector. Because the Pixel and SCT detectors would seriously degrade in their performance due to the radiation damage of their *sensors* and *Front-End* (FE) electronics, ATLAS has decided to replace the entire Inner Detector with a new, *all-silicon ITk system* [3].

The ITk consists of two types of detectors : *Pixel and Strip* (fig. 1.7) with an area and number of channels given in Table 1.1. This new all-silicon detector will give 14 hits within a pseudorapidity of $\eta = \pm 2.7$ to allow good matching with the muon system [5]. The design was made to optimize the required tracking performance in terms of *fake rate*, *hit efficiency* and *momentum resolution*.

Detector	**Silicon Area** (m^2)	**Channels** (10^6)
Pixel Barrel	5.1	445
Pixel Endcap	3.1	193
Pixel Total	8.2	638
Strip Barrel	122	47
Strip Endcap	71	27
Strip Total	193	74

Table 1.1: The surface area and channel count for the prospects of ATLAS HL-LHC Pixel and Strip Detectors

Intensive R&D studies are in process to develop the most suitable pixel sensor technology. The new FE chip, RD53 [6, 7], will be developed as the next generation of pixel readout chips needed by both ATLAS and CMS at the HL-LHC. It is intended to demonstrate the requirements for *radiation tolerance*, *stable low threshold operation*, and *high hit and trigger rate capabilities*.

The current prototype has a pixel size of $50 \times 50\ \mu\text{m}^2$ to allow sufficiently *fast data transmission* and *low power consumption* while keeping a *reasonable hit occupancies* in the high track density environment on the inner layers. It will require a sensor capacitance (leakage current) less than 100 fF (10 nA) per pixel to provide a lower noise and threshold than the previous chips. It will be designed to keep high performances even after a dose of 500 MRad. A 600 e^- threshold should be efficient for signals from 50 μm path length in silicon for a *Minimum Ionizing Particle* (MIP) . The noise in the chip is estimated to be around 73 e^- *Equivalent Noise Charge* (ENC), depending on the design. The current chip under development, RD53A, is not intended to be a final production for use in an experiment, and will contain design variations for testing purposes, and the characteristics will change in near future.

Kyushu university is preparing to participate to the project of developing new chips for the ITk upgrade. The project presented in this thesis (part II) is the first stone to prepare a *Data Acquisition* (DAQ) system for the future chips. Because those new chips are still under development, the DAQ system was installed for the FE-I4 chip, currently used in the IBL detector. The similarities between the current and future Front End logics will allow a quick way to handle the new FE chips and operate them.

1.5 Structure of the Thesis

The next topics of this thesis are organized as follows. Chapter 2 presents the theoretical context. It gives an introduction to the Standard Model of particle physics and introduce two phenomena responsible for Higgs boson pair production.

The part II regroups Chapter 3 and 4 and concerns the FE-I4 readout chip DAQ System. The Chapter 3 is an overview of silicon detectors, it contains details on the FE-I4 chip and its readout system. The Chapter 4 presents the results for tuning the FE-I4 chip and the algorithm for determining the tuning parameters that maximize data quality.

The part III regroups Chapter 5 and 6 and concerns a qualitative simulation study of the physics case, based on two phenomena involving the rare Higgs production processes. The Chapter 5 presents the simulation process and the event selection for analysis. The Chapter 6 presents the results of Monte Carlo simulation and expectation of the number of Higgs pair production events at the end of Run 2.

Finally, the Chapter IV summaries the results and presents recommendations for further work.

Chapter 2

The Standard Model of Particle Physics

This Chapter introduces the Standard Model of particle physics which describes three of the four fundamental forces of the universe. It includes an overview of the Higgs mechanism, which is responsible for the mass of the particles and describes the production and decays of the Higgs boson. The last part contains an introduction of two phenomena that have not been observed : the Higgs self-coupling and the production of Heavy Higgs particle predicted by the Minimal Supersymmetric Standard Model.

2.1 Introduction

The *Standard Model* (SM) [8] describes a consistent theoretical framework for particle physics in the range of the currently accessible experimental data. Developed along the sixties, this model based on *Quantum Field Theory* associates in the same context elementary particles and their interactions through gauge symmetries for three of the four fundamental interactions : *Electromagnetic*, *Weak* and *Strong*.

2.1.1 Interactions

The fundamental interactions between elementary particles are described by quantum fields which are quantized into vector bosons. The fields behave under group symmetries described by Lie groups. Furthermore, The bosons that transmit the interactions appear after the quantization of those fields, corresponding to a gauge invariance of the Lagrangian. At a quantum level, the SM describes three fundamental interactions :

- **The Electromagnetic Interaction** (EM) is described by a quantum field theory based on the $U(1)$ symmetry group named *Quantum ElectroDynamics* (QED). The quantization of the associated magnetic field B produces a spin 1 gauge field A_μ that corresponds to the mediator of the interaction and is interpreted as the *photon* γ. The gauge invariance symmetry imposes the gauge field to contain no mass term and hence the photon to be a massless particle. The QED coupling constant α expresses a strength for two charged particles to interact under the electromagnetic interaction. This strength is directly related to the fine structure constant $\alpha = 1/137$.
- **The Weak Interaction** was first suggested by Pauli in 1930 to explain the observed violation of energy conservation in β decays by postulating the existence of the *neutrino* ν. In 1956, the Wu's experiment shown from the β decay of cobalt 60 a non observation of *right* helicity neutrinos

[9]. It was the first evidence for parity violation of the weak interaction. The introduction in 1957 of the $V - A$ mechanism by Feynman, Gell-Mann, Marshak and Sudarshan [10] allows the theory to couple the weak interaction only with the *left* part of the particles under the group $SU(2)_L$ where L designates *left* chirality.

The quantization of the weak field produces three new fields W^+, W^- and W^0. As for the EM interaction, the gauge invariance imposes those bosons as well as the fermions to be massless. Nevertheless, the observed mass is restored by Brout-Englert-Higgs mechanism (Sec. 2.1.2). The weak interaction coupling constant (named *Fermi constant*) is of order G_F~1.17×10^{-5} GeV^{-2}.

- **The Strong Interaction** was introduced by Yukawa in 1935 to explain the interaction between the neutron and the proton in the nucleus. In 1961, Gell-Mann, Ne'eman and Zweig explained that the hadrons (particles that interact strongly) are composed of quarks that are the fundamental representation of the group $SU(3)$. The Pauli exclusion principle looked violated after the observation of the hadron Δ^{++} composed of three up quarks. To face the problem, a new degree of freedom was introduced by Greenberg, Han and Nambu in 1965 that opened the way to the *Quantum ChromoDynamics* (QCD). This theory is based on the group $SU(3)_C$ where C means three color charge *red*, *blue* and *green*. The quantization of the corresponding 8 gauge fields G^α_μ ($\alpha = 1,...,8$) are interpreted as the *gluons*, mediator for the strong interaction.

  As for the EM interaction, no mass terms are associated to the gluons. Furthermore, the coupling constant α_S of the strong interaction is too large at low energies to develop a perturbation theory due to the phenomenon of asymptotic freedom, a property that causes bonds between particles to become asymptotically weaker as energy increases and distance decreases. The strong interaction is associated to an energy scale Λ_{QCD} of order 220 MeV.

The intensity of the weak interaction is four order weaker than the EM interaction at low energies. Nevertheless, from an energy of ~100 GeV, the two interaction strength become comparable. This statement is at the origin of a new gauge theory of an electroweak unification by Glashow, Weinberg and Salam [11] during the sixties, experimentally confirmed by the discovery of neutral currents by Gargamelle experiment in 1973 [12]. The electroweak theory is based on the group of symmetry $SU(2)_L \otimes U(1)_Y$ with the EM interaction associated to the hypercharge $Y = 2(Q - I_3)$ defined from the electric charge Q and the weak isospin I_3. The two neutral fields (W^0 and B) mix with an angle θ_W under the mechanism of *spontaneous symmetry breaking* and the associated bosons acquire mass giving a massive pair of charged gauge bosons (W^+, W^-), a massive neutral boson $(Z = W^0 \cos\theta_W - B \sin\theta_W)$, and a massless photon $(\gamma = W^0 \sin\theta_W + B \cos\theta_W)$.

Finally, the SM corresponds to the association of the unified Electroweak interaction with the QCD based on the gauge group $SU(3)_C \otimes SU(2)_L \otimes U(1)_Y$.

2.1.2 The Brout-Englert-Higgs Mechanism

The electroweak unification theory contains four gauge bosons that are massless respecting the gauge invariance of the group $SU(2)_L \otimes U(1)_Y$, in opposition with the massive particles we observe. In order to agree on between theory and experiment, the *Brout-Englert-Higgs* (BEH) mechanism [13, 14] introduces a new field ϕ which is invariant under electroweak gauge transformation and explains that a

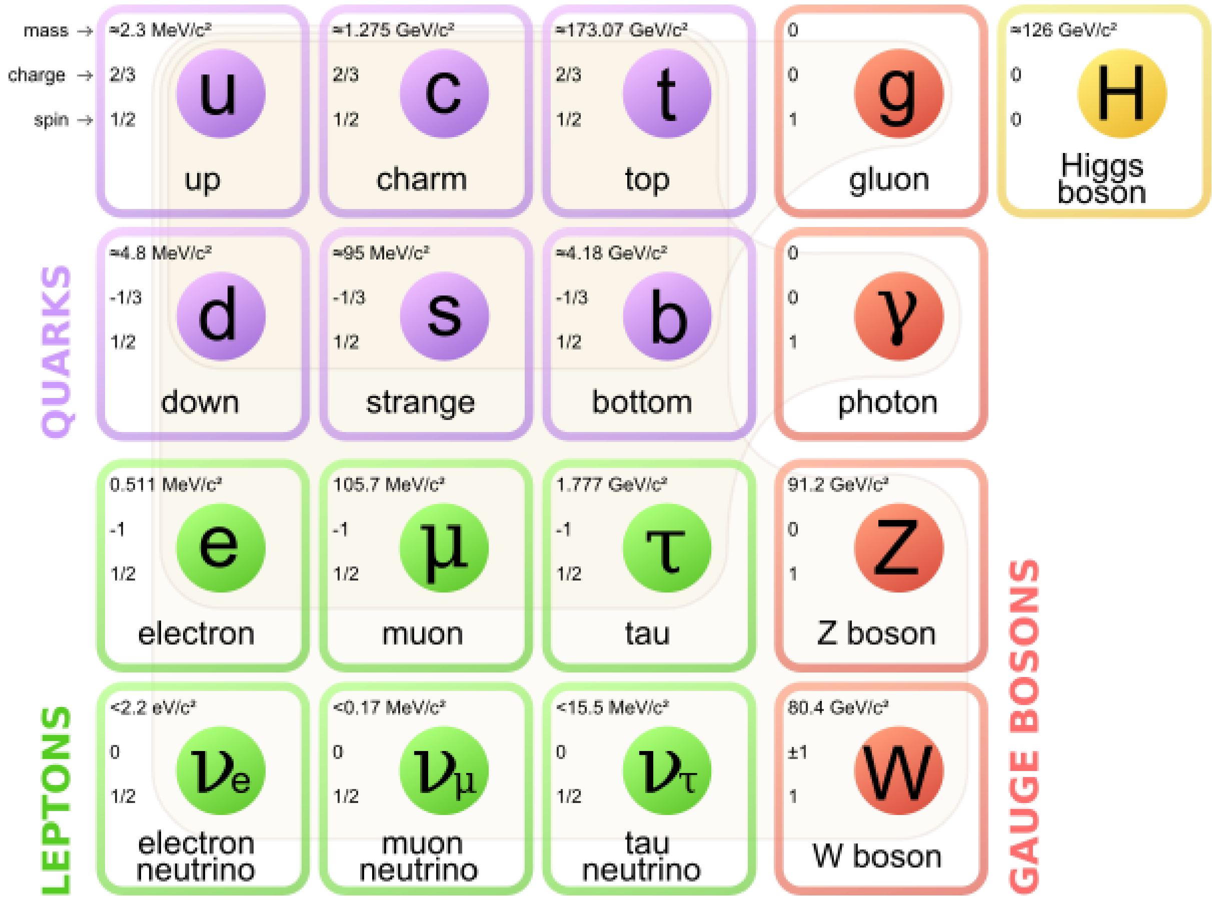

Figure 2.1: SM of elementary particles: the 12 fundamental fermions and 4 fundamental bosons. Brown loops indicate which bosons (red) couple to which fermions (purple and green).
(Source : Wikipedia : https://en.wikipedia.org/)

symmetry breaking of this new field is at the origin of the appearance of the mass of the SM particles. Under this theory, the Lagrangian of the electroweak interaction is then explained by two terms :

$$\mathcal{L}_{EW} = \mathcal{L}_{symm} + \mathcal{L}_{BEH}, \tag{2.1}$$

where $\mathcal{L}_{symm}$ is the symmetric term involving only gauge bosons and fermions and $\mathcal{L}_{BEH}$ is specified by the gauge principle and the renormalizability requirement :

$$\mathcal{L}_{BEH} = (D^\mu\phi)^\dagger(D_\mu\phi) - V(\phi^\dagger\phi) - \overline{\psi}_L\Gamma\psi_R\phi - \overline{\psi}_R\Gamma\psi_L\phi^\dagger \tag{2.2}$$

where the matrices Γ make the Yukawa coupling invariant under the Lorentz and gauge groups. The spontaneous symmetry breaking is obtained for only one *vacuum expectation value*, v. The potential $V(\phi^\dagger\phi)$ is symmetric under $SU(2)_L \otimes U(1)_Y$ and contains quartic terms in ϕ :

$$V(\phi^\dagger\phi) = -\frac{1}{2}\mu^2\phi^\dagger\phi + \frac{1}{4}\lambda(\phi^\dagger\phi)^2 \qquad \text{with} \qquad \mu^2 = -\frac{1}{2}m_H^2 \qquad \text{and} \qquad \lambda = \frac{m_H^2}{v^2}. \tag{2.3}$$

This potential introduces the *vacuum expectation value* $v = \sqrt{-\mu^2/\lambda}$ that appears once the symmetry is broken. Under an adequate gauge transformation, it is possible to rewrite the potential with the form :

$$\phi(x) = \frac{1}{\sqrt{2}}\begin{pmatrix} 0 \\ v + h(x) \end{pmatrix}. \tag{2.4}$$

Here, the scalar field $h(x)$ corresponds to a *spin 0 Higgs boson* and its mass m_H is given by $m_H = \sqrt{-2\mu^2} = \sqrt{2\lambda v^2}$. The fact that m_H depends on the free parameter λ makes it not predicted by the SM.

The Higgs boson was the last SM particle to be observed experimentally by the announcement in July 2012 of the observation of a new particle [15, 16] by both ATLAS and CMS experiments (Sec. 1.2). The mass of the Higgs boson m_H is measured to be 125.09 ± 0.24 GeV/c^2 and its properties [17, 18] (spin, parity and coupling) were observed in accordance within the predictions of the SM.

As a conclusion to this section, all the particles of the SM of particle physics, and also their interaction, mass, charge and spin are represented by figure 2.1.

2.1.3 Higgs Production and Decay

The quantitative analysis (Part III) focuses on two phenomena involving rare Higgs pair production. It is required to understand accurately the production and decay processes of the Higgs boson.

Production modes

The Higgs Boson is created by four main processes [19] (fig. 2.2) (by decreasing order of the cross-section ordering) :

① **gluon-gluon fusion (ggF)** has the largest cross-section. The gluons are massless and so do not interact directly with the Higgs boson. In this process, the gluons fuse together with the help of a top quark triangle which merges into the scalar particle.

② **vector boson fusion (VBF)** is the interaction of two (anti-) fermions that both exchange a virtual W or Z boson which produce a Higgs boson.

③ **vector boson associated Higgs (VH)** also called **Higgs Strahlung** is possible when two fermions collide to merge into a virtual W or Z boson which, if it carries enough energy, can emit a Higgs boson.

④ $t\bar{t}$ **associated Higgs (ttH)** or **top fusion** has by far the smallest cross-section. This process considers the scenario in which both two colliding gluons decays into a quark-antiquark pair. A quark and antiquark from each pair can then recombine to form a Higgs boson.

The ggF production process is several orders larger than the others and only this creation process is considered in the analysis of Higgs pair production (Sec 2.2).

Decay modes

The Higgs boson, as other heavy SM particles, decays to lighter particles under the predictions of quantum mechanics. The discovery of a Higgs boson in 2012 allowed to fix its mass to $125.09 \pm$

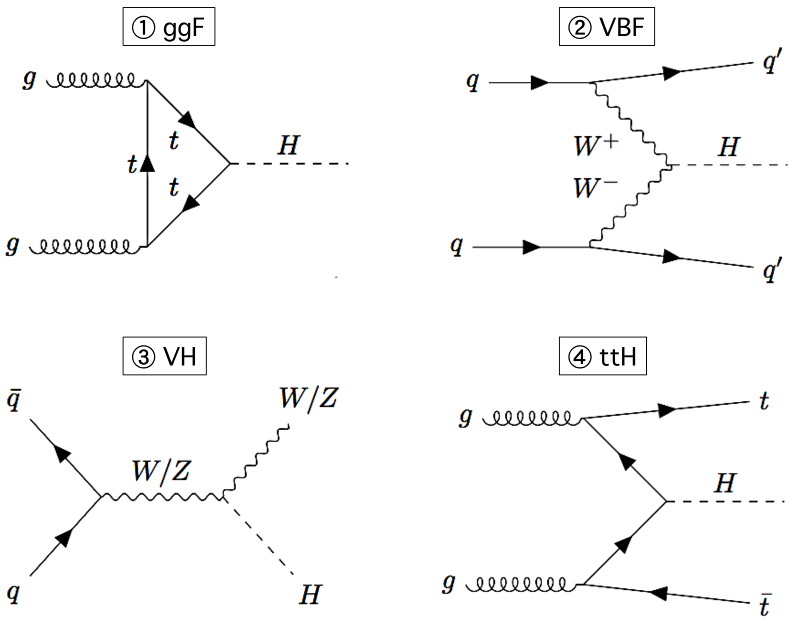

Figure 2.2: Feynman diagram of the four Higgs boson creation processes

0.24 GeV/c^2 (Sec. 2.1.2) and determine its lifetime[1] to be 1.6×10^{-22} s. Since the Higgs boson interacts with all massive particles, there are many possibilities for its decay.

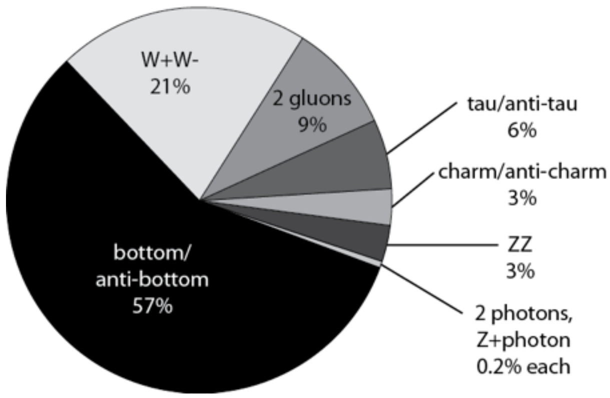

Figure 2.3: Diagram of the 125 GeV SM Higgs boson decays
(Source : University of California : http://sites.uci.edu/)

The SM Higgs boson is too light to decay into a top-quark pair. As shown in fig. 2.3, more than the half of the Higgs bosons decays into a pair of bottom-antibottom quarks. The decay into a pair of photons through top quark loop concerns only 0.2%. This decay mode is carefully studied since it gives a clean signature in the detector.

2.2 Beyond The Standard Model

Even though the SM is currently the best description of the universe, the SM does not explain the complete picture. Many questions remain unclear concerning the Higgs boson. The analysis part

[1] In the SM, the total decay width of a Higgs boson with a mass of 125.09 ± 0.24 GeV/c^2 is predicted to be 4.21×10^{-3} GeV. The mean lifetime is given by $\tau = \hbar/\Gamma$

of the present research (part III) concerns two processes that are not observed yet, the *Higgs boson self coupling* and the theories involving *Two Higgs Doublet Model* (2HDM) where several *heavy Higgs bosons* are postulated.

2.2.1 Higgs self-coupling

The observation of the Higgs boson by both ATLAS and CMS experiments opened a new way : it becomes important to measure accurately the proprieties of the Higgs boson and to understand precisely the *electroweak symmetry breaking* (EWSB) mechanism [1]. Many measurements need to be performed to measure its intrinsic properties (the mass, the spin-parity quantum number and the total decay width) and its coupling to fermions and gauge bosons in order to verify their mass relatively to the fundamental prediction from the BEH mechanism. Nevertheless, those measurements do not allow a deep understanding of the mechanism itself. The only way to reconstruct the scalar potential (Eq. 2.3) of the Higgs doublet field ϕ that is responsible for EWSB is to probe the Higgs self-interaction.

Rewriting the Higgs potential in terms of a physical Higgs boson leads to the trilinear Higgs self–coupling[2] :

$$\lambda_{HHH} = \frac{3M_H^2}{v}. \tag{2.6}$$

This coupling is only related to the mass of the Higgs boson and is experimentally accessible only by probing double Higgs production [21]. The four main classes of processes for Higgs boson pair production at Hadron collider are represented in the figure 2.4. They correspond to the four classes of single Higgs boson production as discussed in section 2.1.3.

Due to the production of two heavy particles in the final states, the cross-sections for these processes are much smaller than those for single Higgs boson production. As in Table 2.1, the largest cross section is given by the ggF production mode which is one order of magnitude larger than the VBF. All the processes are about 1000 times smaller than the single Higgs production channels. This implies that **high luminosities are required to probe the Higgs pair production** at the LHC.

$\sqrt{s}$ [TeV]	$\sigma^{NLO}_{gg\to HH}$ [fb]	$\sigma^{NLO}_{qq'\to HHqq'}$ [fb]	$\sigma^{NNLO}_{q\bar{q}'\to WHH}$ [fb]	$\sigma^{NNLO}_{q\bar{q}\to ZHH}$ [fb]	$\sigma^{LO}_{q\bar{q}/gg\to t\bar{t}HH}$ [fb]
8	8.16	0.49	0.21	0.14	0.21
14	33.89	2.01	0.57	0.42	1.02

Table 2.1: The total Higgs pair production cross sections (in fb) for the main channels at the LHC [1]. The values are given for center of mass energies of 8 TeV (LHC Run 1) and 14 TeV (LHC Run 2) with $m_H = 125$ GeV

[2]This coupling is obtained by developing the potential of eq. 2.4 around the vacuum after spontaneous symmetry breaking by supposing $h(x) << v$ [20] :

$$\begin{aligned} V(h(x)) &= 2\lambda v^2 \frac{h^2(x)}{2} + 6\lambda v \frac{h^3(x)}{3!} + 6\lambda \frac{h^4(x)}{4!} - \frac{v^4\lambda}{4} \\ &\equiv M_H^2 \frac{h^2(x)}{2} + \lambda_{HHH} \frac{h^3(x)}{3!} + \lambda_{HHHH} \frac{h^4(x)}{4!} - \frac{v^4\lambda}{4} \end{aligned} \tag{2.5}$$

The quadrilinear Higgs coupling λ_{HHHH} can only be observable in triple Higgs production which is far beyond the scope of current experimental research. The cross-section for this process is considered negligible in the present work.

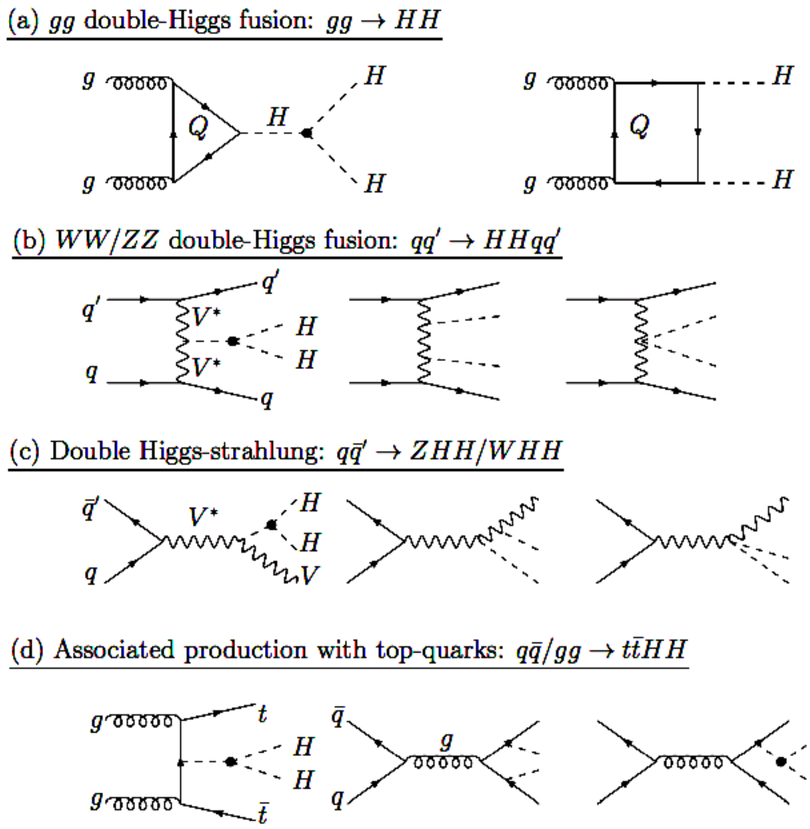

Figure 2.4: Feynman diagrams of the lowest order Higgs boson pair production at Hadron collider [1]

2.2.2 Two Higgs Doublet Models (2HDM)

After the announcement of the observation of a 125 GeV/c^2 particle, research focused on its properties to determine whether or not it is consistent with the *SM Higgs Boson*. In that case, it is the simplest manifestation of the BEH mechanism.

The other types of Higgs bosons are predicted by the other models that go beyond the SM. Several theories are based on 2HDM [22]. One of them, the *Minimal Supersymmetric Standard Model* (MSSM) requires an additional Higgs doublet. In this case, one doublet would couple with up-type quarks and the other to down-type quarks [23, 24, 25]. A pair of doublet means the prediction of five Higgs particles : two CP-even Higgs boson (a light h and a heavy H), one CP-odd Higgs boson (A) and two charged Higgs bosons (H$^{\pm}$) [26, 27].

The masses and coupling of all those particles can be expressed in term of **only two** parameters, often chosen to be the **mass of the pseudoscalar boson** m_A and the **ratio of the vacuum expectation values** v_u and v_d [3] of the neutral component of the two Higgs doublet field, $\tan\beta = v_u/v_d$, by the relations :

$$m^2_{h,H} = \frac{1}{2}\left((m^2_A + m^2_Z) \mp \sqrt{(m^2_A - m^2_Z)^2 + 4m^2_A m^2_Z \sin^2 2\beta}\right), \tag{2.7}$$

$$m^2_{H^\pm} = m^2_A + m^2_W, \qquad \cos^2(\beta - \alpha) = \frac{m^2_h(m^2_Z - m^2_h)}{m^2_A(m^2_H - m^2_h)}, \tag{2.8}$$

[3] By analogy with eq. 2.5.

where $m_{h,H}$ are respectively the mass of the light and heavy neutral Higgs bosons, $m_{H^{\pm}}$ the mass of the two positively and negatively charged Higgs bosons, m_Z and m_W are the mass of Z and W bosons and α is the mixing angle between the two neutral scalar fields.

Direct searches for neutral *MSSM Higgs boson* have been performed by ATLAS and CMS Collaboration [28, 29]. The scenarios proposed in those searches involve radiative correction that introduces dependencies on the other parameters such as the scale of the *soft supersymmetry breaking mass* M_{SUSY}, the masses of the top quark m_t and the gluino[4] $m_{\tilde{g}}$, the mass parameter of the higgsino μ, the wino M_2 and the third-generation slepton[5], $m_{\tilde{l}_3}$, as well as the third-generation trilinear couplings A_t, A_b and A_τ [30, 31, 32].

In the direct search, the parameters have been fixed so that m_A and $\tan\beta$ only remains free. By fixing M_{SUSY} around 1 TeV and for values of $\tan\beta \lesssim 6$, the Higgs boson mass predictions are lower than the observed value of 125.09 ± 0.21 (stat) ± 0.11 (syst) GeV/c^2. However, the current non-observation of *Supersymmetric* (SUSY) particles at the LHC suggests that M_{SUSY} is much larger than 1 TeV. In this scenario, the observed Higgs boson mass becomes in accordance with the predictions for low values for $\tan\beta$ [33]. By fixing the parameters in this way, the interpretation [34] suggests that the mass of the CP-odd Higgs boson [6] m_A, can be smaller than two times the mass of the top quark $2m_t \sim 350$ GeV/c^2. This means that the decay mode $H \to hh$ has a sizable branching fraction.

2.3 Review of $\gamma\gamma b\bar{b}$ results for Run 1

The results for Run 2 search for Higgs boson pair production in the $\gamma\gamma b\bar{b}$ final state is not published yet. For Run 1 [35], the analysis used 20 fb^{-1} of proton-proton collisions at the center of mass energy of 8 TeV. A 95% confidence level upper bound of the production cross-section times branching ratio was set to 2.2 pb for resonant heavy Higgs production process while expected limit is 1.0 pb. The difference gave a light excess of events corresponding to 2.4 standard deviation from background only hypothesis. Concerning the Higgs self-coupling non-resonant process, the limit range varies from 0.7 to 3.5 pb depending on the resonance mass considered.

[4]The gluino $\tilde{g}$, the higgsino $\tilde{H}$ and the wino are respectively the hypothetical supersymmetric partners of a gluon, a Higgs boson and a W boson.

[5]The third generation sleptons are the superpartners of the third generation leptons tau τ and tau neutrino ν_τ.

[6]The mass of the CP-odd Higgs boson is about the mass of the Heavy neutral Higgs $m_H \sim m_A$.

Part II

Data Acquisition System of the FE-I4 Readout Chip

Chapter 3

The FE-I4 readout chip

As presented in the Section 1.3.2, the FE-I4 chip is used in the IBL detector to detect charged particles which is the innermost layer of the ATLAS detector. This chapter is an overview of the silicon detectors and the data acquisition (DAQ) system of the FE-I4 chip. The section 3.1 introduces the principle of semiconductor detectors and the interaction of charged particles with matter described by the Bethe-Bloch formula. The Section 3.3 presents the specification of the FE-I4 chip. The Section 3.4 describes the analog pixel structure of the FE-I4 chip and explains the digitization of the signal. Finally, the Section 3.2 describes the details of the DAQ system to operate the FE-I4 chip.

3.1 Principle of semiconductor detectors

Semiconductors are material with very unique properties and are widely used in electronics and particle detection. This Section presents the fundamental properties of semiconductors to understand the charge response of the sensor which a charged particle is passing through.

3.1.1 p-n junction

The *p-n junction* forms the basis of the semiconductor electronic devices and sensors. In semiconductors, such as *Silicon* (Si), the molecular structure is periodic whereby each atom is surrounded by 4 valence electrons. The number of electrons in a silicon lattice can be shifted by doping them to change its electrical properties. there exist two types of doping to change the electrical neutrality of the silicon :

- **p type** : The group III atoms in the periodic table have only three valence electrons. When silicon is filled by those material, not enough electrons are present to assure the electrical neutrality of the material. The lack of an electron makes a hole, that is interpreted as a positive free charge carrier.

- **n type** : The n-type material is made by doping the semiconductor with atoms of the group V in the periodic table, containing 5 or more valence electrons. The presence of those atoms in the silicon lattice results in a free electron in the conduction band .

When two types semiconductor materials are joined together, a large electron and hole density gradient appears at the *p-n junction* (Fig. 3.1). The result is a diffusive migration of electrons and holes to each sides of the junction creating a "*depletion region*", created by two net oppositely charged regions. The electric field appeared prevent charge carriers from crossing the depletion region.

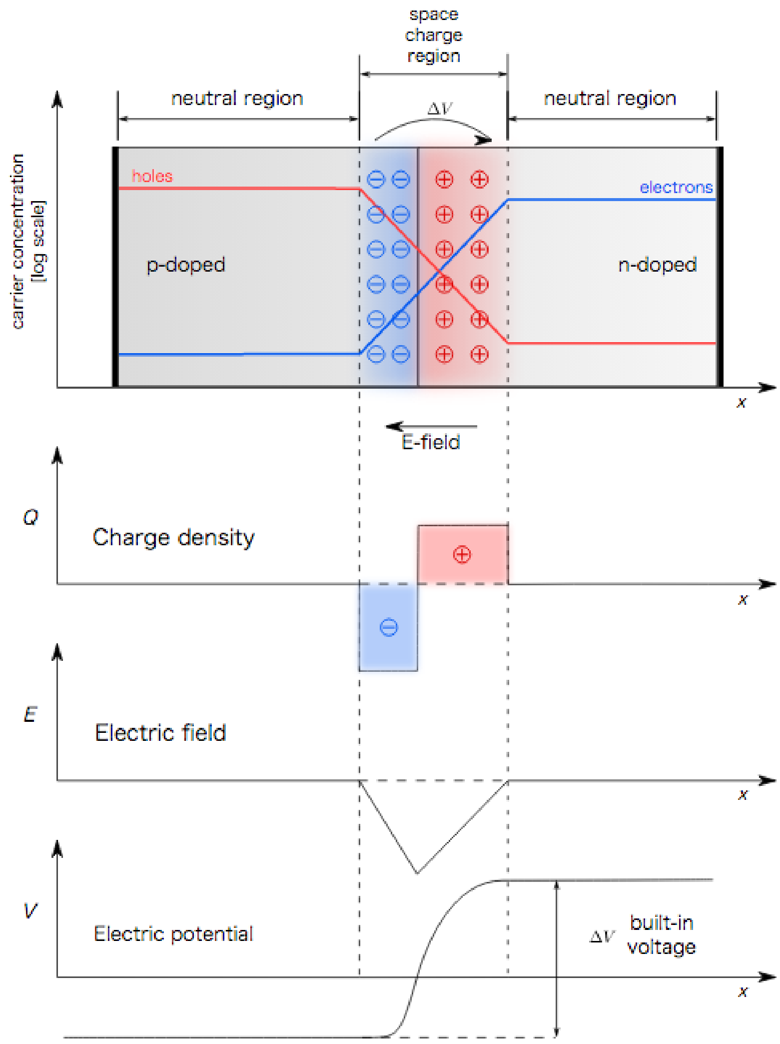

Figure 3.1: p-n junction in thermal equilibrium with zero bias voltage applied. Electron and hole concentrations are shown respectively as blue and red lines. Gray regions are charged neutral. Light red zone is positively charged and light blue zone is negatively charged. The bottom three figures are plots for the charge density, the electric field and the potential, respectively.
(Source : Wikipedia : https://en.wikipedia.org/)

3.1.2 Charged particles detection in semiconductors

The Coulomb interaction of a charged particle that crosses over the depletion region creates electron/hole pairs in the silicon crystal. The pair will not recombine due to the electric field but will drift away to the p-doped and n-doped regions. The signal generated in a silicon detector is essentially a function of *the energy loss* (dE/dx) of the particle in the semiconductor layer and *the thickness of the depletion zone.*

Energy loss

The detection of a particle is made by observation of the ionization energy loss dE/dx left behind by charged particle passage. The average energy loss by a charged particle in a medium is given by the Bethe-Bloch formula [36] :

$$-\frac{dE}{dx} = 4\pi N_A r_e^2 m_e c^2 z^2 \frac{Z}{A}\frac{1}{\beta^2}\left[\frac{1}{2}\ln\left(\frac{2m_e c^2\beta^2\gamma^2 T_{max}}{I^2}\right) - \beta^2 - \frac{\delta(\gamma)}{2}\right], \tag{3.1}$$

where

N_A	Avogadro's number
r_e	classical electron radius : $e^2/(4\pi\epsilon_0 mc^2)$
$m_e c^2$	mass-energy of the electron
z	charge of the incident particle
Z	the atomic number of the medium
A	the atomic mass of the medium
T_{max}	maximum kinetic energy which can be transfered to a free electron in a single collision
I	mean excitation energy in the material
δ	density effect correction
β^2	$1-(1/\gamma^2)$
γ	E/mc^2
m	mass of the incident particle

The minimum of −dE/dx appears around $\beta\gamma = 3$. That corresponds to the most prominent part that expresses the minimum deposit of energy. The noise in the detector should be well below this energy to detect the *Minimum Ionizing Particles* (MIP). This theoretical aspect is the starting point for the determination of the signal charge and the noise in the pixel detectors. The application to the FE-I4 chip is discussed in Section 4.1.

Thickness of depletion zone

When a voltage is applied across the junctions, more electrons (holes) accumulate on the cathode (anode). To increase the ionization signal charge and promote particle detection, it is necessary to apply reverse bias voltage. i.e. a negative (positive) voltage on the p-junction (n-junction) to enlarge the depletion region.

The ATLAS pixel detector and Insertable B-Layer uses Silicon sensors. This material is the standard in high energy physics for vertex and tracking detectors.

3.2 The data acquisition system

Kyushu University's experimental particle physics laboratory is currently creating a project to handle and develop the next generation semiconductor readout chips for the HL-LHC ATLAS pixel detector. The DAQ system described here is the starting point to manipulate the new chips. It is used for various tasks and the readout (Data structure, Tuning, Control, etc.) for the currently used FE-I4 chip (detailed in Sec. 3.3) is general for pixel detectors. Furthermore, the future RD53 chip are in development and expected to be ready for the first tests by the end of 2017. The installation of the DAQ system and the tuning of the chip (Chap. 4) will allow a quick operation once the new chips are ready.

The figure 3.2 is a graph that shows the different parts of the DAQ system for FE-I4.

- **FE-I4 Board** : The FE-I4 board was developed for testing purposes by the University of Bonn. It provides connections with Ethernet protocol to communicate with the SEABAS2, and connections for power supply.

  ⓐ FE-I4 chip

  ⓑ KEL connector

  ⓒ Power supply

  ⓓ Ethernet port to connect with Daughter Board

  The power supply connections are the digital VDDD = +1.5 V with current limit 0.4 A and the analog current VDDA = +1.5 V with current limit 0.7 A. The board also provides connections for test and debugging purposes. Finally, the chip ID connection allows to control several FE-I4 chips in parallel.

  In the case several chips are connected to the same port (e.g. multiplexer), Chip ID is required to recognize each chip. Three pins of the FE-I4 chip (`Cmd_ChipId_P<0>`, `Cmd_ChipId_P<1>` and `Cmd_ChipId_P<2>`) can be connected to either ground or VDDA power supply. The three bit binary number gives `Chip_ID` between 0 and 7. If a pad is left unconnected, an internal resistor gives the value 0. Because this research concerns only single chip operation, for simplicity the chip ID of the operated chip is left as 000.

- **Daughter Board** : is used to connect simultaneously 4 FE-I4 boards to the SEABAS-2 Board via a KEL 100-pin connector.

  ⓔ Ethernet port 0 to connect with FE-I4 Board

  ⓕ NIM port 0 to extract data out from FE-I4

  ⓖ Ethernet and DOUT NIM ports 1, 2 and 3 to connect several FE-I4 boards simutaneously

  ⓗ Power in (taken from SEABAS2)

  ⓘ Connectors to USER FPGA pins

- **Xilinx Platform Cable** : provides integrated firmware to configure Xilinx FPGAs and programming of Xilinx devices. A *Field-Programmable Gate Array* (FPGA) is an integrated circuit designed to be configured by a customer or a designer after manufacturing. The Xilinx ISE[1] software is used to program and inject the firmware into the FPGA.

  ⓙ Xilinx Platform Cable model DLC10

  ⓚ USER FPGA firmware injection connector

  ⓛ USB connection to PC with Xilinx ISE Software

- **SEABAS2 Board** : The SEABAS2 Board is detailed in the next Section 3.2.1.

[1]Details on : https://www.xilinx.com/

ⓜ NIM IN (for trigger signal)

ⓝ NIM OUT (for trigger veto signal)

ⓞ Ethernet connection with DAQ Software

ⓟ Power in

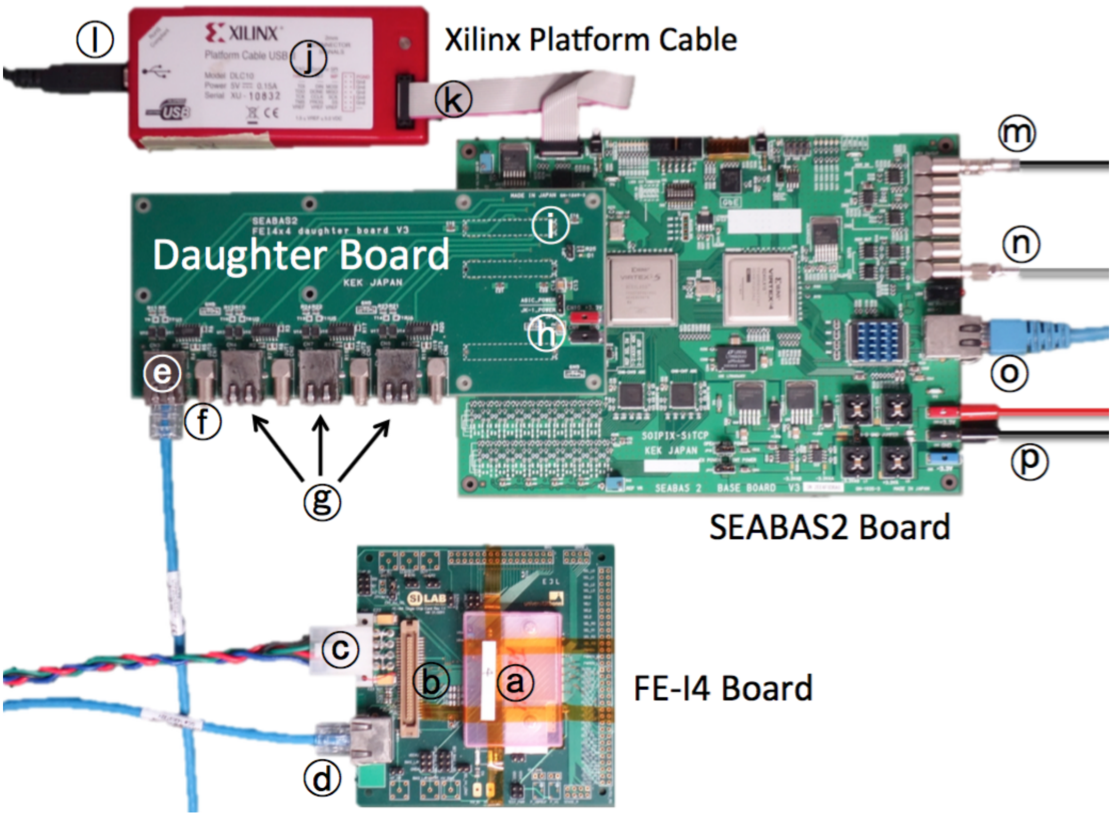

Figure 3.2: Picture of the FE-I4 DAQ system. See text for detailed explanation.

3.2.1 Hardware

The hardware of the DAQ system is composed of three main parts : the SEABAS2 board, the Daughter Board and the FE-I4 board.

The SEABAS2 board

The SEABAS2 board (fig. 3.3) has been developed by the KEK-SOI group for multi-purpose DAQ systems. It contains :

① **USER FPGA** : Xilinx Virtex 5 FPGA [37], contains USER firmware to operate FE-I4 chip.

② **SiTCP FPGA** : Xilinx Virtex 4 FPGA [38], contains the protocol to extract data to the PC.

③ **Firmware injection connector** : The firmware is compiled in an external PC using the software ISE and loaded in the USER FPGA through this connector.

④ **LED** : Firmware modules and FPGA operations are confirmed by the lightning of the LEDs.

⑤ **NIM I/O** : The NIM Standard is used for triggering signals.

⑥ **Ethernet port** : 1Gbps connection between SiTCP (Sec. 3.2.2) and PC

⑦ **Power** : Power supply for SEABAS2 and Daughter Board

⑧ **Connectors to USER FPGA pins** : 120 signal lines from USER FPGA

The connection to the computer uses TCP/IP protocol (see Sec. 3.2.2). The signal coming from USER FPGA is driven through the Daughter Board to provide Ethernet connection to the FE-I4 board. Three pairs of cables are used as positive and negative signal for Command IN, Data OUT and Service.

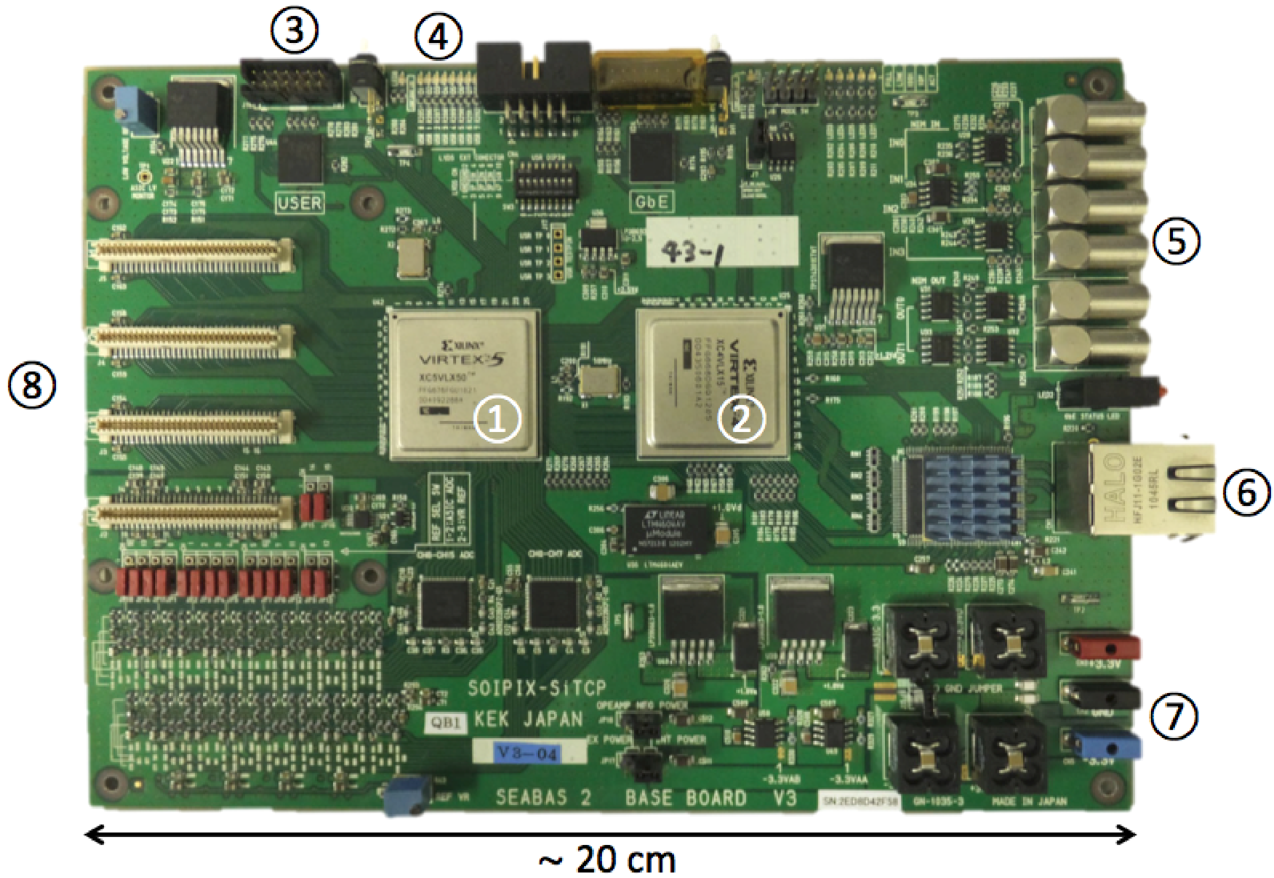

Figure 3.3: Picture of the SEABAS2 (Soi EvAluation BoArd with Sitcp) Board. ① USER FPGA, ② SiTCP FPGA, ③ Firmware injection connector, ④ LED, ⑤ NIM I/O, ⑥ Ethernet port, ⑦ Power, ⑧ Connectors to USER FPGA pins

3.2.2 Firmware

The SEABAS2 contains two FPGAs communicating between themselves. One of them contains the Si-TCP protocol to communicate via Ethernet to the computer. The other USER FPGA contains the firmware for controlling the FE-I4 chip.

Si-TCP FPGA

Si-TCP [39] is a technology to connect front-end to PC via Ethernet. The measurement data is transferred to the computer by writing the data in the FIFO [2] of Si-TCP (located in Si-TCP FPGA's firmware on SEABAS2). By synchronization, the data written in Si-TCP will appear on the PC. On the other hand, the slow control from the PC to the user circuit will be used to write commands from the software in the USER FPGA's FIFO.

USER FPGA

The firmware was written in the language Verilog, currently used to program analog and digital circuits. The tasks for the USER firmware are mainly to send commands and receive data from the FE-I4 board while communicating with the Si-TCP FPGA. The commands contain Run mode, Calibration mode and Trigger that need precise timing.

The firmware is structured in modules, each of which has a designated task. They communicate each others by setting input-output in the code. All modules are contained within the `Top_module` which makes the communication between the USER FPGA and other devices. The modules provide a clock, a communicator containing the TCP/IP protocol, a Decoder to identify header from the data stream received from the control software and a manager for trigger signal. Another important module, `Job_Manager`, contains a signal sender to configure the FE-I4 chip and transmit tuning command or trigger and injection signal. It also manages a signal receiver for data coming from the FE-I4 chip.

3.2.3 Software

The software is ran from the computer through SEABAS2 to control and collect data from the FE-I4 chip. It is written in C++ and is composed of self-sufficient modules (classes). One of the two main modules is the configuration class for chip operations. The configuration class contains Command Generator block to manage the global and local registers of the FE-I4 chip. The other is the the DAQ class, it contains an injection module and a decoder to decrypt the data coming from the FE-I4 chip. The software also provides a SiTCP Controller to provide the TCP/IP protocol necessary to communicate with the firmware.

3.3 The FE-I4 readout chip

Once the *RD53* chip is ready to use it will be important to quickly characterize and operate it in data taking conditions. The RD53 chip is under development. The preparation for the DAQ system was done using the *FE-I4* readout chip, which is used in the IBL detector which is the innermost layer of the ATLAS detector. The samples of the first engineering run (called FE-I4A) have been received in the fall of 2010, while the IBL has been installed to the ATLAS Detector during the Long Shutdown 1 in 2013-2014, as shown on figure 1.4.

[2] FIFO (first in, first out) is a method for organizing and manipulating a data buffer.

3.3.1 General characteristics

The FE-I4 chip [40, 41] is an integrated circuit that contains a readout circuitry for 26,880 pixels of 250×50 μm^2 pitch arranged in 80 columns and 336 rows (fig 3.4). Some characteristics of the chips are given in Table 3.1. The pixel array has bump bond pads with 12 μm width octagonal openings on a 50 μm vertical pitch. The connection from the FE-I4 chip to the FE-I4 board is made with 25 μm thick wire bonding. The wire bonding pads at the bottom come in three sizes : wide (250 μm wide bonding area for high current inputs and outputs), normal (100 μm wide for all other I/O), and narrow (75 μm wide bonding area for diagnostic only).

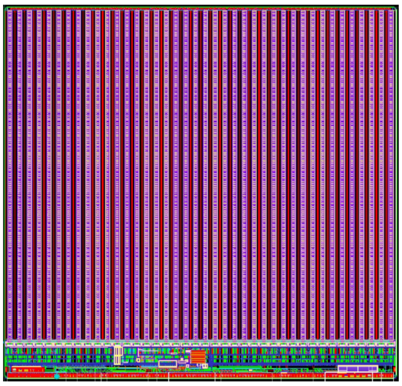

Figure 3.4: FE-I4 chip layout looking down onto the bump pads.
(Source : The FE-I4B Integrated Circuit Guide : https://indico.cern.ch/)

Item	**Value**	**Units**
Pixel size	250×50	μm^2
Pixel array size	80×336	Col × Row
Maximum charge	100,000	e^-
Normal pixel input capacitance	100-500	fF
Edge pixels input capacitance	150-700	fF
In-time threshold with 20 ns gate	≤ 4000	e^-
Hit-trigger association resolution	25	ns
Same pixel two-hit discrimination	400	ns
Tuned threshold dispersion	≤ 100	e^-
ADC method	ToT	
External clock input	40	MHz
Single serial command input	40	Mb/s
Single serial data output	160	Mb/s
Output data encoding	8b/10b	
I/O signals	LVDS	

Table 3.1: Basic specifications of the FE-I4 readout chip.
(Source : The FE-I4B Integrated Circuit Guide : https://indico.cern.ch/)

The FE-I4 columns are divided into 2×2 pixel regions. Each region contains 4 identical analog pixels, ending in a discriminator, and one shared memory that can store up to 5 events. For each event, a counter clocked at 40 MHz keeps track of the time elapsed since the event takes place with 25 ns resolution. The individual discriminator outputs are processed by applying a digital cut on the *Time over Threshold* (ToT) after an analog cut on the threshold.

3.3.2 Output Data Format

The format used is based on a Start of Frame binary sequence, followed by 30 bit word(s) and an End of Frame. The Start of Frame marks the beginning of the transmission of an event. After the Start of Frame sequence, valid record words are Data Header, Address Record, Value Record or Service Record. Data Record word(s) might only be present after a Data Header word. A triggered empty event is recognized by the absence of any Data Records after a Data Header. The main purpose of the End of Frame is to provide some uniqueness in the stream between two events, which can then be used for frame synchronization during heavy data transmission when there may be no Idle States.

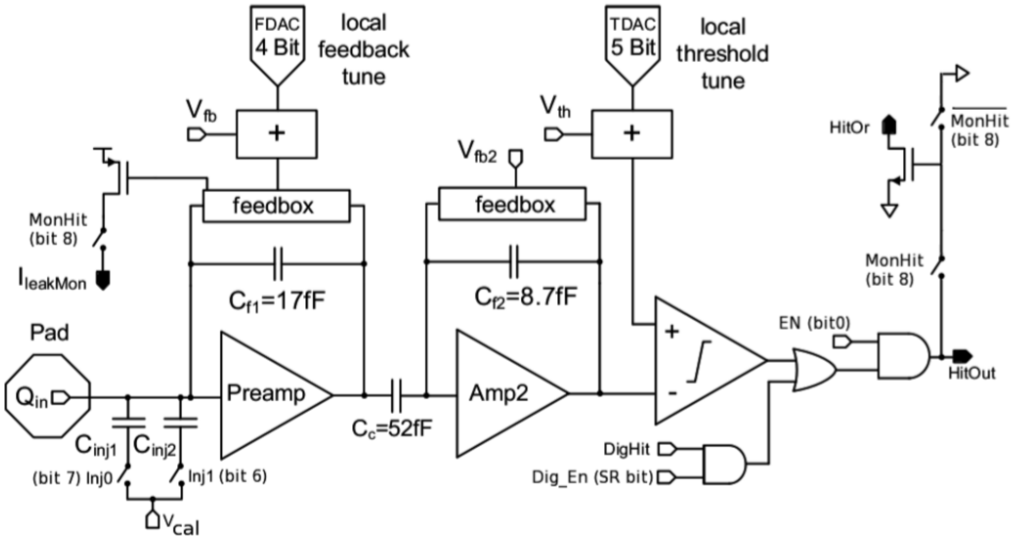

Figure 3.5: Analog pixel schematic diagram of FE-I4 chip.
(Source : The FE-I4B Integrated Circuit Guide : https://indico.cern.ch/)

The protocol also provides an Idle State when no records are pending to be transmitted.

3.4 Pixel Structure

Each pixel contains an independent amplification stage with adjustable shaping, followed by a discriminator with independently adjustable threshold. A good determination of the amplification and discrimination parameters is important to reduce noise and increase data quality.

3.4.1 Amplifier and ToT tuning

The figure 3.5 shows the analog Front-End part which is composed by a two-stage amplifier configuration : a **preamplifier** (i.e. `PreAmp`) followed by a **second stage of amplification** (i.e. `Amp2`). The two stages are used to optimize low power, low noise and fast rise time. The `PreAmp` (first stage) is a cascode amplifier, which consists of a common-emitter stage loaded by the emitter of a common-base stage. It has a high gain, moderately high input impedance, a high output impedance, and a high bandwidth. The `Amp2`, AC coupled to the `PreAmp`, is a folded cascode amplifier. The main motivation of this 2-stage system is to provide enough gain in front of the discriminator while permitting optimization in the choice of the `PreAmp` feedback capacitor (C_{f1}) which is used for ToT tuning.

The global ToT tuning uses a global 8-bit register, `PrmpVbpf`, which controls the master feedback current of the `PreAmp`. The local tuning uses the 4-bit register FDAC in every pixel. A schematic of the `PreAmp` output signal dependences from injected charge, threshold target and feedback current is shown in figure 3.6.

3.4.2 Discriminator and Threshold Tuning

The purpose of the discriminator (fig. 3.5) is to transmit signal whose charge is beyond a threshold value. The output signal is shown in figure 3.6 with its dependancies with charge, threshold and feedback. In order to optimize particle detection, the threshold for all pixels should be uniform. The

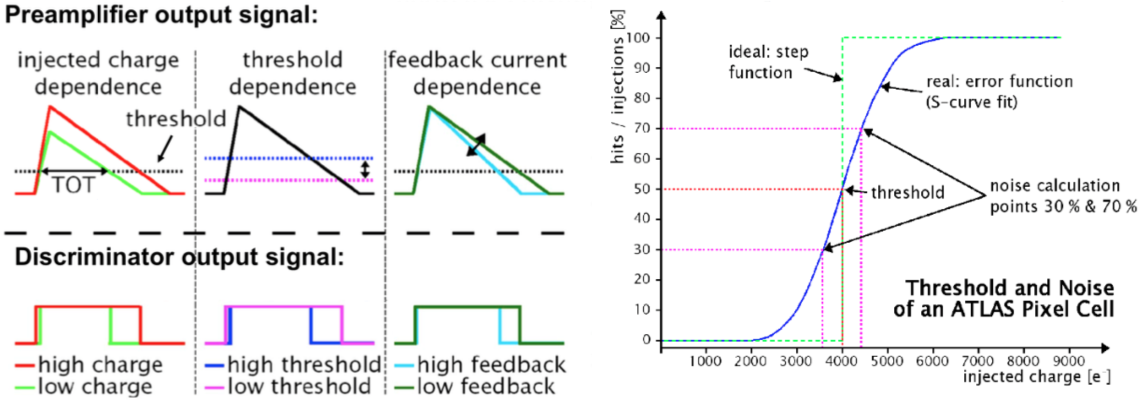

Figure 3.6: On the left, schematic preamplifier and discriminator output signals and their dependencies. On the right, hits/injection distribution function per injected charge for a threshold tuned at 4000 electrons

purpose of the threshold tuning is to set the threshold of each pixel *as close as possible* to the target threshold value.

Due to the noise, the ideal function of figure 3.6 where an immediate transition of the detection efficiency from 0 to 100% at the threshold target never happens. To measure the charge threshold in each pixel, the firmware injects five times a sequence of increasing analog charge from 50 to 5000 electrons. The number of hits is collected for each injection. The number of hits measured for each injected charge results determines the shape of the s-curve of figure 3.6. The response function gives the convolution of the step function. This distribution function is modeled with the normal cumulative distribution function :

$$\text{eff}_{hit}(Q_{inj}) = \frac{1}{2}\left(1 + \text{Erf}\left(\frac{Q_{inj} - Q_{th}}{\sqrt{2}\sigma_{noise}}\right)\right), \tag{3.2}$$

where Q_{inj} is the injected charge, Q_{th} is the threshold and σ_{noise} expresses the Equivalent Noise Charge (ENC) in the chip. The ENC is defined as a hypothetical charge produced in the detector that gives a peak output response equal to the RMS of the noise. The threshold is defined as the injected charge that gives 0.5 of hit efficiency.

In the FE-I4 chip, the threshold can be set by a global and local parameters. The 8-bit global parameter named `Vthin_AltFine` is used to produce a global threshold voltage. The distribution of the threshold average value of all pixels can match a specific target using this parameter. In parallel, each pixel contains a 5 bit register named TDAC. By applying a local voltage via the threshold tuning, every pixel can be tuned independently to the target value. The threshold of each pixel is expected to spread within 100 electrons around the target.

The noise in a silicon detector system is an important feature. It depends on several parameters as the geometry of the detector, the readout electronics, the biasing scheme, etc. In the Chapter 4, the tuning of the FE-I4 chip and the determination of the tuning parameters are made to find the best configuration maximizing performances and reducing the noise of the readout electronics.

Chapter 4

Tuning the FE-I4 Chip

The goal of the tuning is to get the uniform response for all individual pixels to the same analog injection. This Chapter begins (Sec. 4.1) with an estimation of the charge delivered by a Minimum Ionizing Particle (MIP) passing through the sensor. The Section 4.2 presents the results for the determination of the Threshold target that gives the best tuning performances and minimizes the noise in the chip through Global and Local threshold tuning. The Section 4.3 presents the results of Global and Local Time over Threshold tuning. Finally, the Section 4.4 presents the final results by comparing the performances of the selected tuning parameters.

4.1 Signal charge

The charge of the analog injection needs to correspond to a typical particle detection event. In silicon, the minimum energy required to form an electron/hole pair is 3.6 eV. The density of silicon (ρ = 2.33 $g \cdot cm^{-3}$) makes a mean energy loss of about 390 eV.μm^{-1} [36] for a MIP (eq. 3.1). The average number of electron/hole pairs created in 1 μm of silicon after the interaction with a MIP is 108.

The sensor used with the FE-I4 chip is a 200 μm thick silicon semiconductor. Then, when a MIP is passing through, there are about 2.2×10^4 electron-hole pairs created. Furthermore, the most probable energy loss for silicon due to Landau fluctuation is 70% of the mean value, giving an average signal charge of about 1.5×10^4 electrons corresponding to 2.4 fC.

The FE-I4 chip used in the DAQ system described in the previous Chapter is a bare chip : that is not connected to a sensor. The data collected to process Threshold and ToT tuning uses an analog charge injection in each pixel (fig. 3.5), that is equivalent to the signal created from the interaction of a MIP with the 200 μm thick sensor (i.e. 1.5×10^4 electrons).

4.2 Threshold Tuning

As explained in Section 3.4.2, the Threshold can be adjusted by two parameters : One is "`vthin_AltFine`" in the FE-I4 global register to adjust the threshold for all the pixels at once (called GDAC), and the other is a local parameter, TDAC, different for each pixel. The Threshold tuning is operated in two steps (detailed in Sections 4.2.1 and 4.2.2), corresponding to the tuning of those two parameters.

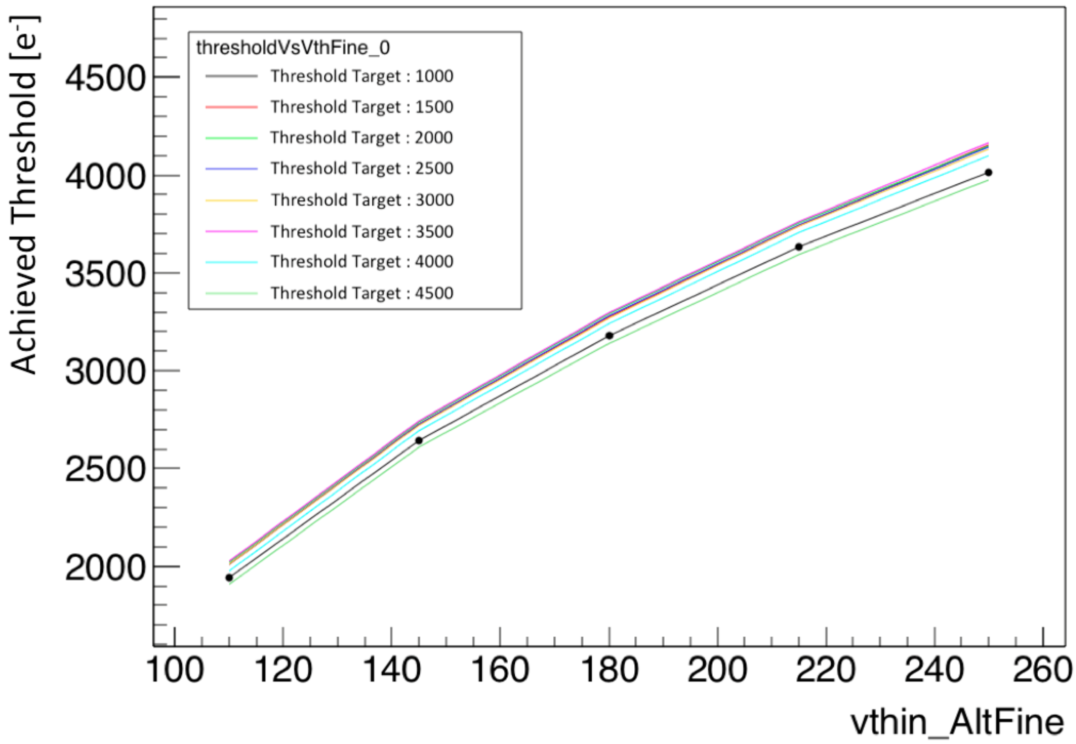

Figure 4.1: `vthin_AltFine` vs achieved threshold for threshold target from 1000 to 4500 electrons. For each threshold target, the GDAC tuning investigates the response of the pixels threshold average value (x axis) to the value of `vthin_AltFine`. The five black points are situated at the five points of measure for `vthin_AltFine` = 110, 145, 180, 215 and 250. They are only shown on the curve where threshold target = 1000 electrons, but the measures were done on those values for all the targets.

4.2.1 Global DAC tune

The GDAC tuning of the chip is made around a threshold target. If the value of the target is *too low*, the fake event rate and noise get larger. On the other hand, if the target value is *too high*, a high charge in the sensor will be needed to be considered as a track, therefore the MIP events might not be detected.

The goal is to find the threshold tuning target that gives the best performances of the FE-I4 chip. A first evaluation of the Global DAC tuning is made for values of the target threshold = 1000, 1500, 2000, 2500, 3000, 3500, 4000 and 4500 electrons. Then, a measurement of the noise for each target is made.

Results

The determination of the value of `vthin_AltFine` is made using figure 4.1. The DAQ software provides a method to find the proper GDAC values to achieve the target threshold. The determination of `vthin_AltFine` value is achieved by setting the target value from the y-axis to the x-axis using the corresponding curve.

The GDAC tuning gives no parameter value for a target lower than 2000 electrons and bigger than 4000 electrons corresponding to `vthin_AltFine` = 110 and 250, respectively. Targets outside this range are expected to give bad performances after the local TDAC tuning (Sec. 4.2.2).

The noise in the chip for the setting of `vthin_AltFine` is shown in figure 4.2. Its value is around 140 ±5 ENC and shows no dependency in this range to the threshold target. For `vthin_AltFine`

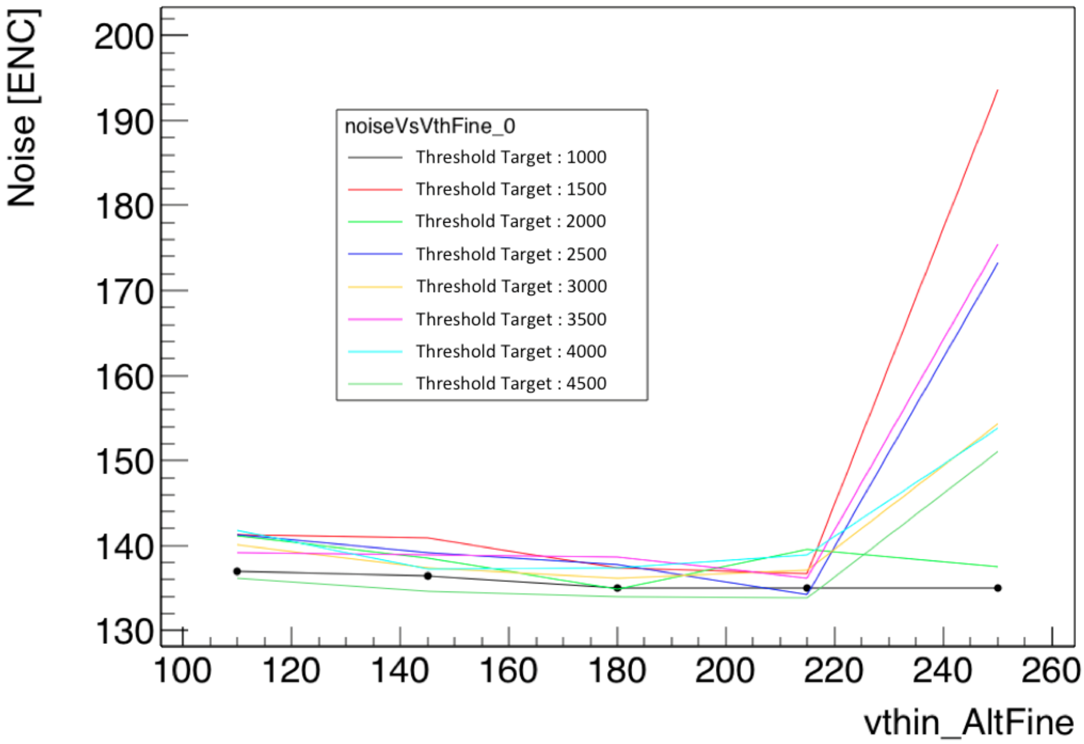

Figure 4.2: `vthin_AltFine` vs noise for threshold target from 1000 to 4500 electrons. The five black points are situated at the five points of measure for `vthin_AltFine` = 110, 145, 180, 215 and 250. They are only shown on the curve where threshold target = 1000 electrons, but the measures were done on those values for all the targets.

> 220 (Fig. 4.2), the noise gives random values. This means that it is preferable to avoid the variable `vthin_AltFine` to be larger than 220.

According to figure 4.1, when the tuning target is set to 4500 electrons, the corresponding setting for `vthin_ AltFine` is larger than 255 which is the maximal value for this variable. Also as in figure 4.2, this region gives a higher noise. The following tuning steps for a target set to 4500 electrons gave very bad performances. Furthermore, as a first selection the threshold target value 4500 electrons is rejected and the following concerns a comparison of the performances for threshold targets set between 1000 and 4000 electrons.

4.2.2 Local TDAC tune

The next step for the tuning of the chip is the local TDAC, to adjust the threshold pixel by pixel. As seen in Section 3.4.2, each pixel contains a 5 bit register named TDAC to tune each pixel independently.

Results

As shown in figure 4.3, the mean value of the pixel threshold distribution before TDAC tuning is set to the target by choosing the appropriate `vthin_AltFine`. The results for the performances of the threshold tuning are shown in table 4.1.

For the three lowest values of the threshold target (1000, 1500 and 2000 electrons), the low range limit of `vthin_Alt Fine` register is reached and the distribution before tuning is similar. The following TDAC tuning necessitates to change the value of each pixel to a higher range, which also reaches

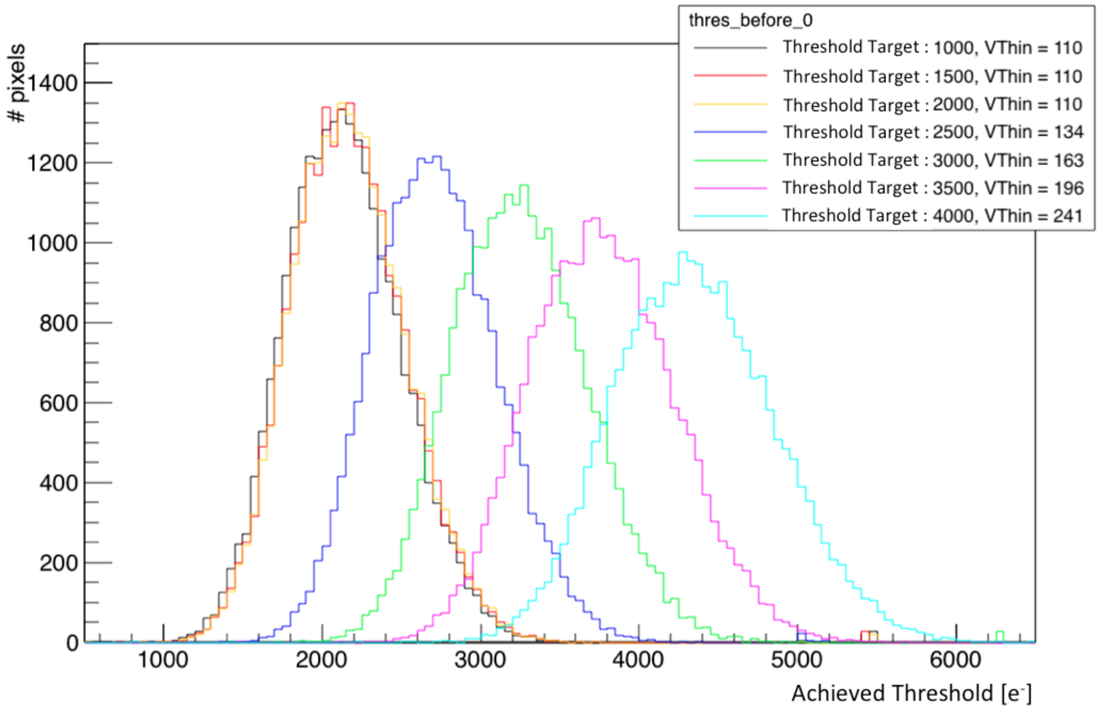

Figure 4.3: Distribution of the achieved threshold for each pixel **before tuning** for threshold target from 1000 to 3500 electrons. The parameter `vthin_AltFine` for each target is also shown.

its limit for some pixels resulting in a tail in the distribution after tuning (fig. 4.4). The performances for those three targets are comparatively low. On the other hand, the highest threshold target (4000 electrons) gives good results on the threshold tuning performances. However, the global threshold tuning set the value of `vthin_AltFine` to be 241. As in figure 4.2, the noise gives a random behavior for `vthin_AltFine` > 220. Therefore, the 4000 electrons threshold target is rejected.

The figure 4.4 shows a distribution of the achieved threshold for six threshold targets. The zoom in the upper part shows that, after rejecting the 4,000 electrons target for the reasons explained above, the best uniformity of the threshold response is given for the threshold target 3,000 and 3,500 electrons. To make a more accurate evaluation of the performances of FE-I4 chip under those settings, the figures 4.5 and 4.6 shows a fitting function in the distribution of the noise for each pixel.

The mean value for the noise is 142.0 ± 0.1 ENC for Threshold = 3000 and 141.2 ± 0.1 ENC for

Threshold Target (e)	`vthin_AltFine`	Mean Threshold (e)	Threshold RMS	Mean Noise (ENC)
1000	110	1054 ± 1.2	181.6	154.8 ± 0.13
1500	110	1507 ± 1.0	151.6	151.5 ± 0.13
2000	110	2002 ± 0.9	137.2	146.3 ± 0.12
2500	134	2508 ± 0.7	113.6	143.8 ± 0.12
3000	163	3003 ± 0.6	98.5	141.8 ± 0.11
3500	196	3502 ± 0.5	83.5	141.0 ± 0.11
4000	241	4024 ± 0.5	77.3	140.2 ± 0.11
4500	n/a	n/a	n/a	n/a

Table 4.1: Results for the threshold tuning for target 1000 to 4500 electrons. From left to right is the target value, the GDAC tuning parameter `vthin_AltFine`, the mean threshold after tuning, the pixel threshold distribution RMS and the mean noise of every pixels. Very low performances for 4500 electron threshold were observed so the results are not shown for this target

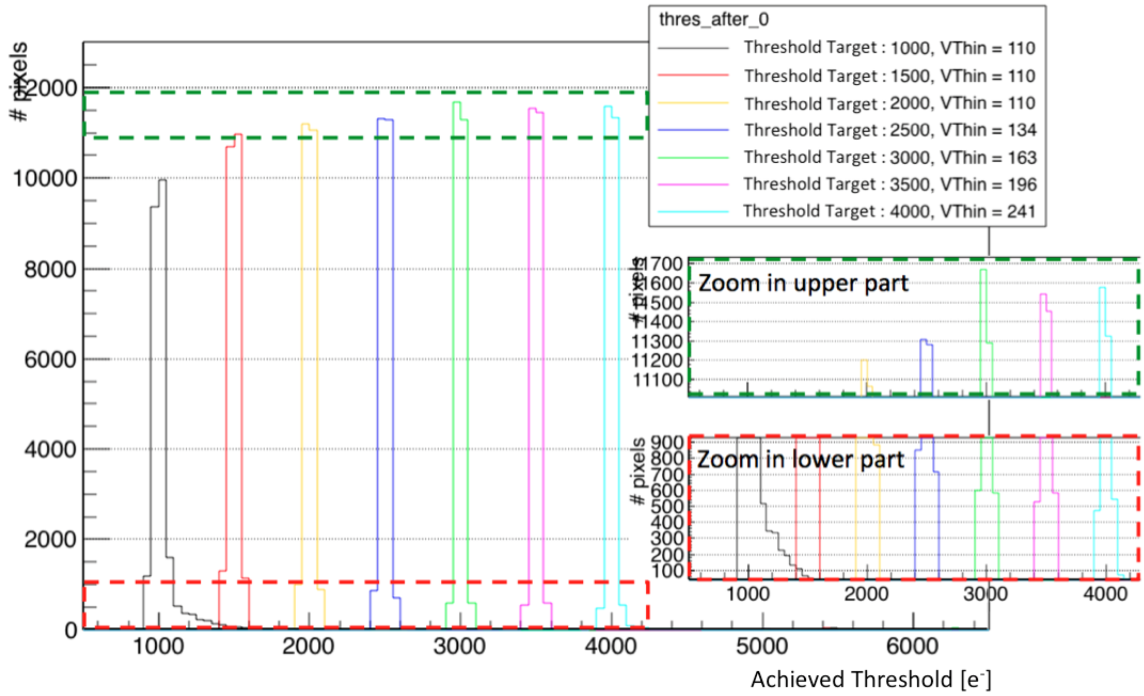

Figure 4.4: Distribution of the achieved threshold for each pixel **after tuning** for threshold target from 1000 to 3500 electrons. The parameter `vthin_AltFine` for each target is also shown.

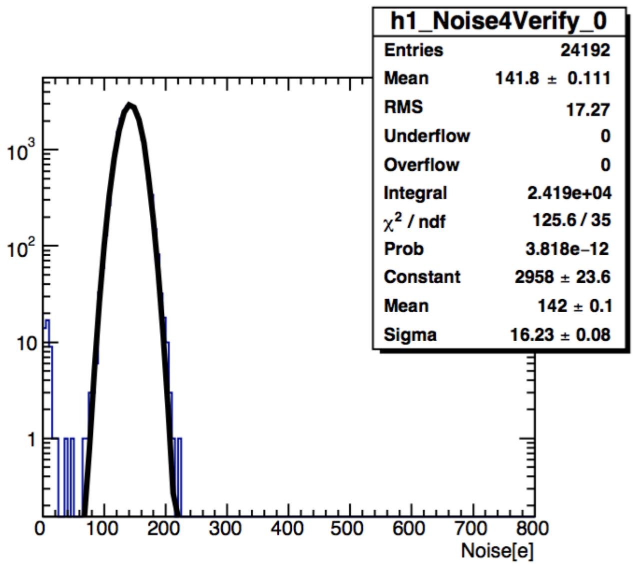

Figure 4.5: Fitting of the repartition of the noise of each pixel for a threshold tuned at **3000 electrons**

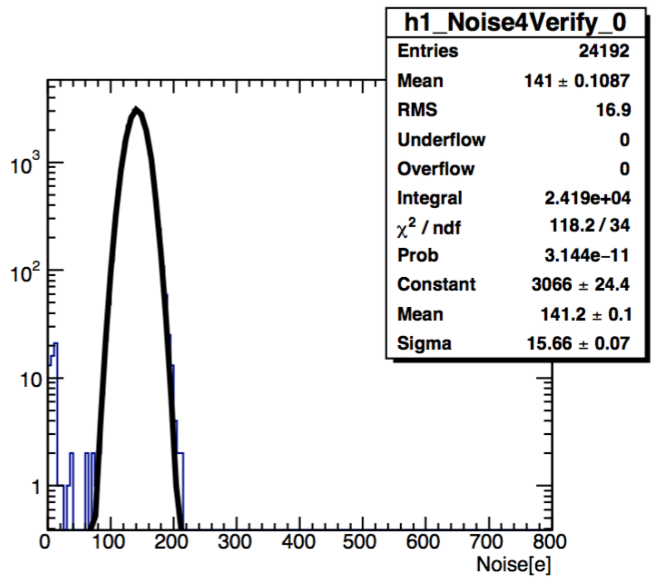

Figure 4.6: Fitting of the repartition of the noise of each pixel for a threshold tuned at **3500 electrons**

Threshold = 3500, showing slightly less noise in the chip tuned at 3500 electrons. This distribution shows also a narrower peak with a standard deviation of $\sigma_{3500} = 15.66 \pm 0.07$ versus $\sigma_{3000} = 16.23 \pm 0.08$, showing a slightly higher stability of the noise in the pixels. The figures 4.5 and 4.6 give also an estimation of the number of dead pixels[1] on the used chip. There are about 20 pixels that give no noise and are considered as dead pixels.

The threshold target setting to 3000 and 3500 electrons seems to give the best performances. For equivalent noise, it is obvious that a lower threshold target is preferable for more sensivity to detect particles. The threshold target that optimizes the performances of the FE-I4 chip is found to be 3000 electrons.

4.3 Time over Threshold

The *Time over Threshold* (ToT) is a widely used method in particle detectors to describe signals. It is composed of two measurements of a signal going above (leading) and returning below (trailing) at a given threshold. The time length between those two measurement is named ToT and provides information about the energy deposited by the interacting particle through the reconstruction of the difference between leading and trailing time.

Similarly as for the Threshold, the ToT tuning (Sec. 3.4.1) contains firstly a global tuning to process. A second local tuning, set the value of the TDAC register (fig. 3.5) independently for each pixel. The following sections describe those two steps and present the results to determine the configuration for a ToT response to a MIP like analog injection that gives the best performances to the FE-I4 chip.

4.3.1 Global ToT tune

The purpose of the ToT tuning is to get a uniform ToT response to the same injected signal for every pixel. For a certain input charge, the ToT can be tuned by changing the preamplifier feedback current (Sec. 3.5). This current controls how fast the signal returns to the baseline.

The purpose of the global ToT tuning is to adjust the 8-bit register `PrmpVbpf` which is common for all pixels. This first tuning will adjust the average value of all pixels to the target at fixed input charge, before operating the fine tuning.

Results

The figure 4.7 shows the result of the global ToT tuning for 7 values of ToT target, expressed in clock cycles[2]. The tuning is done with the configuration determined previously : injected charge of 1.5×10^4 electrons and Threshold of 3,000 electrons.

As seen in the threshold global TDAC tune (Sec. 4.2.1), the value of `PrmpVbpf` is determined by setting the achieved value (y axis) to the x axis by using the corresponding curve. Because the slope is small, the values over ToT=5[3] the target ToT=5 gives `PrmpVbpf=0` : The average value for every pixel ToT response will not mach the target in those cases and a bad performance is expected. On the

[1] A pixel that gives neither signal nor noise is called a dead pixel.

[2] The LHC runs at 40 MHz proton-proton collision. To make measurements that matches the collisions, the clock of the FE-I4 chip is set to the same frequency. In this case, one clock cycle corresponds to 25 ns.

[3] As discussed previously, means 5×25 ns = 125 ns

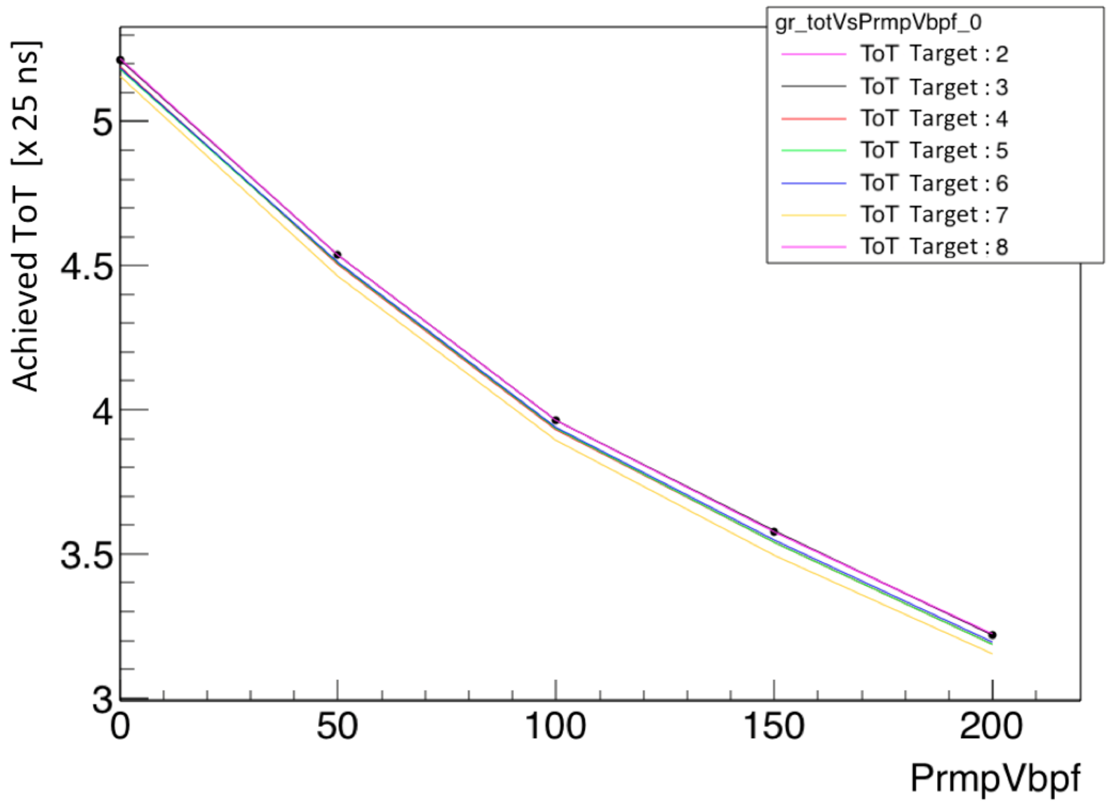

Figure 4.7: `PrmpVbpf` vs Time over Threshold for ToT target from 2 to 8 clock cycles. The five black points are situated at the five points of measure for `PrmpVbpf` = 0, 50, 100, 150 and 200. They are only shown on the curve where ToT target = 2, but the measures were done on those values for all the targets.

other hand, for a tuning for ToT = 2 or 3, the corresponding value for `PrmpVbpf` is approaching 255, the largest value for this 8-bit register. As for large target values, it can have an effect on the tuning performances.

4.3.2 Local TDAC tune

The local TDAC tune is the fine ToT tuning for the FE-I4 chip. It aims to get a uniform response from each pixel to the same input signal. The tuning is used to set the value of a 4-bit register named FDAC which is located in the `PreAmp` of every pixel and controls the feedback current independently. The size of the register being smaller, it is important to set the global `PrmpVbpf` value prior to make the fine tuning.

Results

The local FDAC tuning was done with the same configuration and the same target values as for the global ToT tuning (Sec. 4.3.1). The results for all targets are presented in the figure 4.8.

As discussed previously (Sec. 4.3.1), the target values ToT=6, 7 and 8 give bad performances due to the value `PrmpVbpf` = 0 in each case in the global ToT tuning. On the other hand, the result of global ToT tuning for the target ToT=2 is `PrmpVbpf` = 254, which is near the limit of the slope of the 8-bit register. As shown in figure 4.8, the number of pixels tuned to the right targets is the highest for target ToT = 3, 4 and 5.

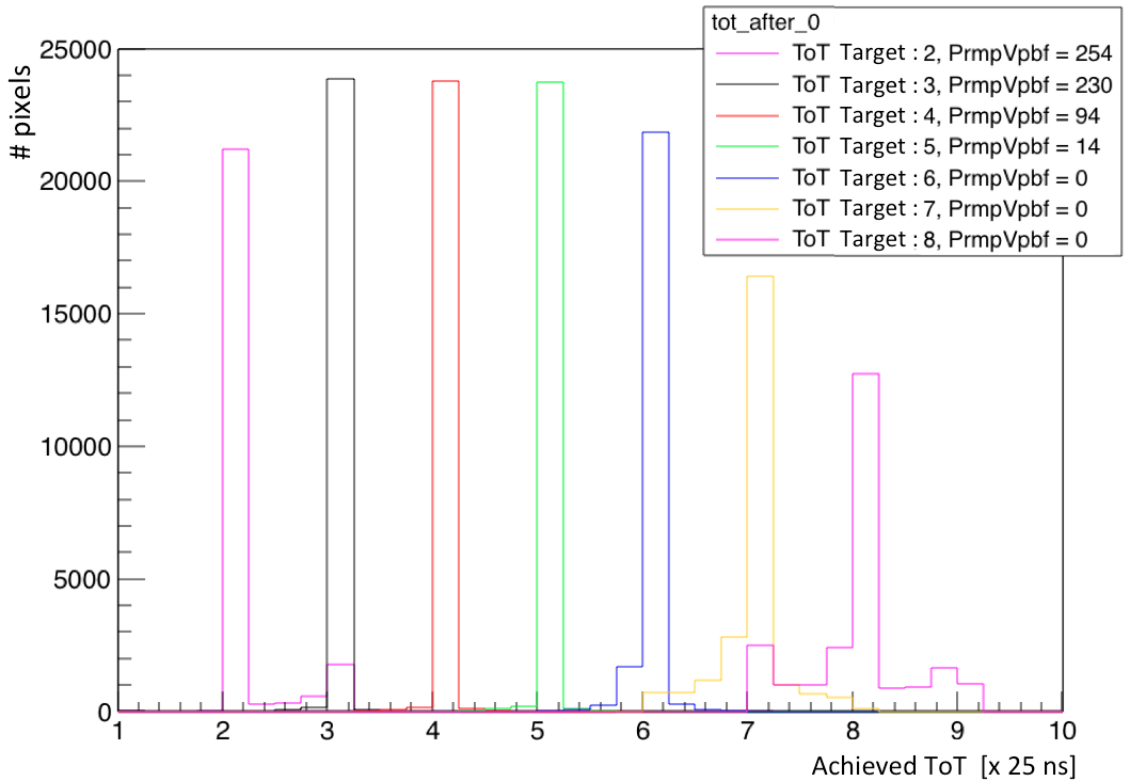

Figure 4.8: Distribution of the achieved Time over Threshold for each pixel **after tuning** for ToT target from 2 to 8 clock cycles. The parameter `PrmpVbpf` for each target is also shown.

4.4 Tuning verification

In the schematics of the pixel in figure 3.5, it is obvious that the amplification of the signal is done prior to the comparison to the threshold. Subsequently, by changing the value of the FDAC register, the ToT tuning is expected to alter the performances of the Threshold tuning : It is necessary to make one more time the Threshold tuning **before** and **after** the ToT tuning. The final comparisons from the threshold tuning performances for ToT = 3, 4 and 5 permits to understand which tuning parameters are the most suitable for operations.

The Table 4.2 shows the results of the verification process with threshold target set to 3000 electrons. The ToT target of 4×25 ns shows a slightly best performances to center the threshold mean value of all pixels to the target. However, the ToT target of 5×25 ns gives a narrower peak. It also corresponds to the combination that gives the minimal noise.

ToT Target (×25 ns)	Mean Threshold (e)	Threshold RMS (e)	Mean Noise (ENC)	Noise RMS
3	2990 ± 0.67	104.7	161.5 ± 0.12	19.2
4	3008 ± 0.71	109.7	147.7 ± 0.12	17.91
5	3010 ± 0.63	97.88	144 ± 0.11	18.25

Table 4.2: Results for the tuning verification for injected charge of 1.5×10^4 e^-, Threshold target 3,000 electrons and ToT target 3, 4 and 5 ×25 ns.

The charge injection of 1.5×10^4 electrons was determined to simulate a minimum ionizing particle through the sensor. Every other hit would then have a greater charge and give a longer ToT output. By setting the ToT to 5 ×25 ns, a better precision on the measurement is also expected because the

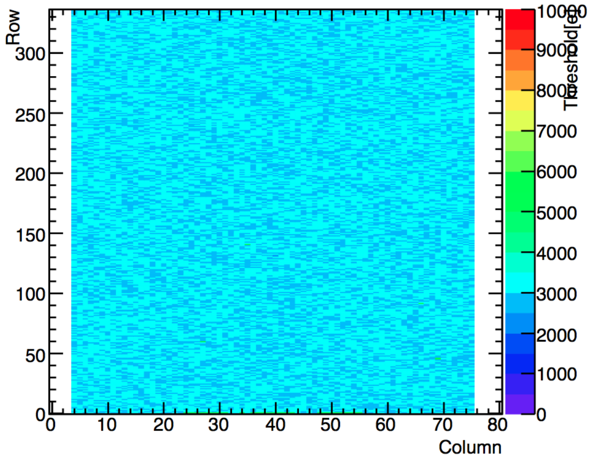

Figure 4.9: Hitmap of the **Threshold distribution** of the pixels of FE-I4 chip. The injected signal is 1.5×10^4 electron, the threshold target 3000 e^- and the ToT target 5 ×25 ns.

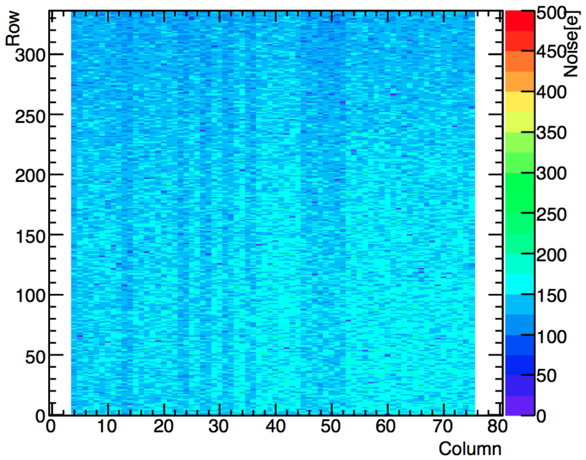

Figure 4.10: Hitmap of the **Noise distribution** of the pixels of FE-I4 chip. Same configuration as for fig. 4.9.

ratio of the ToT to the length of one clock cycle will increase.

As a conclusion, the figure 4.9 shows the value of the threshold for each pixel after tuning. The result shows a uniform distribution with no defective region. The figure 4.10 represents the distribution of the noise within each pixel. This chip being used under testing purposes for several years, vertical patterns appears with higher noise.

Part III

Study of Higgs Boson Pair Production

Chapter 5

Monte Carlo Simulation of Higgs pair production and Backgrounds

This Chapter is an overview of the ATLAS software used for analysis. This software is mostly run using the CERN Linux cluster `LXPLUS` from an ssh session. It can be run online during the data taking or offline to process the data once it is recorded to storage. Data processing and analysis are performed with a framework called `ATHENA`. The framework has a skeleton into which developers plug in their code, providing most of the common functionality and communications between different components.

The Section 5.1 presents the simulation chain for Monte Carlo (MC) event production. The Section 5.2 concerns the event selection through three levels of cuts applied on the events. The modeling of Higgs pair production and the backgrounds are discussed in Section 5.3. Finally, the Section 5.4 shows an event display of Higgs pair production in the ATLAS detector.

5.1 Monte Carlo Production

In order to study the detector response for a wide range of physics processes and scenarios, a detailed simulation has been implemented that carries events from the event generation to output in a format which is identical to that of the real detector. As shown in figure 5.1, the simulated data used for this study uses four steps [42] :

- **Event Generation** : The MC generators simulate events of proton-proton collisions. These events can be filtered at the generation step so that only events with a certain property are kept. The result is a list of initial, intermediate and final state particles and their energy-momentum four-vectors. The simulation includes heavy particles and their decay to lighter particles as measured in the detector. The output of the event generation is *EVNT files*.

- **Simulation** : The ATLAS detector response to the generated events is simulated. The program computes the interaction of the particles with the detector to create a realistic response. Cuts can be applied to select only certain particles to process in the simulation. Each particle is propagated through the full ATLAS detector by `Geant4` [43]. The configuration of the detector, including misalignments and distortions, can be set by the user. The energies deposited in the sensitive portions of the detector are recorded as "hits", containing the total energy deposition, position, and time, and are written to a simulation output file, called *HITS files*.

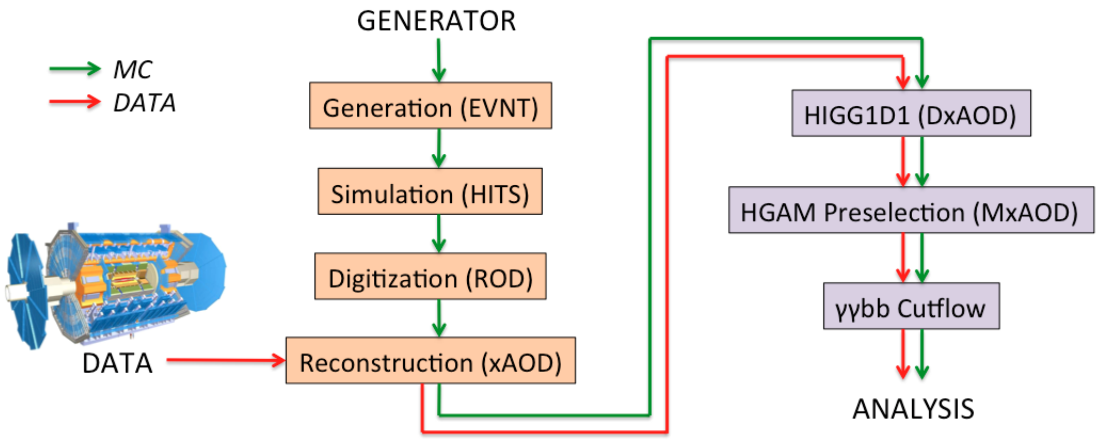

Figure 5.1: Simplified schematic of the ATLAS software from generation to $\gamma\gamma b\bar{b}$ analysis. The green (Red) arrows show the path of MC (DATA). The orange squares show the main steps for common analysis (see text) and the objet format in the brackets. The purple boxes represent the derivation process for a specific event selection, used for the current analysis.

- **Digitalization** : The simulated energy deposit is converted into bit information. The simulated data become then the same format than the real data created by the ATLAS detector. The digitization takes the hits output from simulated events. The overlay (pile-up) is done in the digitization. At this stage, detector noise is added to the event. The output of the digitization step is a *Raw Data Object (RDO)* file, which is in exactly the same format as the real data.
- **Reconstruction** : The simulated and real data are derived through the same trigger and reconstruction packages. Each signal is associated to objects for analysis (electrons, muons, jets, etc.). Reconstruction task is to recognize local pattern, to reconstruct the tracks, vertices and clusters in the different sub-detectors, and finally to create high level objects, such as particles of different identification, jets including their flavor tag, or missing transverse energy. These high level reconstruction objects are the input to the analysis. The output format is called *Analysis Object Data (xAOD)* which is the starting point for many physics analyze.

5.2 Event selection

The simulation is processed for signal Higgs pair production and the corresponding background events. The events are selected within the $hh \to \gamma\gamma b\bar{b}$ channel. The method uses one Higgs boson that decays to a mode (or channel) with a pair with a large branching ratio for the Higgs boson tagging. As discussed in Section 2.1.3, the branching ratio of the decay $h \to b\bar{b}$ is 57%. The other Higgs boson of a pair of Higgs bosons is then required to decay in a photon pair. The branching ratio for that channel is only 0.2% but it provides a clean mass reconstruction with a high signal-to-noise ratio. The $\gamma\gamma b\bar{b}$ channel is then an excellent final state for a search for Higgs boson pair production [44] thanks to the large $h \to b\bar{b}$ branching ratio, clean di-photon trigger, excellent di-photon invariant mass resolution and high signal-to-background ratio.

The event selection is made in three steps as in figure 5.1, applied on the simulated events. First, after the reconstruction step, the events are skimmed using the `HIGG1D1` derivation (Sec. 5.2.2), applied on every event to keep at least one Higgs boson candidate identified. The second step (Sec.

5.2.2) is a preselection focused on the events that contains the $h \to \gamma\gamma$ process [45, 18]. The output is called MxAOD (*for Mini-xAOD*). The final step is a selection that includes b-tagging[1] to identify the $h \to b\bar{b}$ process which is combined to the preselection to identify Higgs boson pair (Sec. 5.2.3). This selection is based on jet p_T cuts and b-tagging is applied to specify the $\gamma\gamma b\bar{b}$ channel.

5.2.1 HIGG1D1 Skimming

The first step, as shown in the top purple box of figure 5.1, concerns the identification of Higgs events. A set of cuts listed below is applied in order to keep the events that contains at least one Higgs boson. The `HIGG1D1` skimming keeps the events with the following requirements :

- **Photons** : the photons are required to pass :
  - Loose : Three set of cuts : **loose**, **medium** and **tight**, have less or more requirements on particle identification. This provides flexibility in analysis, for example to improve the signal efficiency for rare processes which are not subject to large backgrounds from fakes. The **loose** set of cuts performs a simple identification based only on limited information from the calorimeters. This set of cuts provides excellent identification efficiency, but low background rejection. It was chosen due to the few number of Higgs pair production events.
  - $p_T > 20$ GeV : a minimum of 20 GeV is required in order to keep a good object quality.
  - $|\eta| < 2.47$: within the range of the inner detector and electromagnetic calorimeter.
  - Remove crack region between barrel and endcaps $|\eta| = 1.37$ to 1.52 that gives lower performances on track reconstruction
- **Electrons** : every electrons that verify :
  - Loose
  - $p_T > 20$ GeV
  - $|\eta| < 2.47$: within the range of the inner detector and electromagnetic calorimeter.
  - Remove the crack region $|\eta| = 1.37$ to 1.52 between barrel and endcaps
- **Muons** : the requirements on muons are :
  - $p_T > 20$ GeV
  - $|\eta| < 2.7$: within the range of the muon detector.
- **Keep events** with $\gamma\gamma$, ee, $e\mu$ and $\mu\gamma$

The DxAOD output is used as input in the next derivation step.

[1] Identification of jets originating from b quarks.

5.2.2 $h \rightarrow \gamma\gamma$ preselection

The $\gamma\gamma b\bar{b}$ Analysis framework depends mainly on the $h \rightarrow \gamma\gamma$ event selection which runs when MxAOD is produced (Fig. 5.1) :

- **Jets** : all jets which pass :
  - $p_T > 25$ GeV : A minimum of 25 GeV is required in order to keep a good object quality.
  - $|\eta| < 4.4$: within the range of the inner detector and electromagnetic and hadronic calorimeters.
  - Jet Vertex Tagger (JVT) > 0.59 : The tracking information is used to compute a variable called Jet Vertex Fraction, which is the fraction of the total momentum of track in the jet which are associated with the primary vertex. By imposing a lower limit on this variable, it is possible to reject the majority of pile-up jets, due to the large difference between their momentum and the momentum of the leading jet. This process leads to a jet efficiency from hard-scattering that depends on the number of reconstructed primary vertices (N_{PV}) in the selected event. The JVT is a multivariate combination of two track-based variables where the hard-scatter jet efficiency is stable as a function of N_{PV}.
- **Photons** : at least two good photons which :
  - Are away from bad calorimeter region : $|\eta| = 1.37$ to 1.52
  - Pass electron ambiguity cut : converted photons, characterized by the presence of at least one track matching an electromagnetic cluster with an inner track, can be identified as electrons in the detector.
  - $p_T > 25$ GeV
  - $|\eta| < 2.47$

MxAOD CUTS

MxAOD are produced by the group with the $h \rightarrow \gamma\gamma$ selection applied. The skimming is done after `HIGG1D1` (fig. 5.1) and the selection is described above. It makes cuts on events to require at least two photons that correspond to a $h \rightarrow \gamma\gamma$ event. The cuts are applied in the following order. The algorithm also provides information on the number of events produced and remaining in the previous event selection steps.

1 N_{events} : The number of events in the reconstruction output (xAOD)

2 N_{DxAOD} : The number of events in the `HIGG1D1` output.

3 **All events** : The number of events in the MxAOD input. It may differ from N_{DxAOD} in the case where the number of events is normalized to the luminosity.

4 **No duplicates** : Suppresses the duplicates events.

5 **Pass trigger** : The High Level Trigger is send from the detection one photon with a transverse momentum over 100 GeV.

6 **GRL (Good Run List)** : Formed by applying Detector Data Quality criteria, to the list of all valid physics runs and luminosity blocks.

7 **Detector DQ (Data Quality)** : Must satisfy a good efficiency

8 **Has PV (Primary Vertex)** : Each bunch crossing of the LHC produces an average of 50 collisions. This cut verifies if the measured particles are coming from the same primary vertex.

9 **2 loose photons** : At least two photons.

10 e/γ **ambiguity** : Electron and photon clusters may be reconstructed both with electron and photon hypotheses to maximize the reconstruction efficiency for both.

11 **Trigger Match** : Verifies if the trigger corresponds to the event in time.

12 **Tight ID** : Second level (following Sec.) of identification for one of the two photons.

13 **Isolation** : Confirm the isolation of the photons for an accurate mass reconstruction. The isolation is defined from the distance ΔR between the two photons with $\Delta R = \sqrt{\Delta\theta^2 + \Delta\phi^2} > 0.4$.

14 **Relative p$_T$ cuts** : Computed from the ratio of the photon transverse momentum to the mass of the di-photon system. $p^T_{\gamma_1}/M_{\gamma\gamma} \geq 0.35$ and $p^T_{\gamma_2}/M_{\gamma\gamma} \geq 0.25$, where γ_1 has the greater momentum in the $\gamma_1\gamma_2$ pair of identified photons.

15 **105** $< m_{\gamma\gamma} <$ 160 GeV : a window around the mass of the Higgs boson.

Event weight

The MxAOD derivation provides also an event weighting algorithm. The size of a MC sample is determined by the generation of a certain number of events N_{events}, while the cross-section σ of the sample is a fixed quantity depending on the process. Since the number of events, sample size, and luminosity $\mathscr{L}$ are related according to $\sigma = N_{events}/\mathscr{L}$, the luminosity of a MC sample varies according to the number of events generated and the cross-section of the process. It is necessary to weight the MC sample corresponding to the luminosity. The weight is computed using the following equation :

$$W = \frac{\sigma\mathscr{L}}{N_{events}}. \tag{5.1}$$

Histograms are weighted by multiplying the quantity used to fill the histogram by the event weight.

5.2.3 $\gamma\gamma b\bar{b}$ Cutflow

Once the $h \to \gamma\gamma$ preselection is validated, the last selection specifies the identification of the four particles $\gamma\gamma b\bar{b}$ within the requirements. The identification of b-quarks uses the *anti-k_t jet clustering algorithm* [46] to combine the calorimetry and tracking information to define jets. The outputs of the b-tagging algorithms are combined in a *Multivariate Discriminant* (MV2) which provides the best separation among the different flavour hypotheses.

b-tagging algorithm

The b-tagging is a jet flavor tagging method used for the identification (or "tagging") of jets originating from bottom quark. The selection on the b-tagging depends on the number N_{b-jet} of jets that pass the selection algorithm `MV2c10_FixedCutBEff`, where `MV2c10` describes the degree of charm quark rejection in the MV2 discrimination method and `FixedCutBEff` identifies jets as b-jets if the identification efficiency is over a preselected percentage. Each event is categorized in function of the number of jets tagged as b-jets under different tagging efficiencies :

- **If** $N_{b-jet} > 2$ **at 85% of efficiency :** The event is rejected to avoid overlaps with the $hh \to b\bar{b}b\bar{b}$ analysis. In the global two Higgs boson analysis, four different processes are merged to optimize the number of Higgs pair observation. The selection cuts are set to avoid overlaps that result in duplicated events.
- **If** $N_{b-jet} = 2$ **at 85% of efficiency :** The event belongs to a **2-tag signal event**.
- **If** $N_{b-jet} = 1$ **at 60% of efficiency :** Then, the event is a **1-tag signal candidate**. In this case further categorization is needed, typically the heaviest non-b-tagged jet reconstructed mass is considered as a b-jet to complete the pair.
- **If** $N_{b-jet} = 0$ **at 60% of efficiency :** The event belongs to the **0-tag control region**.

Di-photon mass cuts

The final requirement is made so that events should fall into a narrow window around the Higgs mass: $120.3 < m_{yy} < 129.7$ GeV. Events falling outside this window but inside a loose window of $105 < m_{yy} < 160$ GeV are retained to enable the di-photon background to be estimated.

5.3 Signal and Background modeling

The treatment of data in counting experiments contains two independent processes, both contributing additively to the total number of counted events. There are labelled as "signal" and "background". The observed total number of events should correspond to the addition of the well known background contribution, and the signal that depends on the theoretical model.

5.3.1 Signal

The non-resonant Higgs pair production by Higgs self coupling as well as heavy Higgs production are implemented in the `MADGRAPH 5` [47] at Leading Order (LO). This model is run and the decay to a pair of Higgs is done with `Pythia 8` [48]. The decays of each Higgs boson is forced to become a pair of photons or a pair of b-quarks.

The production of a heavy scalar (H) decaying to two Higgs bosons (hh) is used in this study. The samples are generated with a natural width of the heavy scalar of 10 GeV, at masses of 250, 325, 350 and 400 GeV. The heavy scalar is forced to decay to two light SM Higgs bosons with $m_h = 125$ GeV. The decay of the two SM Higgs bosons is handled by `Pythia 8` to force the decay to a pair of photons and a pair of b-quarks.

5.3.2 Background

The dominant continuum backgrounds are QCD $\gamma\gamma$ + jets and γ + jets as shown in figure 5.2. Under some conditions, the photons can be identified as Higgs boson if they match the requirements of the `HIGG1D1` selection. The pair of b-quark produced in QCD processes could also become a candidate for the $hh \to b\bar{b}b\bar{b}$ analysis. Therefore, the results of Section 6.3 shows a decreasing number of background event number as the number of identified b-jets increases.

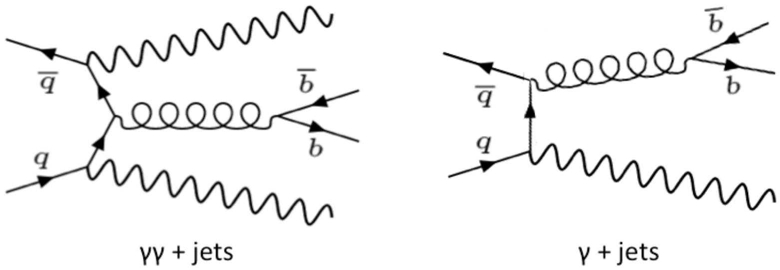

Figure 5.2: Feynman diagrams of the lowest order main backgrounds for the Higgs boson pair search in the $\gamma\gamma b\bar{b}$ channel

For the $\gamma\gamma$ + jets background, a collection of 15 samples corresponding to 15 mass windows of the di-photon system $m_{\gamma\gamma}$ is produced with `Pythia 8`. The main motivation to split the sample into windows is to produce an accurate number of events corresponding to each cross section. The γ + jets sample is a collection of 14 windows over the transverse momentum of the photon $P_{T\gamma}$.

The list of Signal and Background samples used for the analysis is detailed in the Appendix B.

5.4 Event display

The analysis framework provides a function to display the events. The function was run over an MxAOD sample so it passed all the requirements over `HIGG1D1` and MxAOD derivation cuts.

The figures 5.3, 5.4 and 5.5 shows the same event from three representations in the laboratory frame. In this event, six jets are reconstructed while two are b-tagged with an efficiency over 85%. Those two b-tagged jets have a reconstructed mass of 128.9 GeV for the most energetic one and 68.9 GeV for the second. As seen in Section 5.2.3, this event belongs to the **2-tag signal event** and passes the **high mass selection**. All requirements are validated except for the mass of the di-photon system $m_{\gamma\gamma}$ = 785.8 GeV which is far beyond the di-photon mass cut selection. This event will be rejected for the analysis.

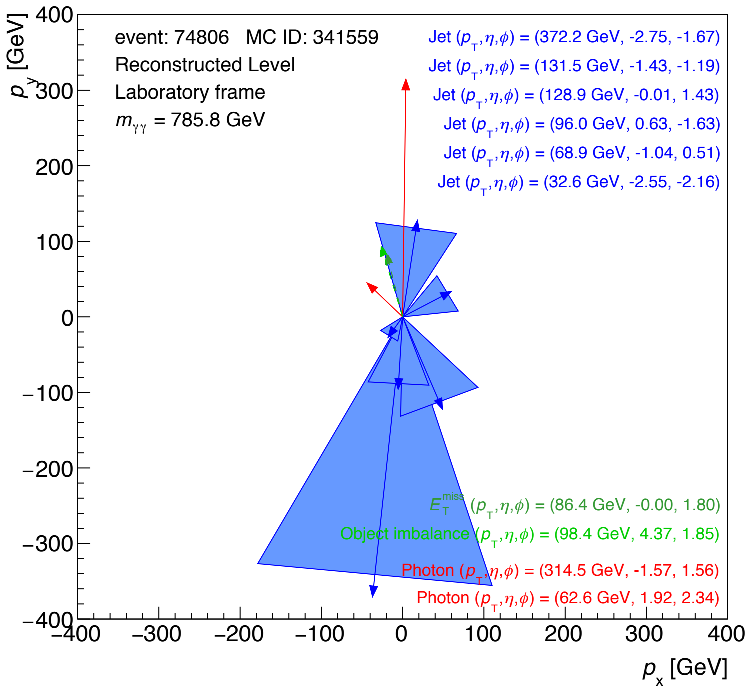

Figure 5.3: $\gamma\gamma b\bar{b}$ event display of in the momentum space over the x and y axis of the ATLAS detector (transverse to the beam axis)

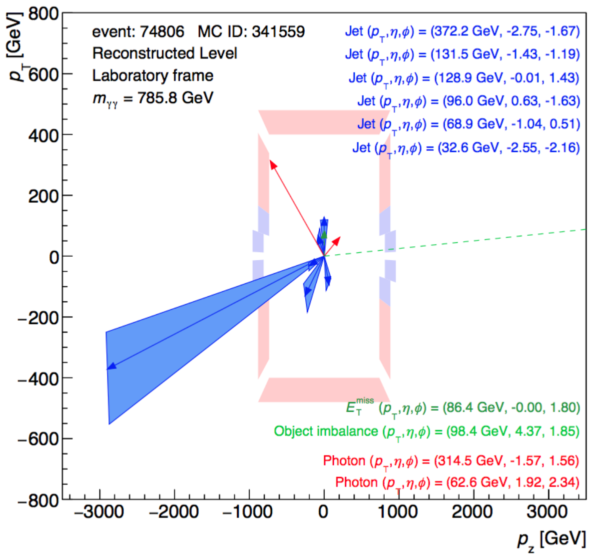

Figure 5.4: $\gamma\gamma b\bar{b}$ event display of in the momentum space over the z axis (along the beam axis) and the transverse momentum p_T

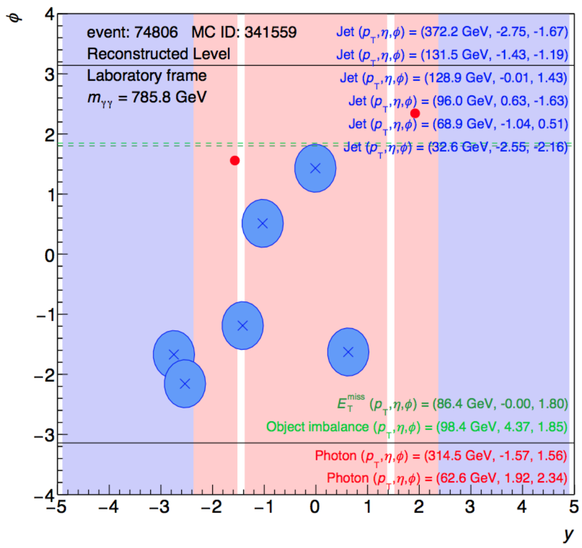

Figure 5.5: Event display of $\gamma\gamma b\bar{b}$ positions in cylindrical coordinates

Chapter 6

Prospects of the $hh \to \gamma\gamma b\bar{b}$ channel at the end of Run 2

This Chapter presents the results for the prospects of the Higgs self-coupling measurement at the end of LHC Run 2. The Section 6.1 describes the simulated samples production. To allow a good accordance between the previous and future analyze, the reproducibility of event simulation is required. The method described is used to produce samples for future analysis with higher luminosities, center-of-mass energy or even new background processes for analysis involving higher orders. The Section 6.2 presents the results on the expected number of events for the non-resonant Higgs self-coupling and resonant heavy Higgs production processes by comparison with the corresponding backgrounds.

6.1 Production of MC datasets

The first task in this analysis work is to make the simulation of signal and background events. As discussed in Section 5.3, the signal is determined to be either *non-resonant Higgs self-coupling* or *resonant MSSM heavy Higgs production.* As discussed also, the main background is QCD $\gamma\gamma$ + jets and γ + jets. The single Higgs production could also be considered as a background but the cross-section being very small, it should be added in the *Next to Leading Order* (NLO) analysis. The LO terms being the terms with the largest order of magnitude, the NLO is a correction that includes smaller terms of the model.

Signal and background simulated events were produced for the analysis of Higgs pair production in Run 1 and early Run 2 (Sec. 2.3). As the luminosity growing, new samples are required corresponding to the energy of 13 TeV as in Run 2. However, it is necessary for reproducibility to get an accordance between Run 1 and Run 2 samples. The method described here presents the reproduction of the method used for the early Run 2 analysis. The production of future samples will differ mainly by the center of mass energy and detector geometry while most of the production parameters through the full simulation (described in Sec. 5.1) will use a similar method.

6.1.1 Generation to DxAOD production

The following sample was used in the early Run 2 analysis :

- `mc15_13TeV.341559.MadGraphPythia8EvtGen_A14NNPDF23LO_sm_hh_yybb.merge.DAOD_HIGG1D1.`

```
e4038_s2608_s2183_r7772_r7676_p2669
```

This is a sample of *MC DxAOD Higgs self-coupling* to $\gamma\gamma b\bar{b}$. The energy at the center of mass in the proton-proton system is 13 TeV and the data set identifier (run number) is 341559. The generators used are `MADGRAPH 5`, `Pythia 8` and `EvtGen` while the parton distribution function is `A14NNPDF23LO`[1] at leading order. The AMI tags `e4038`, `s2608`, `s2183`, `r7772`, `r7676` and `p2669` contain the information for production commands[2]. The Appendix A describes in detail the production process and the Appendix B contains a list of all the MC datasets used in this analysis. The `HIGG1D1` derivation was also applied to this sample with the cuts as discussed previously (Sec. 5.2.2).

Firstly, the `ATHENA` commands were reproduced with a small number of events. This is to avoid long waiting time between the beginning of the compilation and an eventual error. All the commands can be found in Appendix A. After the 5 events was successfully created, a larger number of 100 events were generated and were derivated using the same commands.

6.1.2 MxAOD preselection and $\gamma\gamma b\bar{b}$ cut flow

As seen in Section 5.2.2, MxAODs are used as preselection cuts in the present analysis. MxAOD is the common format for all analyze that contains $h \rightarrow \gamma\gamma$ process. Both official and private DxAOD samples were derived to MxAOD for comparison. The results are presented here.

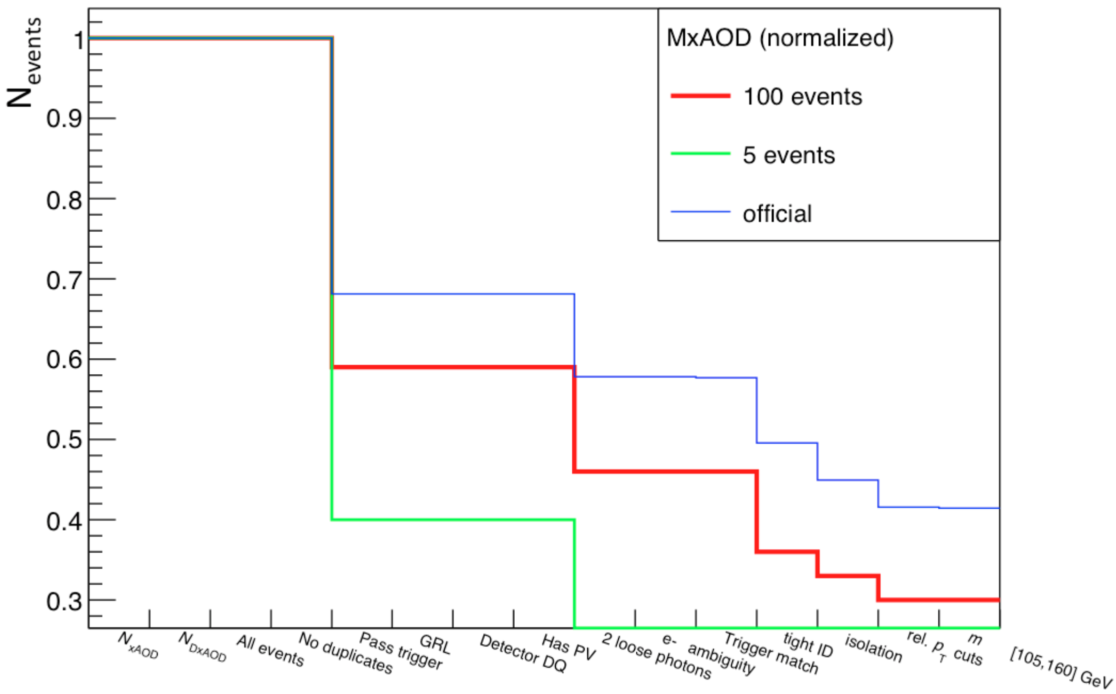

Figure 6.1: A normalized number of events remaining after each cut. The MxAOD preselection is applied for 5 events sample (Green), 100 events sample (Red) and $\gamma\gamma b\bar{b}$ official sample (Blue, 10000 events) of Higgs boson pair production simulation. The histograms are normalized to show the fraction of events that remains after several cuts.

The figure 6.1 shows the cut-flow along the MxAOD derivation. All cuts that appear in this figure are the steps described in section 5.2.2. The cuts are applied one by one from the left to the right

[1] See `https://nnpdf.hepforge.org/` for more information
[2] More information on `https://ami.in2p3.fr/`

as the number of remaining events is decreasing. On the figure, two privates samples of 5 and 100 events plus one official sample containing 10,000 events are compared, normalized to the proportion of events remaining along the cut-flow.

Some cuts have no effects on the MC samples. Because those events are simulated, they all contains the process of *Higgs pair production*. The figure 6.1 shows, as it should be, that no cut occurred between reconstruction and `HIGG1D1` derivation as $N_{xAOD} = N_{DxAOD}$. There is also no duplicates as expected. Furthermore, the Good Run List (GRL) as well as Detector DQ are informations about data taking and gives no effects on MC sample cuts. The next cut that gives no effect is the confirmation of the existence of a Primary Vertex (PV). The MC production assures the Higgs pair to come out from the same proton-proton collision and the fact that no effects are observed for this cut is a confirmation that the reconstruction is done properly. Finally, there is no ambiguity between photons and electrons at the reconstruction level in MC samples so no cuts are observed.

On the other hand, the cuts that alter most of the number of events in the current samples are the following. First, the most important cut on the events is the High Level Trigger that requires a transverse momentum of one photon to be greater than 100 GeV. To assure this requirement, the original Higgs boson that decayed into a pair of photons should be boosted to assure the triggering. Secondly, the requirement for two loose photons and one photon tight ID is the other important cut due to the importance of a clear identification of the objects.

From figure 6.1, it is obvious that the sample containing 5 events is too small as the cuts exclude quickly every events in the sample. After increasing the number of events to 100, the cut efficiency is found to be 30%, while it is more than 46% for the official sample. As discussed previously in section 5.2.2, the number of events N_{events} is related to the luminosity $\mathscr{L}$ and the cross section $\sigma = N_{events}/\mathscr{L}$. The cross section being fixed for one defined process (i.e. Higgs self-coupling), the number of events determines the luminosity. Therefore, the events have to be weighted using the equation 5.1.

The figures 6.2, 6.3 and 6.4 show a comparison between the private and official samples at the output of the $\gamma\gamma b\bar{b}$ cut-flow (Sec. 5.2.3). The three histograms show respectively the control regions with **zero** or **one** b-tagging and the signal region containing exclusively events with **two** b-tag jets. The number of events in the input is normalized to the luminosity expected at the end of Run 2 : $\mathscr{L}_{int} = 100\ \text{fb}^{-1}$. The MxAOD used to produce those samples contains the event weighting, providing a better match. The error bars are computed from statistical error coming from the limited number of events, a smaller number of events increases the statistical error. The reweighed 5 events sample is not shown along the cut-flow as the error is too large.

The 100 event sample uncertainty is also large. Therefore, producing a sample that contains more events would decrease the uncertainty. Nevertheless, the proportion of remaining events after the reweighing is in good accordance with the official sample.

The idea in this work was to reproduce the method for event simulation as a starting point to produce Run 2 samples. However, official $\gamma\gamma b\bar{b}$ samples for Run 2 were produced during the present work was ongoing. The analysis that follows used those official samples that already contain a large number of events. However, as the luminosity and collision energy growing, new samples are often required. The work is the starting point to produce new samples corresponding to smaller cross-

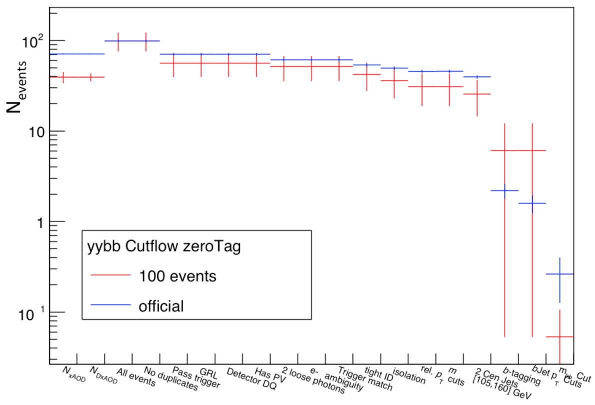

Figure 6.2: $\gamma\gamma b\bar{b}$ cutflow in the **zero tag control region** for 100 events private sample and 10000 events official sample. The number of events is normalized to the LHC Run2 expected luminosity.

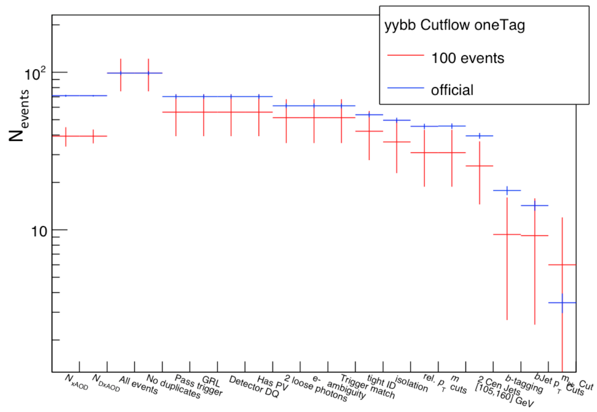

Figure 6.3: $\gamma\gamma b\bar{b}$ cutflow in the **one tag control region** for 100 events private sample and 10000 events official sample. The number of events is normalized to the LHC Run2 expected luminosity.

section process and backgrounds or higher order simulation.

6.2 $hh \to \gamma\gamma b\bar{b}$ signal and background prospects at the end of Run 2

As the luminosity is growing, it becomes possible to probe phenomena that are very rare, i.e. whose cross-sections are very small. Since the discovery of the Higgs boson in 2012, the next step requires a higher luminosity and a detector that gives the best performance. The idea here is to give a qualitative analysis on the expectation at the end of the current run (Run 2). It is a demonstration that proves the necessity to increase the luminosity to probe the phenomena of (non-resonant) Higgs self-coupling and (resonant) heavy Higgs production that were presented in the Chapter 2.

6.2.1 Signal and background simulation

The goal of the work presented in this Section is to determine the expected number of signal and background events that will be measured at the end of the Run 2. As discussed in Section 5.3, the signal and the backgrounds are both simulated. The samples were produced by the method described previously (Sec. 6.1) and each event is required to pass all the cuts presented in the Chapter 5 of all derivation steps (`HIGG1D1`, MxAOD and $\gamma\gamma b\bar{b}$ cut-flow). The table 6.1 shows all the samples that were used in this analysis with the corresponding production cross-section times branching ratio, the number of events simulated and the number of events that are expected to be produced with an integrated luminosity of $\mathscr{L}_{int} = 100$ fb^{-1}, as expected at the end of Run 2. The computation for the last is made from the following relation :

$$\sigma = \frac{N_{events}}{\mathscr{L}_{int}}, \tag{6.1}$$

between the cross section σ, the number of events N_{events} and the integrated luminosity $\mathscr{L}_{int}$.

The samples used in this analysis, signal and backgrounds were produced independently with the following characteristics :

- **Signal** : There are two kinds of signals, resonant and non-resonant, depending on the phenomena of the interest. The non-resonant model is based on the prediction from the theory

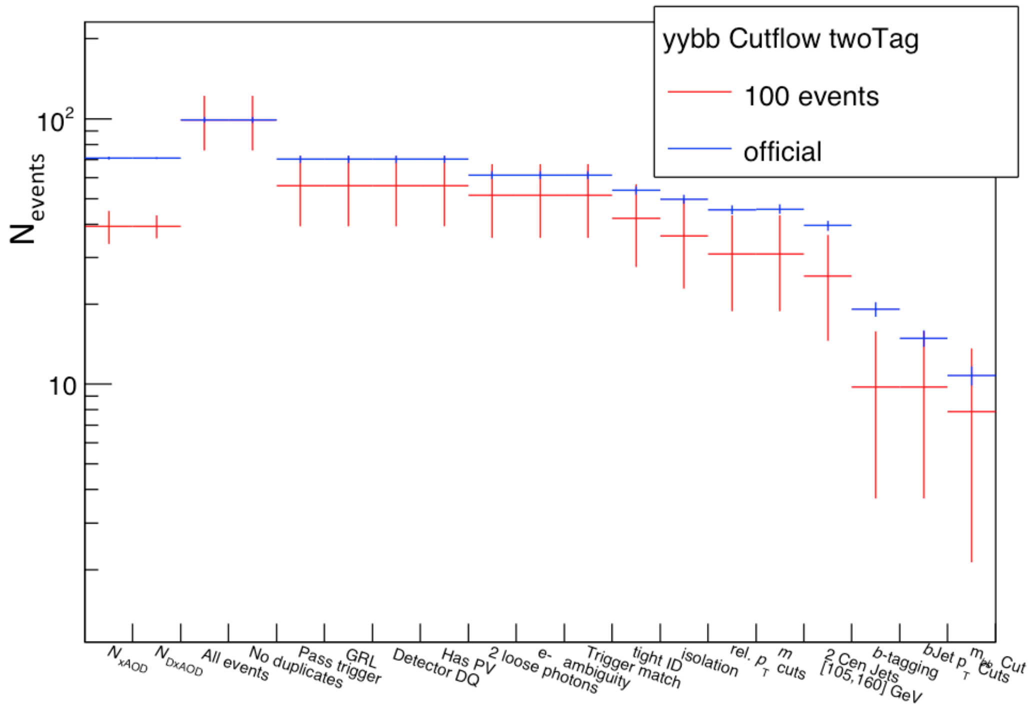

Figure 6.4: $\gamma\gamma b\bar{b}$ cutflow in the **two tags signal region** for 100 events private sample and 10000 events official sample. The number of events is normalized to the LHC Run2 expected luminosity.

of SM Higgs self-coupling, detailed in Chapter 2. The associated cross-section is expected to be 9.89×10^{-5} pb. Concerning the resonant model (also detailed in Chap 2), as it concerns a particle (heavy Higgs) that has never been observed, four samples were produced with different masses (m_X = 250, 325, 350 and 400 GeV) depending on the choice for the free parameters involved. The production cross-section of 0.1 pb is an assumption and has to be measured by the observation of a large number of heavy Higgs production events.

- **Backgrounds** : The backgrounds taken into consideration concern two phenomena that result in $\gamma\gamma b\bar{b}$ events. Firstly, the QCD $\gamma\gamma$ + jets is simulated in 15 samples (Table 6.1), that correspond to 15 windows on the reconstructed mass $m_{\gamma\gamma}$ of the di-photon system. The creation process for each window involving different production cross-section, the background modeling becomes more accurate by processing this way. The other background is the QCD γ + jets. For the same reason, the simulation is made on 14 windows over the transverse momentum p_T of the photon. The background concerning single Higgs production involves very small cross-section, and is almost invisible in the $\gamma\gamma b\bar{b}$ channel. This contribution has not been taken into consideration in this study. However, it would be interesting to introduce this process in a NLO modeling.

The following results show the output of derivation and cut-flow analysis of those samples. The background is presented and then the full results including all signal and background samples are discussed.

6.2.2 QCD $\gamma\gamma$+jets background

As discussed in the previous section, the background is estimated from the association of windows over the di-photon mass and the photon transverse momentum. The estimations for the background are presented here.

The figure 6.5 presents the result for the estimation of the contribution of each $\gamma\gamma$+jets background window with the expected luminosity of the end of Run 2 and a center of mass energy for the proton-proton collision at 13 TeV. The results concern three regions depending on the number of jets (Sec. 5.2.3) that were identified as b-jets. The number of events is normalized to the cross-section (eq. 6.1). The statistical uncertainty is related to the number of events simulated that passed all the cuts up to the $\gamma\gamma b\bar{b}$ cutflow output.

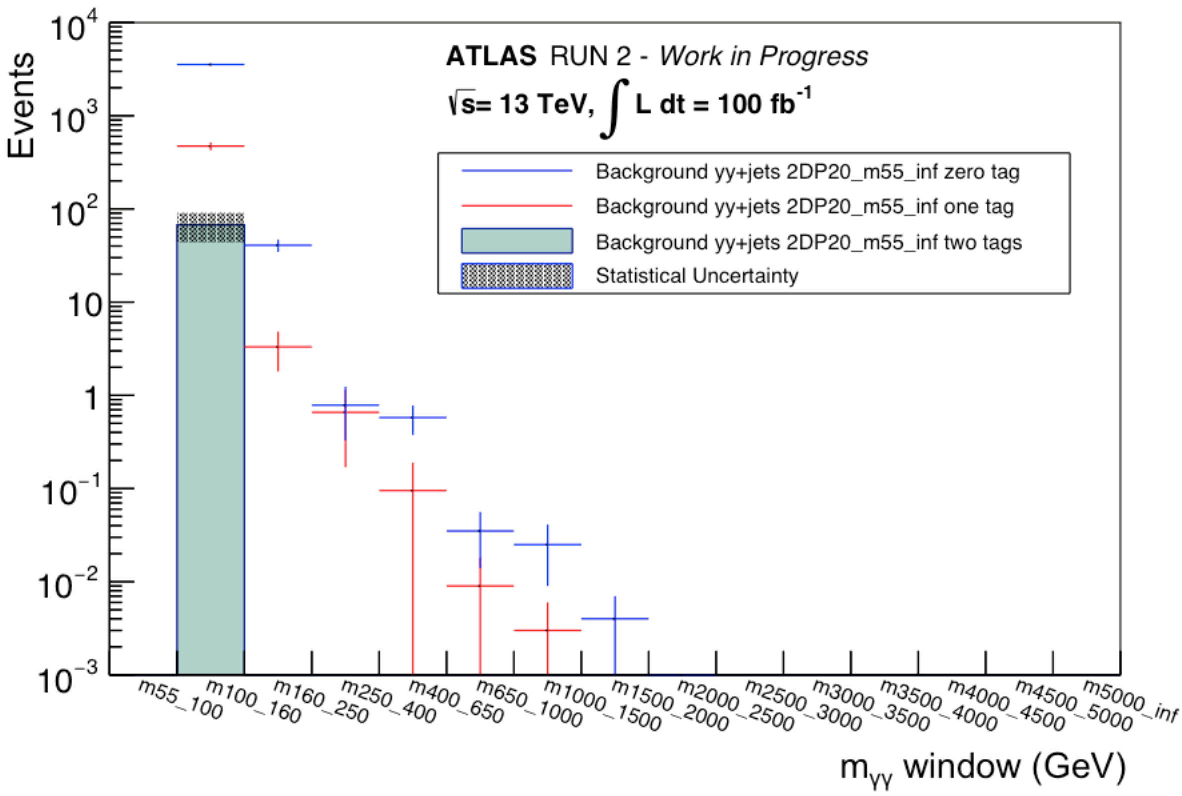

Figure 6.5: Estimation of the $\gamma\gamma$ + jets background for different di-photon mass windows. The results are presented for two control regions with zero, one b-tagging and one signal region involving two b-tagged events.

Within the windows around the mass of the Higgs Boson $m_h = 125$ GeV, a large number of 3546.4 ± 118.9 events are expected in the zero tag category. In the one tag category, the expected number of background events decrease to 471.9 ± 46.4. In the signal region, a smaller number of 67.4 ± 23.6 events are predicted. The requirement on the b-tagging works properly as it makes decrease the background in the signal region.

6.2.3 QCD γ+jets background

The results for the estimation of the number of γ+jets background are presented in figure 6.6 for each b-tagging category and every window on the photon transverse momentum. Those samples also correspond to the expected luminosity of $\mathscr{L}_{int} = 100$ fb^{-1} and a proton-proton center of mass energy of 13 TeV.

The table 6.1 shows the number of events produced and the number of events expected from the equation 6.1 for every windows. The number of events that are expected is very large compared to the number of events produced. In fact, a very large number of γ+jets xAOD events was produced as the production cross-section is very large compared to Higgs pair production cross-section. However, the proportion of events that passed the requirements of HIGG1D1 derivation is very low as those events do not contains any Higgs bosons : this is coming from a misidentification in the algorithm. Moreover, the MxAOD and $\gamma\gamma b\bar{b}$ cutflows makes also strict cuts on the HIGG1D1 output decreasing significantly the number of background events. As in table 6.1, more than 10^{11} events are expected for $17 < p_T < 35$ GeV photon transverse momentum window with the corresponding luminosity of $\mathscr{L}_{int} = 100$ fb^{-1}.

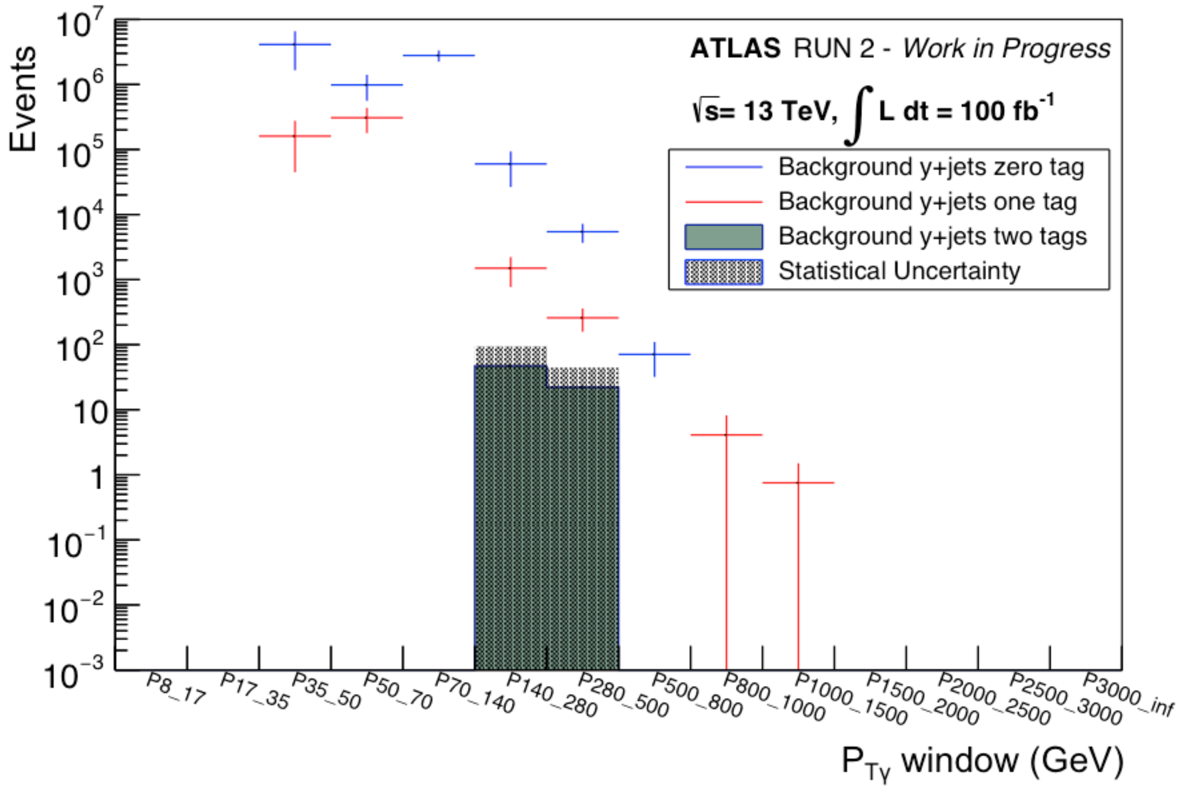

Figure 6.6: Estimation of the γ + jets background for different photon transverse momentum windows. The results are presented for two control regions with zero, one b-tagging and one signal region involving two b-tagged events.

The uncertainty observed in the two tagged control region covers entirely the signal. This is the result of the large ratio between the input and output number of events through the derivation work.

6.3 Results

This section presents the results of signal samples by comparison with the merged background. In the following, the background correspond to the sum of all windows for each category. The systematic uncertainties of the merged events s_f are computed using the propagation of uncertainty formula under addition :

$$s_f = \sqrt{\sum_{i=1}^{N_w} \left(\frac{\partial f}{\partial x_i}\right)^2 {s_x}_i^2}, \tag{6.2}$$

where N_w is the total number of windows[3] and ${s_x}_i$ the uncertainty on the number of events expected in the window i. The derivative $\partial f / \partial x_i$ expresses the weight of the window which is assumed to be equal with each other. This ratio is then considered to be 1. The following results are presented independently for each b-tagging category as explained in section 5.2.3.

6.3.1 0 b-tag category

The results in the 0 b-tag category for signal and merged background modeling are presented in the figure 6.7. The statistical uncertainty is also shown, and was computed using equation 6.2 for the background.

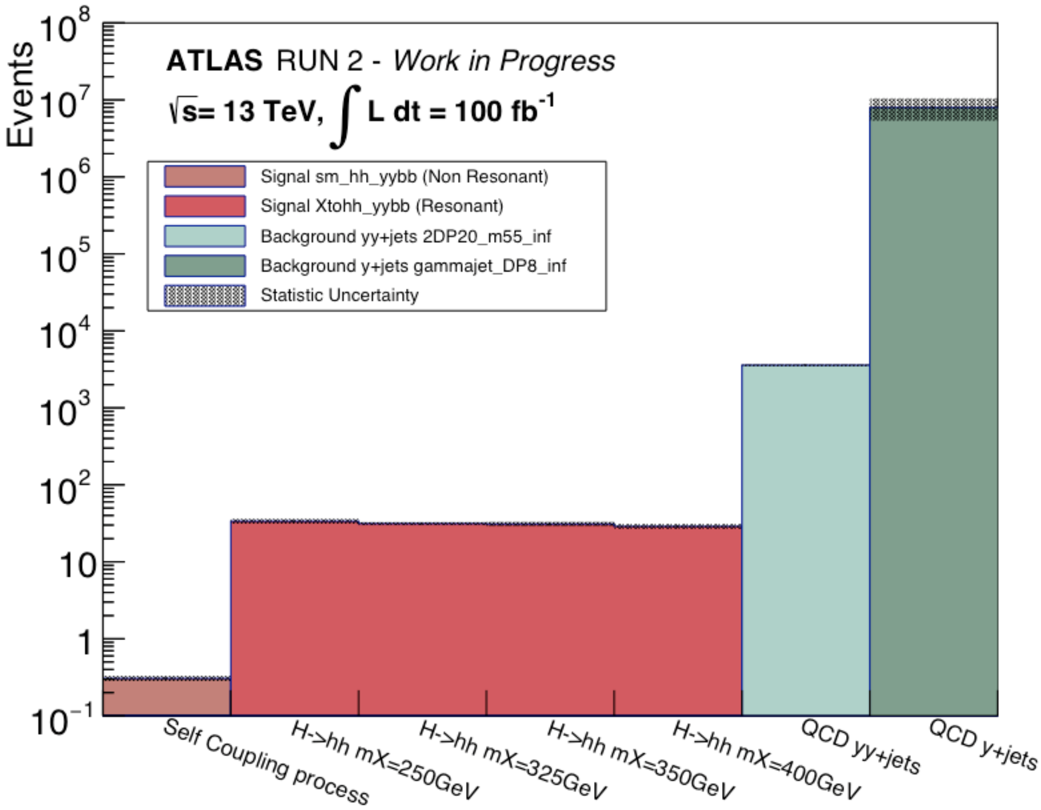

Figure 6.7: Results of expected number of events for signal and merged background in the **zero b-tagged category**

In this category, the γ+jets background is by far the dominant contribution with $(7.94 \pm 2.56) \times 10^6$ events expected at cutflow output. The $\gamma\gamma$+jets background also more than the signal with an expectation of 3588 ± 119 events. This background is completely hidden in the uncertainty of the main background. As discussed previously, it is due to the extremely low ratio between the number of events simulated and the number of events remaining after the event selection.

By comparison to the background, the signal number of expected events is very small. For the non-resonant Higgs self-coupling process, 0.31 ± 0.02 event are expected. The resonant heavy Higgs

[3] $N_w = 15$ for the $\gamma\gamma$+jets background and $N_w = 14$ for the γ+jets background

process predicts 33.7 ± 2.4 events for $m_X = 200$ GeV, 31.3 ± 1.5 for $m_X = 325$ GeV, 31.0 ± 2.2 for $m_X = 350$ GeV and 28.9 ± 2.2 for $m_X = 400$ GeV. The 0 b-tag category is used as a control region as the important difference between the signal and background expected number of events makes no observation possible of Higgs pair creation processes.

The two dominant backgrounds produce photons and jets, that are not necessary b-jets. The signal contains b-jets and the observation of signal events in the 0 b-tag category is coming from the misidentification of both b-jets. The efficiency for b-tagging is more than 70%, therefore, the misidentification of both b-jets concerns less than 9% of the events. This fact explains why there is around $O(100)$ times more events in the 2 b-tag category as in figure 6.9.

6.3.2 1 b-tag category

The results for the 1 b-tag category are presented in figure 6.8 for signal and merged background. This category, is also dominated by the γ+jets background with $(4.70 \pm 1.73) \times 10^5$ events expected. It is important to mention that due to b-tagging, this background decreases by $O(10)$ by comparison with the 0 b-tag category. The second domination is the $\gamma\gamma$+jets background with 476 ± 46 events expected.

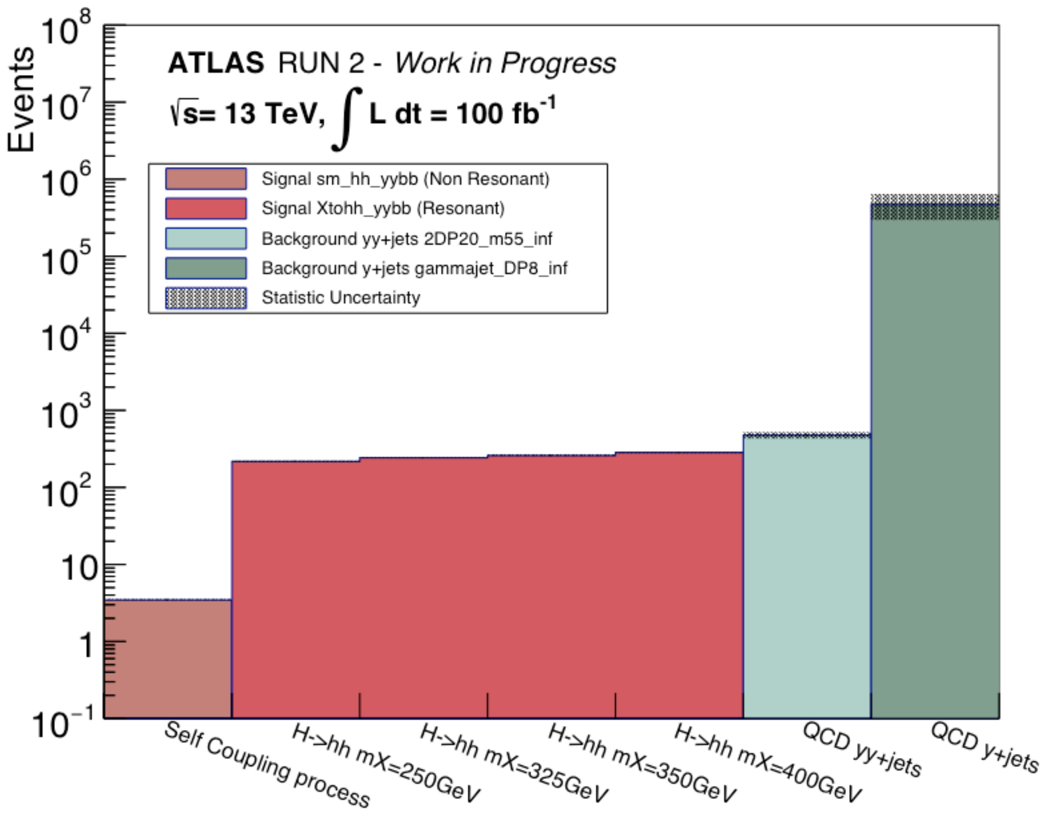

Figure 6.8: Results of expected number of events for signal and merged background in the **one b-tagged category**

For the reason discussed in the previous section 6.3.1, the number of expected signal events is increasing in the 1 b-tag category. The non-resonant Higgs self-coupling is expected to make a contribution of 3.47 ± 0.09 events. The resonant heavy Higgs channel predicts 217 ± 7 events for $m_X = 200$ GeV, 242 ± 5 for $m_X = 325$ GeV, 260 ± 7 for $m_X = 350$ GeV and 284 ± 7 for $m_X = 400$ GeV for the 1 b-tag category.

6.3.3 2 b-tag category

Finally, the signal region results are presented in the figure 6.9. The number of signal events is found to be greater than the expected background. This shows that b-tagging is a tool that gives a very good performance to suppress background. The non-resonant Higgs self-coupling is expected to make a contribution of 11.3 ± 0.1 events. The resonant heavy Higgs channel predicts 505 ± 10 events for $m_X = 200$ GeV, 651 ± 9 for $m_X = 325$ GeV, 495 ± 13 for $m_X = 350$ GeV and 881 ± 14 for $m_X = 400$ GeV for the 2 b-tag category. Concerning the background, the QCD $\gamma\gamma$+jets process is expected to produce 67.4 ± 23.6 events. The QCD γ+jets process to produce 69.3 ± 52.1 events.

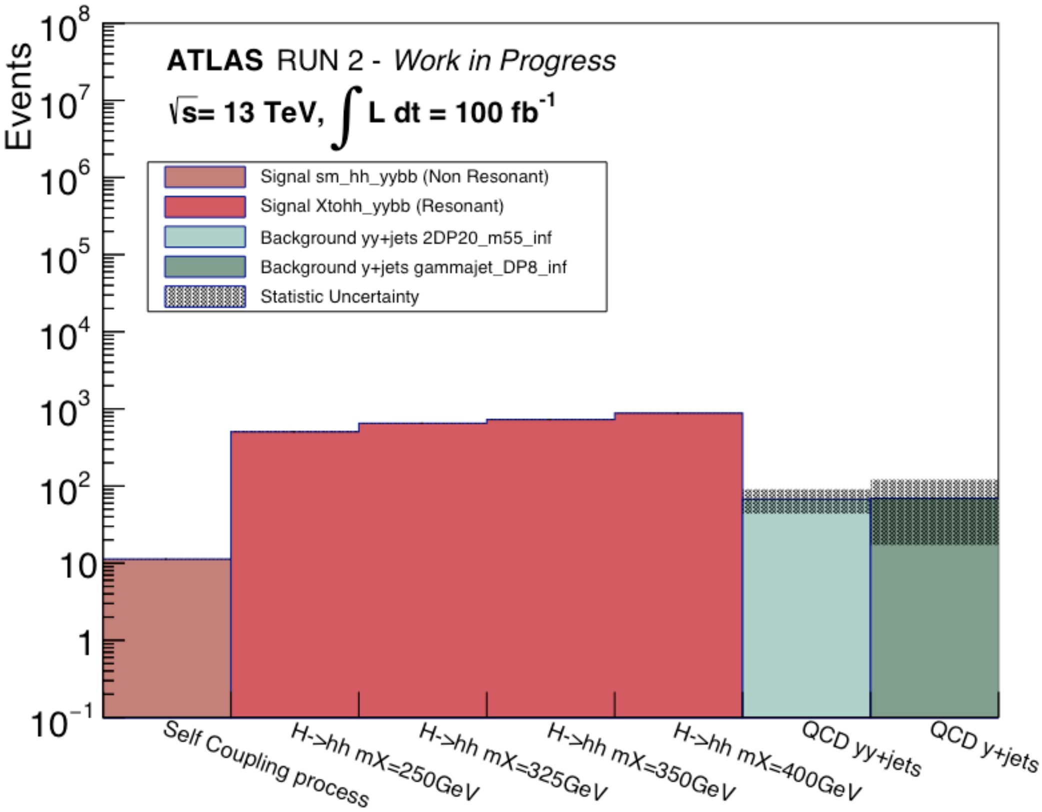

Figure 6.9: Results of expected number of events for signal and merged background in the **two b-tagged category**

The production cross-section for the four Heavy Higgs processes is assumed to be equal in this analysis, 0.01 pb However, the output number of expected events for the heavy Higgs with a mass of $m_X = 400$ GeV is slightly larger. This is mainly due to the increasing probability of producing two boosted SM Higgs bosons in the decay. The High Level Trigger involving high photon transverse momentum, gives best performance when the photons are coming from the decay of a boosted Higgs boson. As discussed in section 6.1.2, the High Level Trigger is the cut that reduces the most the number of events in the MxAOD production.

Concerning the Higgs self-coupling process, the expected number of events is hidden by the background uncertainty. A simulation of larger background samples is required as discussed.

	SAMPLE	$X_{sec} \times BR$ (pb)	n_{events} (MC xAOD)	n_{events} (Computed)
Signal	Self Coupling h->hh	9.89E-05	94312.3	98.943
	2HDM H->hh m_X=250 GeV	0.01	98986.4	10000
	2HDM H->hh m_X=325GeV	0.01	199731.4	10000
	2HDM H->hh m_X=350 GeV	0.01	99131.5.4	10000
	2HDM H->hh m_X=400 GeV	0.01	97237.1	10000
Background QCD $\gamma\gamma$+jets	2DP20_m55_100	36.0325	2.74E+06	36032540
	2DP20_m100_160	8.07501	3.19E+06	8075007.5
	2DP20_m160_250	2.14587	2.71E+06	2.15E+06
	2DP20_m250_400	0.5882	1.86E+06	588199.938
	2DP20_m400_650	0.13697	1.85E+06	136970.453
	2DP20_m650_1000	0.0255686	1.86E+06	2.56E+04
	2DP20_m1000_1500	0.00503021	973577	5030.212
	2DP20_m1500_2000	0.000782312	979847	782.312
	2DP20_m2000_2500	0.000173181	970236	173.181
	2DP20_m2500_3000	4.64E-05	992567	46.392
	2DP20_m3000_3500	1.39E-05	989252	13.911
	2DP20_m3500_4000	4.47E-06	986112	4.467
	2DP20_m4000_4500	1.49E-06	984170	1.486
	2DP20_m4500_5000	5.02E-07	986143	0.502
	2DP20_m5000_inf	2.57E-07	976589	0.257
Background QCD γ+jets	gammajet_DP8_17	-1	6.30614	n/a
	gammajet_DP17_35	477748	2594.55	4.77748E+11
	gammajet_DP35_50	34858	23460.9	3.485803E+10
	gammajet_DP50_70	10101.8	51915.8	1.010183E+10
	gammajet_DP70_140	4147.39	77611.3	4.14739E+9
	gammajet_DP140_280	328.036	43006.8	3.2803E+8
	gammajet_DP280_500	19.3309	57522.9	1.9330E+7
	gammajet_DP500_800	1.24451	68097.8	1.244514E+6
	gammajet_DP800_1000	0.0800278	7030.32	80027.781
	gammajet_DP1000_1500	0.0259049	7756.69	25904.906
	gammajet_DP1500_2000	0.00144349	8052.09	1443.489
	gammajet_DP2000_2500	0.000112796	8302.42	112.796
	gammajet_DP2500_3000	9.72E-06	8276.92	9.723
	gammajet_DP3000_inf	8.93E-07	7842.13	0.893

Table 6.1: The number of simulated MC events and computed from the cross-section times the branching ratio of signal and background processes

Part IV

Summary

Summary

The research presented in this thesis concerns the beginning of a project to develop the next generation pixel detector chips. It was written in the context of the LHC Run 2, while the first prototype for the next generation front end chips are under development. The discussion to share the production work are ongoing.

The motivations for this work were presented in Chapter 1 with an overview of the experimental context. The SM of particle physics was introduced in Chapter 2 with the introduction of two phenomena that contain Higgs pair production. In the Chapter 3, the FE-I4 front-end chip and its DAQ system were presented. The results on its first operation with the determination of threshold and ToT tuning parameters are presented in Chapter 4. The Chapter 5 contains an overview of the ATLAS software and a presentation of the event selection used in Higgs boson pair production analysis. Finally, the Chapter 6 presented the results on the MC simulation with an estimation of the number of events expected at the end of Run 2 for the Higgs self-coupling process and heavy Higgs boson production with the corresponding backgrounds.

The DAQ system was built to operate the FE-I4 chip. The results, presented in Chapter 4, concerns the first operation of the FE-I4 chip at Kyushu University and its *threshold* and *ToT* tuning. The corresponding parameters were carefully chosen so the signal amplification and discrimination within every pixel results in the same response, while reducing the noise and hence, optimize the data quality. The typical signal coming from a *MIP* that passes through the sensor was computed from the Bethe-Bloch formula. It is determined to be 15,000 electrons. The *threshold* target that optimizes threshold tuning was determined from the analog injection of the previous signal and was fixed to 3,000 electrons. The *ToT* was fixed to 5 $\times$25 ns after the verification of the threshold tuning performance for different ToT values.

The tuning parameter determination method described in this thesis can be used as a general way to optimize data taking quality for front-end electronics. By applying this method to the RD53 chip, it will be possible to quickly operate it.

The analysis of the prospects of Higgs pair production measurements was based on event selection criteria explained in Chapter 5. The simulation of *Higgs pair production* was privately made in comparison with official datasets as a way to understand the process and to produce new datasets corresponding to the new *collision energies*, *luminosities* or *detector geometry* as expected for the future ATLAS upgrades. The results gave a good accordance between the private and official samples, however, the production of a larger number of events for a more accurate comparison is needed.

The Chapter 6 presented the estimations of background and signal simulation as expected at the end of Run 2 with an integrated luminosity of $\mathscr{L}_{int} = 100\ \mathrm{fb}^{-1}$. The results in the *two b-tag signal region* are 11.3 ± 0.1 events expected for the *non-resonant Higgs self-coupling* process. The *resonant heavy Higgs* channel predictions depends on the hypothesis on the Heavy Higgs boson mass. The production cross section is assumed to be 0.01 pb. The prediction is 505 ± 10 events for $m_X = 200$ GeV, 651 ± 9 for $m_X = 325$ GeV, 495 ± 13 for $m_X = 350$ GeV and 881 ± 14 for $m_X = 400$ GeV.

Concerning the background, the $QCD\ \gamma\gamma + jets$ process is expected to produce 67.4 ± 23.6 events and the $QCD\ \gamma + jets$ process to produce 69.3 ± 52.1 events. The main observation is that the number of resonant signal events is found to be greater than the expected background. However, the measurement of $O(10)$ events for the Higgs self-coupling and $O(100)$ events for the heavy Higgs production is not high enough to predict an observation of the phenomena but only upper limits on the production cross-sections times branching ratio. Those limits are expected to be $O(1)$ pb while the SM predicts 9.89×10^{-5} pb for the Higgs self-coupling and the MSSM predicts $O(0.01)$ pb for the Heavy Higgs process. Moreover, a large statistical uncertainty was found for the QCD γ + jets background. A simulation containing more restrictions at the generation level is needed in order to reduce the very large number of simulated events cut during the derivation.

The recommendation for further work is to set a trigger on the FE-I4 system to tune the data taking proper time. The trigger signal is transmitted using the NIM standard and can be produced by a pulse function generator. To verify the acceptance of the signal as a NIM Standard, the OUT signal from the generator can be connected to a NIM counter. The firmware provides a latency register to delay the data output.

Concerning the analysis, a MC simulation involving NLO signal will necessitate the introduction of single Higgs production. Those samples can be produced using the method described in the Chapter 5. Another recommendation is to use the smearing functions to simulate Higgs pair production process under HL-LHC conditions. This method is accessible as HL-LHC samples were already produced using those smearing functions for the other processes. Furthermore, the analysis that will contain the full derivation for HL-LHC samples using the method of Chapter 5 will constitute an important step to understand accurately the prospects of Higgs boson pair measurements at the ATLAS experiment during HL-LHC.

Acknowledgment

This project was financed by the Mombu Kagaku Sho scholarship and the Rotary Yoneyama Memorial Fundation. I would like to thank all members of the Fukuoka Higashi Rotary Club for providing me support in many ways.

I would like to express my sincere gratitude to Professor Kiyotomo Kawagoe and my supervisor Professor Junji Tojo for giving me the chance to study in Japan. You considered me inside your institute as a Japanese student, as I wished by coming at Kyushu University. I would like to thank you very much for your support and understanding over these past three years.

I am also grateful to the staff members and students of the group of experimental particle physics as well as Kyushu University administration members for their patience and their help in overcoming numerous obstacles I have been facing through those three years in Japan. I would like to thanks particularly Susumu Oda for his support and advises in my research and also for reviewing this thesis. I also thank Driss Harrass, Ziane Izri, Masanori Hashimoto and Homare Kawasaki for their inspiration and friendship.

I would like to thank my professors of Japanese language, Teruyo Noguchi and Chitaru Sato for their precious help in learning Kanji. Thank you for your philanthropy and for the precious knowledge you share.

Last but not the least, I must express my very profound gratitude to my family, my friends and to my Ipopolis for providing me with unfailing support and continuous encouragement throughout my years of study and through the process of researching and writing this thesis. This accomplishment would not have been possible without them. Thank you.

Fukuoka
February 6th, 2017

M. Darnajou

Mathieu Darnajou

Appendix A

$\gamma\gamma b\bar{b}$ MC dataset production commands

Reproduction of the following sample :

- `mc15_13TeV.341559.MadGraphPythia8EvtGen_A14NNPDF23LO_sm_hh_yybb.merge.DAOD_HIGG1D1.e4038_s2608_s2183_r7772_r7676_p2669`

The AMI tags e4038, s2608, s2183, r7772, r7676 and p2669 contains the information for production commands[1]. The number of events that were produced in this study is small enough to make only one file and hence, the merging tags (s2183 and r7676) were not used here.

A.1 Generate e4038

Athena software version :

- `lsetup AtlasProduction,19.2.4.2`

Command used to run the generation :

```
Generate_tf.py \
--firstEvent 0 \
--randomSeed 0 \
--jobConfig MC15.341559.MadGraphPythia8EvtGen_A14NNPDF23LO_sm_hh_yybb.py \
--outputEVNTFile MC15.341559.MadGraphPythia8EvtGen_A14NNPDF23LO_sm_hh_yybb.py.EVNT
.pool.root
--runNumber 341559 \
--maxEvents 100 \
--evgenJobOpts MC15JobOpts -00-00-75_v1.tar.gz \
--ecmEnergy ´13000´
```

A.2 Simulation s2608

Local

Athena software version :

[1] more information on `https://ami.in2p3.fr/`

- `asetup AtlasProduction 19.2.3.7`

Command used to run the simulation :

- ```
  Sim_tf.py \
  --inputEVNTFile MC15.341559.MadGraphPythia8EvtGen_A14NNPDF23LO_sm_hh_yybb.py.EVNT.
  pool.root \
  --outputHITSFile MC15.341559.MadGraphPythia8EvtGen_A14NNPDF23LO_sm_hh_yybb.py.HITS
  .pool.root \
  --maxEvents 100 \
  --physicsList 'FTFP_BERT' \
  --truthStrategy 'MC12' \
  --simulator 'MC12G4' \
  --DBRelease 'default:current' \
  --conditionsTag 'default:OFLCOND-RUN12-SDR-19' \
  --DataRunNumber '222525' \
  --preInclude 'EVNTtoHITS:SimulationJobOptions/preInclude.BeamPipeKill.py,Simulatio
  nJobOptions/preInclude.FrozenShowersFCalOnly.py' \
  --geometryVersion 'default:ATLAS-R2-2015-03-01-00_VALIDATION' \
  --postInclude 'default:PyJobTransforms/UseFrontier.py'
  ```

On the grid

While the previous job were done locally, the simulation uses a lot of CPU time (about 3 minutes per events). It is requires, even for a small number of simulated events, to use the grid[2]. The command used is as following :

Pathena software version :

- `lsetup rucio 'asetup AtlasDerivation,20.1.6.3,gcc48,here' panda`

Command used to run the simulation on the grid :

- ```
  pathena \
  --useNewTRF \
  --trf "Sim_tf.py \
  --inputEVNTFile=%IN \
  --outputHITSFile=%OUT.HITS.pool.root \
  --maxEvents 100 \
  --physicsList 'FTFP_BERT' \
  --truthStrategy 'MC12' \
  --simulator 'MC12G4' \
  --DBRelease 'default:current' \
  --conditionsTag 'default:OFLCOND-RUN12-SDR-19' --DataRunNumber '222525' \
  ```

[2]The Worldwide LHC Computing Grid is a global computing infrastructure whose mission is to provide computing resources to store, distribute and analyze the data generated by the LHC. it is composed of four levels, or "Tiers", called 0, 1, 2 and 3. Each Tier is made up of several computer centers and provides a specific set of services.

```
--preInclude 'EVNTtoHITS:SimulationJobOptions/preInclude.BeamPipeKill.py,Simulatio
nJobOptions/preInclude.FrozenShowersFCalOnly.py' \
--geometryVersion 'default:ATLAS-R2-2015-03-01-00_VALIDATION' \
--postInclude 'default:PyJobTransforms/UseFrontier.py'" \
--inDS user.mdarnajo:MC15.341559.MadGraphPythia8EvtGen_A14NNPDF23LO_sm_hh_yybb.py.
EVNT.pool.root2 \
--outDS user.mdarnajo.1610281713officialyybbrepro.MadGraphPythia8EvtGen_A14NNPDF23
LO_sm_hh_yybb.py \
--nFilesPerJob=1 \
--nFiles=100 \
--nEventsPerJob=100
```

A.3 Digitization and Reconstruction r7772

This step contains both Digitization and Reconstruction. Athena software version :

- `asetup AtlasProd1,20.7.5.1.1`

Command used to run the reconstruction :

- ```
  Reco_tf.py \
  --inputHITSFile MC15.341559.MadGraphPythia8EvtGen_A14NNPDF23LO_sm_hh_yybb.py.HITS.
  pool.root \
  --outputAODFile MC15.341559.MadGraphPythia8EvtGen_A14NNPDF23LO_sm_hh_yybb.py.AOD.p
  ool.root \
  --inputLowPtMinbiasHitsFile mc15_13TeV.361034.Pythia8EvtGen_A2MSTW2008LO_minbias_i
  nelastic_low.merge.HITS.e3581_s2578_s2195/HITS.05608147._000001.pool.root.1 \
  --inputHighPtMinbiasHitsFile mc15_13TeV.361035.Pythia8EvtGen_A2MSTW2008LO_minbias_
  inelastic_high.merge.HITS.e3581_s2578_s2195/HITS.05608152._000001.pool.root.1
  \
  --digiSteeringConf 'StandardSignalOnlyTruth' \
  --conditionsTag 'default:OFLCOND-MC15c-SDR-09' \
  --ignorePatterns 'Py:TrigConf2COOLLib.py.+ERROR.==================================
  =+' \
  --pileupFinalBunch '6' \
  --numberOfHighPtMinBias '0.12268057' \
  --autoConfiguration 'everything' \
  --postInclude 'default:RecJobTransforms/UseFrontier.py' \
  --numberOfLowPtMinBias '39.8773194' \
  --steering 'doRDO_TRIG' \
  --preInclude 'HITtoRDO:Digitization/ForceUseOfPileUpTools.py,SimulationJobOptions/
  preInclude.PileUpBunchTrainsMC15_2015_25ns_Config1.py,RunDependentSimData/configLu
  mi_run284500_v2.py' 'RDOtoRDOTrigger:RecExPers/RecoOutputMetadataList_jobOptions.p
  y' \
  ```
  ```

```
--postExec 'all:CfgMgr.MessageSvc().setError+=["HepMcParticleLink"]' "ESDtoAOD:fix
edAttrib=[s if "CONTAINER_SPLITLEVEL = '99'" not in s else "" for s in svcMgr.Athe
naPoolCnvSvc.PoolAttributes];svcMgr.AthenaPoolCnvSvc.PoolAttributes=fixedAttrib"
\
--preExec 'all:rec.Commissioning.set_Value_and_Lock(True);from AthenaCommon.BeamFl
ags import jobproperties;jobproperties.Beam.numberOfCollisions.set_Value_and_Lock(
20.0);from LArROD.LArRODFlags import larRODFlags;larRODFlags.NumberOfCollisions.se
t_Value_and_Lock(20);larRODFlags.nSamples.set_Value_and_Lock(4);larRODFlags.doOFCP
ileupOptimization.set_Value_and_Lock(True);larRODFlags.firstSample.set_Value_and_
Lock(0);larRODFlags.useHighestGainAutoCorr.set_Value_and_Lock(True)' 'RAWtoESD:fro
m CaloRec.CaloCellFlags import jobproperties;jobproperties.CaloCellFlags.doLArCell
EmMisCalib=False' 'ESDtoAOD:TriggerFlags.AODEDMSet="AODSLIM"' \
--triggerConfig 'RDOtoRDOTrigger=MCRECO:DBF:TRIGGERDBMC:2046,20,56' \
--geometryVersion 'default:ATLAS-R2-2015-03-01-00' \
--numberOfCavernBkg '0' \
--jobNumber 1 \
--maxEvents -1
```

The pileup minimum bias files is set from the following :

Minbias HIGH

- `mc15_13TeV.361035.Pythia8EvtGen_A2MSTW2008LO_minbias_inelastic_high.merge.HITS.e3581_s2578_s2195/HITS.05608152._000001.pool.root.1`

Minbias LOW

- `mc15_13TeV.361034.Pythia8EvtGen_A2MSTW2008LO_minbias_inelastic_low.merge.HITS.e3581_s2578_s2195/HITS.05608147._000001.pool.root.1`

A.4 Reconstruction p2669

Athena software version :

- `asetup AtlasDerivation,20.7.6.4`

Command used to run the reconstruction :

```
Reco_tf.py \
--maxEvents -1 \
--inputAODFile ../Reco_r7772/MC15.341559.MadGraphPythia8EvtGen_A14NNPDF23LO_sm_hh_
yybb.py.AOD.pool.root \
--outputDAODFile MC15.341559.MadGraphPythia8EvtGen_A14NNPDF23LO_sm_hh_yybb.py.DAOD
.pool.root \
--reductionConf HIGG1D1 \
--passThrough 'True' \
```

```
--preExec 'default:from BTagging.BTaggingFlags import BTaggingFlags;BTaggingFlags.
CalibrationTag = "BTagCalibRUN12-08-18"' \
--jobNumber 1
```

Appendix B

MC Signal and Background Samples

The MC samples used in this analysis were produced using a method similar as explained in Appendix A. Every simulated phenomena are forced to produce $hh \to \gamma\gamma b\bar{b}$ for the signal or qq, qg or $gg \to \gamma\gamma b\bar{b}$ for the backgrounds from quark q or gluon g interactions. The production tags that contain information for simulation and derivation are also the same.

The samples listed here are DxAOD datasets, using the `HIGG1D1` derivation framework. The parton distribution function `A14NNPDF23LO` is used to simulate proton collisions. It was developed by the Neural Network Parton Distribution Functions Group at leading order. The center of mass energy of proton collision for the simulation is $\sqrt{s} = 13$ TeV. All samples (signal and backgrounds) are simulated at Leading Order (LO) under the MC15c campaign which is the current software version for MC dataset production.

B.1 Higgs pair production signal samples

Higgs self-coupling

The sample used to simulate Higgs self coupling is listed in Table B.1.

Sample Name	*Run*	*Generators*	*Order*	*Campaign*	*nEvents*
`sm_hh_yybb`	341559	MadGraph+Pythia8+EvtGen	LO	MC15c	100000

Table B.1: Sample used to simulate Higgs self-coupling

Heavy Higgs production

The mass of the heavy Higgs boson being a free parameter in the MSSM, four samples involving four different masses (275, 325, 350 and 400 GeV) were produced, listed in Table B.2.

Sample Name	*Run*	*Generators*	*Order*	*Campaign*	*nEvents*
`X275tohh_yybb`	341173	MadGraph+Pythia8+EvtGen	LO	MC15c	99000
`X325tohh_yybb`	341174	MadGraph+Pythia8+EvtGen	LO	MC15c	200000
`X350tohh_yybb`	341175	MadGraph+Pythia8+EvtGen	LO	MC15c	99000
`X400tohh_yybb`	341176	MadGraph+Pythia8+EvtGen	LO	MC15c	98000

Table B.2: List of samples for the simulation of Heavy Higgs production under four mass hypothesis

B.2 Backgrounds

QCD $\gamma\gamma$ + jets

As in Table B.3, the QCD $\gamma\gamma$ + jets background were produced in 15 samples corresponding to windows over the reconstructed mass of the di-photon system. The name "Mass_X_Y" means that the window is between the X and Y boundaries in GeV. "inf" means that no upper boundary were put on the di-photon system mass for the corresponding sample.

Sample Name	*Run*	*Generators*	*Order*	*Campaign*	*nEvents*
Mass_55_100	302520	Pythia8+EvtGen	LO	MC15c	2698325
Mass_100_160	302521	Pythia8+EvtGen	LO	MC15c	3178112
Mass_160_250	302522	Pythia8+EvtGen	LO	MC15c	2710734
Mass_250_400	302523	Pythia8+EvtGen	LO	MC15c	1858485
Mass_400_650	302524	Pythia8+EvtGen	LO	MC15c	1856871
Mass_650_1000	302525	Pythia8+EvtGen	LO	MC15c	1862854
Mass_1000_1500	302526	Pythia8+EvtGen	LO	MC15c	974995
Mass_1500_2000	302527	Pythia8+EvtGen	LO	MC15c	980494
Mass_2000_2500	302528	Pythia8+EvtGen	LO	MC15c	970569
Mass_2500_3000	302529	Pythia8+EvtGen	LO	MC15c	993867
Mass_3000_3500	302530	Pythia8+EvtGen	LO	MC15c	989482
Mass_3500_4000	302531	Pythia8+EvtGen	LO	MC15c	986790
Mass_4000_4500	302532	Pythia8+EvtGen	LO	MC15c	985493
Mass_4500_5000	302533	Pythia8+EvtGen	LO	MC15c	986642
Mass_5000_inf	302534	Pythia8+EvtGen	LO	MC15c	978766

Table B.3: List of QCD $\gamma\gamma$ + jets background samples

QCD γ + jets

The QCD γ + jets background were produced in 14 samples listed in Table B.4. This background containing only one photon, the windows correspond to its transverse momentum. In the sample name "gammajet_X_Y", the windows contains a photon with a transverse momentum between X and Y in GeV. As for the QCD $\gamma\gamma$ + jets background samples, "inf" means that no upper boundary were put on the photon transverse momentum for the corresponding sample.

The number of events is very small due to the HIGG1D1 derivation that cuts most of the events. As detailed in the results (Sec. 6.2), this fact increases the statistical uncertainty in the background estimations.

Sample Name	*Run*	*Generators*	*Order*	*Campaign*	*nEvents*
`gammajet_DP8_17`	423099	Pythia8+EvtGen	LO	MC15c	10
`gammajet_DP17_35`	423100	Pythia8+EvtGen	LO	MC15c	2620
`gammajet_DP35_50`	423101	Pythia8+EvtGen	LO	MC15c	23609
`gammajet_DP50_70`	423102	Pythia8+EvtGen	LO	MC15c	52299
`gammajet_DP70_140`	423103	Pythia8+EvtGen	LO	MC15c	71928
`gammajet_DP140_280`	423104	Pythia8+EvtGen	LO	MC15c	43308
`gammajet_DP280_500`	423105	Pythia8+EvtGen	LO	MC15c	56027
`gammajet_DP500_800`	423106	Pythia8+EvtGen	LO	MC15c	68503
`gammajet_DP800_1000`	423107	Pythia8+EvtGen	LO	MC15c	7046
`gammajet_DP1000_1500`	423108	Pythia8+EvtGen	LO	MC15c	7821
`gammajet_DP1500_2000`	423109	Pythia8+EvtGen	LO	MC15c	8039
`gammajet_DP2000_2500`	423110	Pythia8+EvtGen	LO	MC15c	8515
`gammajet_DP2500_3000`	423111	Pythia8+EvtGen	LO	MC15c	8499
`gammajet_DP3000_inf`	423112	Pythia8+EvtGen	LO	MC15c	8197

Table B.4: List of QCD γ + jets background samples

List of Acronyms

- **2HDM** Two Higgs Doublet Model
- **BEH** Brout-Englert-Higgs
- **CERN** Centre Européen de Recherche Nucléaire
- **DAQ** Data Acquisition
- **EM** Electromagnetic
- **ENC** Equivalent Noise Charge
- **EWSB** ElectroWeak Symmetry Breaking
- **FE** Front End
- **ggF** gluon-gluon fusion
- **GRL** Good Run List
- **ITk** Inner Tracker
- **JVT** Jet Vertex Tagger
- **LAr** Liquid Argon
- **LHC** Large Hadron Collider
- **LO** Leading Order
- **MIP** Minimum Ionizing Particles
- **MSSM** Minimal Supersymmetric Standard Model
- **NLO** Next to Leading Order
- **PV** primary vertex
- **QCD** Quantum ChromoDynamics
- **QED** Quantum ElectroDynamics
- **RDO** Raw Data Object
- **SCT** Semiconductor Tracker
- **SEABAS** Soi EvAluation BoArd with Sitcp
- **SM** Standard Model
- **ToT** Time over Threshold
- **TRT** Transition Radiation Tracker

- **ttH** $t\bar{t}$ associated Higgs
- **VBF** vector boson fusion
- **VH** associated Higgs
- **xAOD** Analysis Object Data

Bibliography

[1] J. Baglio, A. Djouadi, R. Grober, M. M. Muhlleitner, J. Quevillon, M. Spira *JHEP **1304**, 151 (2013).*

[2] ATLAS Collaboration, "Search for Higgs boson pair production in the $hh \to bb\tau\tau$, $\gamma\gamma WW^*$, $\gamma\gamma bb$, $bbbb$ channels with the ATLAS detector," *Phys. Rev. D **92**, 092004(2015).*

[3] O. B. L. Rossi, "High Luminosity Large Hadron Collider : A description for the European Strategy Preparatory Group," *CERN-ATS **236** (2012).*

[4] ATLAS Collaboration, "The ATLAS Experiment at the CERN Large Hadron Collider," *JINST **3**, S08003(2015).*

[5] R.L. Bates, "ATLAS pixel upgrade for the HL-LHC," *24th International Workshop on Vertex Detector*, vol. 006, 2015.

[6] RD53 Collaboration, "RD Collaboration Proposal: Development of pixel readout integrated circuits for extreme rate and radiation," *CERN-LHCC **008** (2013).*

[7] RD53 Collaboration, M. Deveria et al., "RD-53 collaboration and CHIPIX65 project for the development of an innovative Pixel Front End Chip for HL-LHC," *JINST **010** (2015).*

[8] B. R. Martin, G. Shaw, *Particle Physics.* Manchester, UK: Wiley, 2008.

[9] C.S. Wu, E. Ambler, R.W. Hayward, D.D. Hoppes, R.P. Hudson *Phys. Rev. Lett. **105**, 1413–1414 (1957).*

[10] R. P. Feynman, M. Gell-Mann *Phys. Rev. **105**, 193-198 (1958).*

[11] S.M. Bilenky, J. Hosek *Phys.Rept. **90**, 73-157 (1982).*

[12] Gargamelle Neutrino Collaboration *Nucl. Phys. B **18**, 218-236 (1977).*

[13] P. Higgs *Phys. Lett. **12**, 132-133 (1964).*

[14] F. Englert, R. Brout *Phys. Rev. Lett. **13**, 321 (1964).*

[15] ATLAS Collaboration *Phys. Lett. B **716**, 1-29 (2012).*

[16] CMS Collaboration *Phys. Lett. B **716, 30-61 (2012)**.*

[17] ATLAS Collaboration *Phys. Lett. B **726**, 88-119 (2013).*

[18] ATLAS Collaboration *Phys. Lett. B **726**, 120-144 (2013).*

[19] M. Spira, “Higgs Boson Production and Decay at Hadron Colliders,” *arXiv:1612.07651v1 (2016).*

[20] M. Slawinska, W. Wollenberg, B. Eijk, S. Bentvelsen, “Phenomenology of the trilinear Higgs coupling at proton-proton colliders,” *arXiv:1408.5010v2 (2014).*

[21] R. Grober, M. M. Muhlleitner *JHEP* ***1106****, 20 (2011).*

[22] G.C. Brancoa, P.M. Ferreirab, L. Lavouraa, M.N. Rebeloa, M. Sherd, J.P. Silvab *Phys. Rep.* ***516****, 1-102 (2012).*

[23] P. Fayet *Phys. Lett. B* ***69****, 489-494 (1977).*

[24] K. Inoue, A. Kakuto, H. Komatsu, S. Takeshita *Prog. Theor. Phys.* ***67****, 1889-1898 (1982).*

[25] K. Inoue, A. Kakuto, H. Komatsu, S. Takeshita *Prog. Theor. Phys.* ***68****, 927-946 (1982).*

[26] P. Fayet *Nucl. Phys. B* ***90****, 104-124 (1975).*

[27] A. Djouadi *Phys. Rep.* ***459****, 1-241 (2008).*

[28] ATLAS collaboration *JHEP* ***56****, 1-241 (2014).*

[29] CMS Collaboration, “Searches for a heavy scalar boson h decaying to a pair of 125 GeV Higgs bosons hh or for a heavy pseudoscalar boson A decaying to Zh, in the final states with $h \to \tau\tau$,” *Phys. Lett. B* ***755****, (2015).*

[30] M. Carena, J.R. Espinosa, M. Quiros, C.E.M. Wagner *Phys. Lett. B* ***755****, 209-221 (1995).*

[31] J. Ellis, G. Ridolfi, F. Zwirner *Phys. Lett. B* ***257****, 83-91 (1991).*

[32] H.E. Haber, R. Hempfling, “Can the mass of the lightest Higgs boson of the minimal supersymmetric model be larger than m_z?,” *Phys. Rev. Lett.* ***66****, (1991).*

[33] A. Djouadi, J. Quevillon, “The MSSM Higgs sector at a high m_{SUSY}: reopening the low $\tan\beta$ regime and heavy Higgs searches,” *JHEP* ***28*** *(2013).*

[34] M. Carena, H.E. Haber, I. Low, N.R. Shah, C.E.M. Wagner, “Complementarity between nonstandard Higgs boson searches and precision Higgs boson measurements in the MSSM,” *Phys. Rev. D* ***91*** *(2015).*

[35] ATLAS Collaboration, “Search for Higgs Boson Pair Production in the $\gamma\gamma b\bar{b}$ Final State using pp Collision Data at $\sqrt{s} = 8$ TeV from the ATLAS Detector,” *Phys. Rev. Lett.* ***113*** *(2014).*

[36] F. Hartmann, *Evolution of Silicon Sensor Technology in Particle Physics.* Springer Science, 2008.

[37] Xilinx, “Virtex-5 Family Overview,” *Product Specification* ***DS100****, v5.1 (2015).*

[38] Xilinx, “Virtex-4 Family Overview,” *Product Specification* ***DS112****, v3.1 (2010).*

[39] T. Uchida, “SiTCP Manual,” *Electronics system group, IPNS, KEK* ***DS100****, v1.4 (2012).*

[40] FE-I4 Collaboration, “The FE-I4A integrated circuit guide,” *Version 11.3*, 2011.

[41] FE-I4 Collaboration, “The FE-I4B integrated circuit guide,” *Version 2.0*, 2012.

[42] ATLAS Collaboration, “The ATLAS simulation infrastructure,” *Eur. Phys.* ***70**, 823-874 (2010)*.

[43] A. Rimoldi, “The full detector simulation for the ATLAS experiment : status and outlook,” *Computing in High Energy and Nuclear Physics* ***TUMT001*** *(2003)*.

[44] U. Baur, T. Plehn, D. Rainwater, “Probing the Higgs self-coupling at hadron colliders using rare decays,” *Phys. Rev. D* ***69**, 053004 (2003)*.

[45] ATLAS Collaboration, “Measurements of Higgs boson production and couplings in diboson final states with the ATLAS detector at the LHC,” *Phys. Lett. B* ***726**, 88-119 (2013)*.

[46] M. Cacciari, G.P. Salam, G. Soyez, “The anti-k_t jet clustering algorithm,” *JHEP* ***804*** *(2008)*.

[47] J. Alwall, M. Herquet, F. Maltoni, O. Mattelaer, T. Stelzer, “MadGraph 5 : Going Beyond,” *JHEP* ***128*** *(2011)*.

[48] T. Sjöstrand, S. Mrenna, P. Skands, “A Brief Introduction to PYTHIA 8.1,” *Comput. Phys. Commun* ***013**, 01 (2008)*.